

# PHASE-LOCKED FOURIER DOMAIN OPTICAL COHERENCE TOMOGRAPHY

THÈSE N° 3847 (2007)

PRÉSENTÉE LE 6 JUILLET 2007

À LA FACULTÉ DES SCIENCES ET TECHNIQUES DE L'INGÉNIEUR

Laboratoire d'optique biomédicale

PROGRAMME DOCTORAL EN PHOTONIQUE

ÉCOLE POLYTECHNIQUE FÉDÉRALE DE LAUSANNE

POUR L'OBTENTION DU GRADE DE DOCTEUR ÈS SCIENCES

PAR

**Adrian H. BACHMANN**

ingénieur en microtechnique diplômé EPF  
de nationalité suisse et originaire de Bäretswil (ZH)

acceptée sur proposition du jury:

Prof. J.-E. Moser, président du jury  
Prof. T. Lasser, Prof. R. Leitgeb, directeurs de thèse  
Prof. H. P. Herzig, rapporteur  
Prof. J. Izatt, rapporteur  
Prof. R. Salathé, rapporteur



ÉCOLE POLYTECHNIQUE  
FÉDÉRALE DE LAUSANNE

Suisse  
2007

The work presented in this thesis was performed at the Laboratoire d'Optique Biomédicale, École Polytechnique Fédérale de Lausanne, Lausanne, Switzerland.

The author gratefully acknowledges grants from the Swiss National Science Foundation (205321-109704/1 and 3200-062028.00/1) and Swiss Academy of Engineering Sciences (SATW project TK 01/06).

**To my family**





## Abstract

Fourier or spectral domain optical coherence tomography (FDOCT) is a multi-dimensional interferometric imaging modality that has attracted increasing interest during the last few years. The reason is its outstanding sensitivity allowing high speed 2D and 3D imaging of weakly backscattering biological tissues *iv vivo* and with high axial resolution. FDOCT has today largely replaced the preceding time domain OCT due to its marked advantage in sensitivity and acquisition speed. In particular, for fast *iv-vivo* retinal imaging with high resolution in 3D, FDOCT has become the method of choice. Recent developments enhance the clinical and biomedical potential of FDOCT by aiming from purely structural to functional tissue imaging, revealing tissue dynamics and physiology. The imaging parameter space is becoming highly multi-dimensional by including polarization, Doppler flow and spectroscopy.

Two operating modes of FDOCT exist: spectrometer-based and swept-source. The latter captivates with its unprecedented depth-scan speed of several 100kHz whereas the spectrometer-based FDOCT offers ultra-high axial resolution capabilities of 2 $\mu$ m or even better. However, there are drawbacks to both FDOCT modalities including the depth-dependent sensitivity decay as well as the complex ambiguity of the FDOCT signal which leads to disturbing mirror structures as well as a restricted maximum depth range. Phase shifting techniques allow reconstruction of the complex sample signal, resolving the complex ambiguities, therefore reducing these drawbacks considerably. In addition, in the spectrometer-based FDOCT, any sample movement during camera integration causes a blurring of the interference fringes and thus reduces the sensitivity for flow detection. However, information on flow is especially interesting in ophthalmology since several studies of retinal blood flow – using laser Doppler flowmetry – have already outlined that vessel flow properties are early indicators of retinal pathologies like glaucoma, diabetic retinopathy or age related macula degeneration.

*This thesis proposes two new spectrometer-based FDOCT modalities, both based on the phase-sensitive nature of OCT. Appropriate locking of acquisition speed, exposure time and triggering onto artificially provoked signal phase changes allows the technique to benefit from additional degrees of freedom in the signal detection. The various established models were experimentally verified on biological and technical samples.*

First, spectrometer-based heterodyne FDOCT, without chromatic phase-shifting errors, was presented and discussed. The achromatic phase-shifting is achieved by using acousto-optic frequency shifters (AOFS). *Iv-vivo* measurements showed experimentally the suppression of FDOCT-inherent artifacts like complex mirror terms due to the full complex signal reconstruction by quadrature detection of a stable beating frequency at 20'000 depth-scans per second using integrating buckets. In the search for ultra-high axial resolution, the currently available AOFS used were found to be a limiting factor and so further AOFS were developed to provide truly broadband devices. A dual beam extension allowed phase sensitive measurements even through long probing fibers. Phase stability issues with respect to the

complex signal reconstruction algorithms used were discussed and it was shown theoretically, and verified experimentally, that amplitude errors are equally disturbing as phase errors.

Second, a novel FDOCT modality called resonant Doppler FDOCT was introduced preventing interference fringe blurring caused by moving structures such as flow. The proposed method overcomes this problem by phase-matching the interferometer reference signal to the sample motion by means of an electro-optic phase modulator. Extraction of *in-vivo* blood flow in 3D on a purely intensity basis with an improved velocity range as compared to currently performed color Doppler FDOCT was shown. In addition, for this proposed method, the detectable velocity range is independent of the detector speed. Quantitative flow detection was demonstrated with the same method.

**Keywords:** Optical coherence tomography (OCT); Fourier or spectral domain OCT (FDOCT); complex, phase-sensitive, achromatic, heterodyne, full-range FDOCT; common path, dual beam FDOCT; acousto-optic frequency shifting; phase stability; phase errors; resonant Doppler FDOCT; functional OCT.

## Résumé

La tomographie par cohérence optique dans le domaine spectral ou de Fourier est une méthode d'imagerie multidimensionnelle interférométrique dont l'intérêt est en constante croissance depuis ces dernières années. Ceci résulte d'une extraordinaire sensibilité permettant une imagerie 2D et 3D à haute vitesse de tissus biologiques *iv vivo* à faible rétrodiffusion ainsi que d'une très haute résolution axiale. La FDOCT a aujourd'hui largement remplacé son prédécesseur dans le domaine temporel grâce à ses avantages marqués au niveau de la sensibilité et de la vitesse d'acquisition. En particulier, pour des acquisitions tridimensionnelles rapides et *iv vivo* de la rétine avec une haute résolution, la FDOCT s'avère être la méthode de prédilection. Les récents développements ont affirmé le potentiel clinique et biomédical de la FDOCT pour passer d'une information purement structurale à une véritable imagerie fonctionnelle du tissu révélant sa dynamique et sa physiologie. L'espace des paramètres d'imagerie est devenu hautement multidimensionnel en incluant la polarisation, l'effet Doppler et la spectroscopie.

Deux modes opératoires de la FDOCT existent: une approche basée sur un spectromètre et une seconde sur une source variable en longueur d'onde. Cette dernière se distingue par une vitesse d'acquisition de la structure en profondeur de quelques 100kHz jusqu'à aujourd'hui inégalée, alors que l'approche spectrométrique offre une résolution axiale extrêmement élevée de  $2\mu m$  ou mieux. Cependant, plusieurs inconvénients sont inhérents aux deux méthodes spectrales parmi lesquels une décroissance de la sensibilité en profondeur ainsi qu'une ambiguïté complexe sur le signal FDOCT résultant en la présence nuisible de structures miroirs et en une profondeur de mesure maximale réduite. Des techniques de décalage de phase permettent cependant la reconstruction du signal complexe de l'échantillon résolvant les ambiguïtés complexes et permettant ainsi une réduction considérable des désavantages. En sus, dans la méthode spectrométrique, un mouvement de l'échantillon durant la période d'intégration de la caméra induit une réduction du contraste des franges d'interférence provoquant ainsi une diminution de la sensibilité pour la détection de flux. Toutefois l'information du flux est d'un intérêt fondamental en ophtalmologie tel que cela a été démontré par plusieurs études sur le flux sanguin rétinien utilisant une mesure de flux par laser Doppler. Ces études soulignent la propriété du flux des vaisseaux à indiquer précocement les pathologies de la rétine tels que le glaucome, la rétinopathie diabétique ou la dégénérescence maculaire liée à l'âge.

*Cette thèse propose deux nouvelles approches spectrométriques de la FDOCT, les deux basées sur la nature de la dépendance en phase de l'OCT. Un contrôle particulier du temps d'exposition, du déclenchement et de la vitesse d'acquisition sur des changements intentionnellement provoqués du signal de phase alloue à la technique le bénéfice de degrés de libertés supplémentaires dans le signal de détection. Les différents modèles établis ont été expérimentalement vérifiés sur des échantillons biologiques et techniques.*

Tout d'abord, l'approche spectrométrique hétérodyne de la FDOCT, en l'absence d'erreur de déphasage chromatique, est présentée et discutée. Le déphasage achromatique est réalisé

grâce à l'utilisation de modules acousto-optiques pour le décalage en fréquence (*frequency shifters*, AOFS). Les mesures *iv vivo* ont montré expérimentalement la suppression des artefacts inhérents à la FDOCT, comme les termes miroirs complexes, due à la reconstruction complète du signal complexe par l'utilisation d'une détection en quadrature d'une fréquence de battements stable à 20'000 acquisitions en profondeur par seconde par l'intermédiaire de *integrating buckets*. Dans la recherche d'une résolution axiale extrêmement élevée, les AOFS actuellement disponibles se révèlent être un facteur limitant; aussi des AOFS améliorés ont été développés pour obtenir un élément effectivement large bande. Une extension à deux faisceaux (*dual beam*) permet une mesure sensible en phase même à travers de longues fibres de mesure. La stabilité de phase par rapport aux algorithmes de reconstruction du signal complexe utilisés a été discutée et il a été théoriquement et expérimentalement vérifié que les erreurs d'amplitude sont autant perturbatrices que les erreurs de phase.

Puis, une nouvelle méthode FDOCT appelée *resonant Doppler FDOCT* a été introduite pour prévenir le flou des franges d'interférence induit par des éléments mouvants tel que le flux. La méthode proposée surmonte ce problème grâce à un signal de référence en phase avec le mouvement de l'échantillon par l'intermédiaire d'un modulateur de phase électro-optique. L'extraction de flux sanguin tridimensionnel *iv vivo* par une pure mesure d'intensité avec un domaine de vitesse accru par rapport à la méthode *color Doppler FDOCT* est démontrée. De plus, pour cette méthode proposée, la plage de vitesse détectable est indépendante de la vitesse d'acquisition du détecteur. Une détection quantitative du flux a également été démontrée avec la même méthode.

**Mots-clés:** Tomographie par cohérence optique (OCT); Fourier ou spectral OCT (FDOCT); FDOCT complexe, sensibilité de phase, achromatique, hétérodyne, profondeur complète; FDOCT à parcours commun, faisceau double; décalage de fréquence par module acousto-optique; stabilité de phase; erreurs de phase; *resonant Doppler FDOCT*; OCT fonctionnelle.

## Kurzfassung

Optische Kohärenztomographie im Fourier- bzw. Spektralbereich (FDOCT) ist ein mehrdimensionales, interferometrisches Bildgebungsverfahren, welches in den letzten Jahren vermehrt Beachtung gefunden hat. Der Grund dafür ist die überragende Empfindlichkeit, welche es sowohl in 2D als auch in 3D erlauben, schwach zurückstreuendes biologisches Gewebe *iv-vivo* und mit hoher axialer Auflösung abzubilden. FDOCT hat heute das vorausgehende Time Domain OCT wegen der besseren Empfindlichkeit sowie des kürzeren Erfassungszeit weitgehend ersetzt. Im Speziellen im Bereich der schnellen *iv-vivo* Bildgebung der Retina mit hoher 3D-Auflösung hat sich FDOCT als bevorzugte Methode etabliert. Aktuelle Entwicklungen verbessern das klinische und das biomedizinische Potential von FDOCT, indem sie das Bildgebungsverfahren von rein strukturellen hin zu funktionellen Geweben führen und somit die Dynamik des Gewebes sowie die Physiologie offenlegen. Der Parameter-Raum wird durch die Einführung von Polarisierung, Doppler-Fluss und Spektroskopie in einem hohen Masse mehrdimensional.

Für FDOCT existieren zwei Betriebsmodi: Spektrometer-basiert sowie Wellenlängen-getunt. Letzteres besticht durch seine einzigartige Tiefenscan-Geschwindigkeit von mehreren 100kHz, wohingegen die Spektrometer-basierte FDOCT eine ultra-hohe axiale Auflösung von 2µm und besser ermöglicht. Dennoch weisen beide FDOCT-Betriebsmodi Nachteile auf. Dazu gehören der tiefenabhängige Sensibilitätsabfall sowie die komplexe Mehrdeutigkeit des FDOCT-Signals, welche störende, gespiegelte Strukturen hervorruft, sowie die maximale Messtiefe beschränkt. Da Phasenverschiebungstechniken die komplexen Ambiguitäten auflösen können, ermöglichen sie die Rekonstruktion vom komplexen Probensignal und reduzieren damit die Nachteile von FDOCT erheblich. Beim Spektrometer-basierten FDOCT kommt hinzu, dass jegliche Bewegung der Probe während der Bildaufnahme im interferometrischen Signal Kontrastverringerung verursacht und damit die Empfindlichkeit der Flussdetektion beeinträchtigt. Dennoch ist die Flussinformation speziell im Bereich der Ophthalmologie interessant, weil mehrere Studien über den retinalen Blutfluss – unter Verwendung von Doppler-Strömungsmessung – bereits zeigen konnten, dass die Eigenschaften der Gefäßdurchblutung Frühindikatoren von retinalen Pathologien wie das Glaukom, diabetische Retinopathie oder altersbedingte Makula-Degenration sind.

*Diese Doktorarbeit präsentiert zwei neue Spektrometer-basierte FDOCT-Modalitäten. Beiden liegt die Natur der Phasen-Sensibilität von OCT zugrunde. Geeignetes Koordinieren von Akquisitionsgeschwindigkeit, -auslösung und Belichtungszeit mit Hilfe von künstlich provozierten Signalphasenänderungen ermöglicht es, zusätzliche Freiheitsgrade bei der Signaldetektion zu nutzen. Die verschiedenen Modelle wurden experimentell auf biologischen und technischen Proben getestet.*

Im ersten Teil der Arbeit wurde das Spektrometer-basierte Heterodyn-FDOCT ohne chromatische Phasenverschiebungsfehler präsentiert und diskutiert. Die achromatische Phasenverschiebung wird durch die Verwendung von akusto-optischen Frequenzverschiebern (AOFS) erreicht. *Iv-vivo* Messungen zeigten experimentell die

Unterdrückung von FDOCT-inhärenten Artefakten wie z.B. der komplexen Spiegel-Terme (komplexe Mehrdeutigkeit). Dies wird durch die vollständige komplexe Signalrekonstruktion mit Quadratur-Erkennung von einer stabilen Schwebefrequenz bei 20'000 Tiefenscans pro Sekunde erreicht. Mit dem Ziel ultra-hoher axialer Auflösung wurden die AOFSSs als limitierende Faktoren identifiziert. Deshalb wurden neue AOFSSs entwickelt, um echte Breitband-Anwendungen zu ermöglichen. Eine Doppelstrahl-Erweiterung ermöglichte phasensensitive Messungen sogar unter Verwendung von langen Messfasern. Phasenstabilitäts-Sachverhalte im Bezug auf die verwendeten, komplexen Signalrekonstruktionsalgorithmen wurden diskutiert und es wurde theoretisch gezeigt und experimentell verifiziert, dass sich die Amplitudenfehler gleich stören wie die Phasenfehler auswirken.

Im zweiten Teil der Arbeit wurde eine neuartige FDOCT-Modalität, das sogenannte Resonante Doppler-FDOCT, eingeführt. Diese neue Methode verhindert die Verwischung des interferometrischen Signals, welche bei sich bewegenden Strukturen wie zum Beispiel Blutfluss entstehen. Die vorgeschlagene Methode überwindet dieses Problem, indem sie mit Hilfe eines elektro-optischen Phasenmodulators die Phase des Interferometer-Referenzsignals mit der Bewegung der Probe abstimmt. Ebenfalls gezeigt wurde die Extraktion von *iv-vivo* Durchblutung in 3D auf reiner Intensitätsbasis, mit einem im Vergleich zur aktuell verwendeten Phasen-Doppler-FDOCT verbesserten Geschwindigkeitsbereich. Für die vorgeschlagene Methode ist der detektierbare Geschwindigkeitsbereich zudem unabhängig von der Detektor-Geschwindigkeit. Quantitative Strömungs-Detektion konnte mit derselben Methode ebenfalls gezeigt werden.

**Stichwörter:** Optische Kohärenztomographie (OCT); spektrale optische Kohärenztomographie oder Optische Kohärenztomographie im Fourierbereich (FDOCT); komplexe, phasen-sensitive, achromatische, Heterodyn-FDOCT; Einzelstrahl, Doppelstrahl FDOCT; akkusto-optische Frequenzverschiebung; Phasenstabilität; Phasenfehler; resonantes Doppler FDOCT; funktionelles OCT.

# Table of Content

<b>Abstract</b>	<b>v</b>
<b>Résumé</b>	<b>vii</b>
<b>Kurzfassung</b>	<b>ix</b>
<b>Table of content</b>	
<b>Part I - General introduction</b>	
<b>1 Introduction</b>	<b>3</b>
<b>2 State of the art</b>	<b>5</b>
2.1 Short review – optical coherence tomography .....	5
2.2 Basic FDOCT theory .....	6
2.2.1 Fourier transform for accessing structural information.....	6
2.2.2 Depth range, lateral and axial resolution.....	7
2.2.3 Signal-to-noise ratio and sensitivity .....	8
2.3 Phase shifting in FDOCT .....	9
2.3.1 Introduction .....	9
2.3.2 Color Doppler FDOCT.....	9
<b>Part II - Heterodyne spectrometer-based FDOCT</b>	
<b>3 Heterodyne FDOCT</b>	<b>17</b>
3.1 Introduction .....	17
3.2 Theory .....	20
3.2.1 Complex FDOCT signal.....	21
3.2.2 Differential complex reconstruction.....	22
3.3 Experimental .....	23
3.3.1 Setup.....	23
3.3.2 Detailed synchronization scheme.....	25
3.4 Results and discussion.....	26
3.5 Conclusion.....	28

<b>4</b>	<b>Broadband fiberized acousto-optic frequency shifter</b>	<b>29</b>
4.1	Introduction .....	29
4.2	Theory .....	29
4.2.1	Principle of acousto-optics .....	29
4.2.2	Acousto-optical diffraction regimes .....	30
4.2.3	Diffraction efficiency under Bragg condition .....	31
4.2.4	Anisotropic interaction .....	34
4.2.5	Beam shaping and acoustic power .....	35
4.3	Design of a broadband AOFS .....	35
4.3.1	Uncorrected case .....	35
4.3.2	Principle of angular correction .....	37
4.3.3	Optimization of diffraction efficiency .....	38
4.3.4	Fiber coupling efficiency optimization .....	40
4.3.5	Optimized overall spectral transmittance .....	42
4.3.6	Further improvements .....	43
4.4	Prototype realization and characterization of spectral transmittance .....	45
4.5	Conclusion .....	47
<b>5</b>	<b>Dual beam heterodyne FDOCT</b>	<b>49</b>
5.1	Introduction .....	49
5.2	Method .....	50
5.2.1	FDOCT dual beam configuration .....	50
5.2.2	Heterodyne dual beam FDOCT .....	52
5.2.3	Sensitivity and dynamic range .....	52
5.3	Experimental .....	55
5.4	Applicators .....	57
5.4.1	Single mirror tip/tilt scanner .....	57
5.4.2	Endoscope probe .....	58
5.5	Results and discussion .....	59
5.6	Conclusion .....	64
<b>6</b>	<b>Phase stability</b>	<b>65</b>
6.1	Theory .....	65
6.2	Experimental .....	68
6.3	Conclusion .....	73



### Part III - Functional imaging with resonant Doppler FDOCT

<b>7</b>	<b>Introduction to functional ophthalmic imaging in FDOCT</b>	<b>79</b>
7.1	Physiology of the eye .....	79
7.1.1	Retina .....	79
7.1.2	Photoreceptors, phototransduction and color vision .....	80
7.2	Functional retinal imaging with FDOCT .....	81
<b>8</b>	<b>Resonant Doppler FDOCT</b>	<b>85</b>
8.1	Introduction .....	85
8.2	Theory .....	85
8.2.1	Chromatic interference fringe blurring .....	85
8.2.2	Signal recovery by reference phase tuning .....	88
8.2.3	Differential velocity mapping .....	90
8.3	Experimental .....	91
8.3.1	Setup.....	91
8.3.2	Detailed synchronization scheme.....	92
8.4	Results and discussion.....	94
8.5	Conclusion.....	99
<b>9</b>	<b>Outlook on optical testing of retinal physiology</b>	<b>101</b>
9.1	Introduction .....	101
9.2	Short review on light flicker stimulation.....	101
9.3	Light flicker stimulation.....	102
9.4	Measurements.....	103
9.5	Conclusion.....	105

### Part IV - Conclusion and outlook

<b>10</b>	<b>Conclusion</b>	<b>111</b>
<b>11</b>	<b>Outlook</b>	<b>113</b>

### Part V - Addendum

<b>A</b>	<b>Glossary – acronyms and medical terms</b>
<b>B</b>	<b>List of figures</b>
<b>C</b>	<b>List of tables</b>
<b>D</b>	<b>Scientific contributions</b>
<b>E</b>	<b>Acknowledgements</b>
<b>F</b>	<b>CV</b>



## **Part I**

### **General introduction**



## Chapter 1

### Introduction

Fourier domain optical coherence tomography (FDOCT) is a biomedical imaging modality which has gained in interest during the last few years and which has today attained widespread acceptance in the biomedical imaging community. The reason is its outstanding sensitivity allowing for high speed 2D and 3D *iv-vivo* imaging of weakly backscattering biological tissue with high axial resolution [1-7]. Today, FDOCT has largely replaced time domain OCT due to its marked advantages in sensitivity and acquisition speed [8-10]. In particular, for fast retinal *iv-vivo* imaging with high resolution in 3D, FDOCT has become the method of choice [11-13]. Recent developments enlarge the clinical and biomedical potential of FDOCT by aiming beyond purely structural to functional tissue imaging, thus enabling imaging of tissue dynamics and physiology. The imaging parameter space is becoming highly multi-dimensional including polarization [14-17], Doppler flow [17-22] and spectroscopy [23-25]. Recent developments based on swept-source technology achieve unprecedented depth scan speeds of several 100kHz with high phase accuracy [26-30].



**Figure I-1. Typical high resolution retinal tomogram with “empty” blood vessels (\*) in the optic nerve head region. Tomogram size: 12mm x 1mm (lateral x depth) with 8.5μm axial resolution (values: in air).**

Still, spectrometer-based FDOCT suffers from inherent imaging artifacts such as complex ambiguity, aliasing, signal decay with depth, and last but not least interference fringe blurring. A recent approach to reduce the latter effect for retinal imaging has been the application of pulsed illumination [31]. Interference fringe blurring in particular limits the detection of moving structures such as flow. Figure I-1 demonstrates a typical high resolution retinal tomogram with visible blood vessels. One can clearly observe vessel structures with internal blood flow as well as vessels which appear empty. Recovering the signal from within these pulsating vessels would give access to valuable information on retinal blood flow.

Complex ambiguity-free tomograms make it possible to situate the structure of interest in the measurement region of highest sensitivity and to increase the imaging depth by a factor of two [32-38]. Current phase shifting techniques mostly use piezo-electric actuators; this however leads to chromatic phase shifts with mediocre speed potential.

*This thesis introduces two new spectrometer-based FDOCT modalities, both based on the phase-sensitive nature of OCT. Appropriate locking of acquisition speed, exposure time and triggering onto artificially induced signal phase changes allows the additional degrees of freedom in signal detection to be exploited. Special attention is paid to spectrally broadband concepts, necessary for ultra-high axial resolution.*

This work is divided into five parts, each containing a number of chapters; Part II (Chapters 3 to 6) and Part III (Chapters 7 to 9) constitute the core of this thesis. These two distinct parts represent the author's main contributions to the scientific community in the field of OCT.

Chapter 2 intends to familiarize the reader with the general principles of FDOCT and gives an initial overview of literature related to this thesis. The heterodyne spectrometer-based FDOCT, introduced in Chapter 3, allows for achromatic phase-shifting by generating a stable beating frequency to which the detector can be locked. Then, extending the real-valued signal by a  $90^\circ$  phase-shifted copy allows ambiguity free reconstruction of the tomogram. Chapter 4 discusses the increase in spectral transmittance bandwidth of (fiberized) acousto-optic devices with the aim to enable the spectral bandwidth of the light source used to be preserved as far as possible throughout the whole OCT setup. This is especially important in OCT, since it is known that the axial resolution is inversely proportional to the width of the detected spectrum. Chapter 5 returns to the heterodyne spectrometer-based FDOCT and provides an extension to the concept so as to enable the use of long probing fibers with preserved high phase stability. Impact on sensitivity and dynamic range with respect to the standard method will be discussed. Chapter 6 concludes Part II with a discussion of phase stability issues with respect to the complex reconstruction scheme used in Chapters 3 and 5. In Part III, an extension from purely structural to functional imaging is made and illustrated experimentally for ophthalmology. Chapter 7 intends to introduce the reader to functional imaging. Chapter 8 then presents a novel signal recovery scheme for preventing interference fringe blurring which is based on well synchronized phase-shifting patterns, and then later illustrates the technique with *in-vivo* measurements made on the human retina. To conclude Part III a short outlook on optical testing of retinal physiology and initial implementation of light flicker stimulation are given in Chapter 9. Part IV, with Chapters 10 and 11, is devoted to a general conclusion of this thesis. Finally, Part V contains a glossary and the complete list of the author's scientific contributions.

## Chapter 2

### State of the art

#### 2.1 Short review – optical coherence tomography

Today, Fourier domain optical coherence tomography has obtained wide acceptance in the biomedical imaging community due to its resolution power and outstanding sensitivity enabling very high imaging speed [1-7, 9, 10]. In terms of resolution it outperforms other biomedical imaging methods like magnetic resonance imaging (MRI), computed tomography imaging (CTI) or ultrasound imaging (USI). Similar to USI it measures the delay of fields backscattered from tissue structure or material layers. Depending on the scattering characteristics of the sample being investigation and the employed wavelength, penetration depth can reach several millimeters.

In OCT, axial resolution or depth discrimination is based on coherence properties of the light as is the case for white light interferometry and low coherence interferometry (LCI), which was first applied for investigating technical samples. One of the first publications reporting on measurements of backscatter in optical fibers exploiting low-coherence properties in the time domain was published in 1976 by Barnoski *et al.* [39]. A review of early work in LCI leading from technical to biomedical applications in OCT was published by Masters [40] and reviews on OCT were published, among others, by Fercher *et al.* [41]. In retrospective, many concepts related to FDOCT can be found in the early literature [42-44]. However, only the recent massive technological progress in various domains from optics and fiber technology to electronics and last but not least computer technology propelled OCT to the performance appreciated today.

A first topographic image of the retinal pigment epithelium of the human eye was presented by Fercher and later published by Hitzenberger *et al.* [45-47]. The Fujimoto group pioneered fiber-based time domain OCT (TDOCT) [48-50] and first retinal tomograms measured *in vivo* were reported in 1993 by Fercher *et al.* [51] and Swanson *et al.* [49]. Shortly afterwards, first applications of optical coherence microscopy (OCM) were published by Izatt *et al.* [52, 53].

However, the principle limitation of TDOCT is that depth scanning is realized by axially displacing a mirror in the reference arm of the interferometer. Even though rapid scanning delay lines were developed and A-scan (axial scan) rates were increased [54], parallel imaging schemes were the only way to limit the signal to noise (*SNR*) degradation that comes with increased scanning speed [55]. A full tomographic volume could be recorded with a single depth scan using two-dimensional CMOS detectors with pixel-wise on-chip demodulation of the interferometric signal [56, 57].

Ultra-high resolution (UHR) OCT was first presented by Drexler *et al.* in 2001 [58, 59], revealing structural details down to cellular level and retinal tomograms comparable in details with histology. However, in TDOCT, larger optical bandwidth imposes reduced scanning speed in order to maintain sufficient *SNR* [60], whereas FDOCT keeps its sensitivity independent of the detected spectral bandwidth [9].

Improved CCD detector technology boosted spectrometer-based FDOCT especially in the near infrared (NIR) range around 800nm. A-scan rates of several tens of *kHz* and therefore reduced motion artifacts allowed recording full 3D volumes *in vivo* at unsurpassed axial resolution of about 2 $\mu$ m [4, 5, 7].

Increased imaging speed also paved the way for functional imaging and resolving tissue dynamics [19-21]. Polarization [14-17], spectroscopic [23, 24] and molecular contrast [61, 62] extend the imaging parameter-space in OCT and allow, in latter case, visualization of specific biochemical processes in a target specimen.

If deeper penetration depths into the tissue are desired at the expense of ultra-high axial resolution, light sources with longer wavelengths above one micrometer are employed [16, 26, 27]. Very rapidly tunable light sources were developed especially in the telecom wavelength range achieving “A-scan” rates of several hundred *kHz* [28-30, 63]. Instead of recording the signal in parallel on a spectrometer, the spectrum is swept temporally. Principally, these swept source systems are equivalent in terms of *SNR* compared to spectrometer-based FDOCT and share the same advantages over TDOCT [6, 9, 10]. But a big advantage of swept-source FDOCT is that a single point detector replaces the spectrometer’s array detector, latter becoming expensive for this wavelength range.

In the meantime, OCT has become a mature measuring and imaging method. As a matter of fact, the number of publications in the field of OCT increased until 2005 and peaked at almost 1’000 papers per year [64]. The number of patents on its turn is still increasing in parallel with the number of new companies offering commercial OCT systems. Today, 19 companies are provide OCT-related products and one third of them are focusing on ophthalmology. Other fields include vascular, cancer and dental applications [65].

## 2.2 Basic FDOCT theory

### 2.2.1 Fourier transform for accessing structural information

FDOCT is an interferometric measurement method. Its principle is based on the inverse scattering theorem and the fact that the spectral power amplitude of the backscattered wave equals the Fourier transform (*FT*) of the axial distribution of the object scattering potential (Wiener-Khintchine theorem) [1, 41]. The full sample depth structure is obtained in a parallel way: it is encoded as depth dependent modulation of the light source spectrum [1-3]. The accessible depth information can be described by the *FT* of the power spectral density function  $I(\nu)$ :



$$\begin{aligned}
FT\{I(\nu)\} &= FT\left\{I_R(\nu) + \sum_i I_{S,i}(\nu) + 2 \sum_{i,j;i \neq j} \sqrt{I_{S,i}(\nu)I_{S,j}(\nu)} \cos(\Psi_{i,j}) + \right. \\
&\quad \left. + 2 \sum_i \sqrt{I_R(\nu)I_{S,i}(\nu)} \cos(\Psi_{R,i})\right\}, \quad (I.1) \\
&= \Gamma_{RR}(\tau) + \sum_i \Gamma_{ii}(\tau) + \sum_{i,j;i \neq j} \left\{ \Gamma[\tau + (\tau_j - \tau_i)] + \Gamma[\tau - (\tau_j - \tau_i)] \right\} + \\
&\quad + \sum_i \left\{ \Gamma[\tau + (\tau_R - \tau_i)] + \Gamma[\tau - (\tau_R - \tau_i)] \right\}
\end{aligned}$$

with  $\tau$  the time variable,  $\nu$  the optical frequency and the indices  $i,j$  running over different sample scattering sites in depth.  $\Gamma(\tau_i)$  represents the first-order electric field correlation-function  $\Gamma(\tau_i) \equiv \langle E(\tau)E^*(\tau + \tau_i) \rangle$  [66]. The first two terms are the unmodulated intensity terms of the reference ( $I_R$ ) and sample signal ( $\sum I_{S,i}$ ) respectively, also named DC terms. They are centered at the relative zero-delay or zero optical path length difference of the interferometric signal ( $\Gamma_{RR}$ ,  $\sum \Gamma_{ii}$ ). The third term is an unwanted autocorrelation term and can be seen as coherent noise which has to be suppressed – if visible – for proper structural imaging [3].

The structural information can be deduced from the fourth and last component in the sum of correlation terms in Equation (I.1), the cross-correlation terms. They are modulated encoding a relative optical path length difference between the reference ( $R$ ) and different sample scattering sites. The cross-correlation terms are, however, mirrored about the zero-delay, because of the Hermitian symmetry of the recorded real-valued spectral signal. Thus it produces a complex conjugate artifact, mixing with the desired true image as mirrored structure about the relative zero-phase delay in the entire complex space. Hence, positive and negative relative distances can not be distinguished, leading to the common practice to carefully locate the sample structure above or below the zero-delay line in order to prevent overlapping of the image with its conjugate counterpart.

It is important to note that the Fourier transform in Equation (I.1) is performed in function of spectral frequency and not of wavelength. Since the recorded signal at the spectrometer is not linear in frequency, it is mapped into frequency space by interpolation prior to  $FT$  [3, 5]. After  $FT$  the structure signal is deduced representing one depth or “A-scan” respectively. With the relation  $\Delta z = c \tau = \lambda \nu \tau$  optical path length differences are revealed rather than temporal delays (Equation (I.1)), with  $c$  being the speed of light inside the medium. In order to achieve complete 3D structure information, generally a 2D lateral scan is performed with two orthogonal galvanic scanners.

### 2.2.2 Depth range, lateral and axial resolution

The depth range which can be probed in parallel in FDOCT is dependent on the spectrometer resolution and detector size (number of pixel). For classical FDOCT depth range is defined as

$$l_{max} = \frac{1}{4n} \frac{\lambda_0^2}{\Delta \lambda_{Spec}} N, \quad (I.2)$$

with  $n$  being the refractive index of the medium,  $\lambda_0$  the central wavelength of the detected spectrum,  $\Delta\lambda_{spec}$  the spectrometer bandwidth and  $N$  the number of pixels. For ambiguity free tomograms this depth range is doubled.  $(\Delta\lambda_{spec}/N)^{-1}$  can also be seen as the inverse of the spectral resolution power  $\delta\lambda^{-1}$  of the detecting spectrometer (without accounting for non-linear dispersion by the spectrometer diffraction grating).  $\delta\lambda^{-1}$  is proportional to the coherence length of the detected spectral channel and therefore in part responsible for the signal decay observed for structures far away from the relative zero-delay.

Equation (I.2) describes the depth range with respect to the coherence length of the light detected by a spectral channel of the spectrometer. From a geometric point of view depth range is also limited by – in most cases – Gaussian beam propagation or image formation relations since OCT setups are usually confocal. Illuminating the sample with a Gaussian beam, the depth of focus ( $DOF$ ) is defined by twice the Rayleigh range, reading [67]

$$DOF = 2z_0 = \frac{2\pi w_0^2}{\lambda_0}, \quad (I.3)$$

with  $w_0$  the beam waist defined by

$$w_0 = \frac{\lambda_0}{\pi NA}, \quad (I.4)$$

where  $NA$  is the numerical aperture of the illuminating beam. A measure for the lateral resolution is the  $1/e^2$ -intensity spot size given by  $2w_0$ .

The axial resolution in OCT is independent of the degree of confocality and only defined by the coherence length  $l_c$  of the detected light spectrum:

$$n\delta z = \frac{l_c}{2} = \frac{2 \ln 2}{\pi} \frac{\lambda_0^2}{\Delta\lambda}, \quad (I.5)$$

where a Gaussian spectral density was assumed.

### 2.2.3 Signal-to-noise ratio and sensitivity

System sensitivity is a very important parameter. Besides other advantages it enables 3D *in-vivo* imaging. The speed advantage of FDOCT as compared to the former TDOCT method [41] is apparent since no mechanical depth scanning is needed and the whole depth information along one line is acquired in parallel [6, 9, 10].

Sensitivity is the smallest detectable sample reflectivity where the signal-to-noise ratio  $SNR \equiv 1$ . Leitgeb *et al.* [9] showed that excess noise plays no dominant role in spectrometer-based FDOCT and therefore sensitivity can be described in the shot-noise limit by

$$S = \frac{SNR}{R_S} \bigg|_{SNR \equiv 1} \approx \frac{\frac{1}{N} \left( \frac{\rho \eta \tau}{h\nu_0} P_0 \right)^2 \gamma_S \gamma_R R_R}{\frac{\rho \eta \tau}{h\nu_0} \frac{P_0}{N} \gamma_R R_R + \sigma_{receiver}^2} \quad \text{for } R_S \ll R_R, \quad (I.6)$$

where  $\rho$  is the spectrometer efficiency,  $\eta$  the quantum efficiency of the detector,  $\tau$  the integration time,  $h\nu_0$  the photon energy,  $P_0$  the source power illuminating the interferometer and  $\sigma_{receiver}^2$  the receiver noise. The fraction of light incident on the detector, for the reference

and sample arm respectively, can be expressed as  $R_R\gamma_R=P_R/P_0$  and  $R_S\gamma_S=P_S/P_0$ , with  $P_R$  and  $P_S$  the respectively measured power at the spectrometer exit.

Like in TDOCT the axial resolution increases with the optical bandwidth of the employed light source. However the achievable sensitivity of TDOCT decreases in the shot noise limit with increasing spectral width, *i.e.* with increasing axial resolution, due to the dependency of electronic detection bandwidth on the optical spectral bandwidth [60]. But sensitivity of FDOCT on the other hand is independent of the spectral bandwidth as can be seen from Equation (I.6). This results in a sensitivity improvement with respect to TDOCT of two orders of magnitude or  $>20dB$ , independent of the detected spectral bandwidth [6, 9, 10, 68].

## 2.3 Phase shifting in FDOCT

### 2.3.1 Introduction

The power spectral density function  $I(\nu)$  detected by the spectrometer (Equation (I.1)), taking into account only the cross-correlation terms (subsequently we will denominate the cross-correlation terms as AC signal terms), can be written in  $k$ -space as  $k=2\pi\nu/c$ :

$$I_{AC}(k) = 2 \sum_i \sqrt{I_R(k) I_{S,i}(k)} \cos(\Psi_i), \quad (I.7)$$

with  $I_R$  and  $I_S$  the detected reference and sample light intensities respectively and  $\Psi_i$  containing all structure phase terms. Movement of the reference mirror (or the sample, what is in fact equivalent) smaller than the axial resolution of the system results in a signal phase change rather than a significant change of the modulation frequency (carrying the depth information). This phase change can be represented as a sum in the argument of the cosine function in Equation (I.7) reading  $\Psi_i+d\varphi$ , with  $d\varphi$  accounting for the small path length difference. Introducing such phase changes on purpose and in a controlled manner is commonly known in interferometry as phase shifting [69]. Most phase shifting methods used today in OCT are more or less equivalent to classical optical interferometry and aim to remove complex ambiguity as described in §2.2.1. Starting with the simplest solution, discretely stepped [32, 33, 37, 70, 71] or continuously moved piezo-electric transducers (PZT) [72-74], electro-optic modulators (EOM) [34-36] and acousto-optic frequency shifters (AOFS) [38, 75] are used for externally introducing phase shifts on purpose. Instantaneous phase-shifted copies of the power spectral density function can be detected using 3x3 fiber interferometers [76, 77], reference wave front tilting [78] or using polarization encoding [79]. Depending on the method, reconstruction of the complex spectrogram is achieved differently, *e.g.* integrating bucket algorithms [73] or harmonic lock-in detection of sinusoidal reference modulation [74]. In this thesis, phase shifting techniques using AOFS and EOM will be employed. Both methods will perform phase shifts during acquisition, resulting in integrating buckets. However, no elaborate complex-valued signal reconstruction algorithms will be used as originally introduced for integrating bucket interferometry by Sasaki and Okazaki [80] (see Chapters 3 and 5 in Part II).

### 2.3.2 Color Doppler FDOCT

Fourier transformation of a (real) signal results in a complex function which can therefore be represented by its amplitude and phase. Phase information can be revealed by simply choosing the complex argument after Fourier transform:  $\angle\{FT\{\bullet\}\}$ . Thus, the differential

phase value between two successive frames recorded with a temporal delay of  $\Delta t$  can be expressed as:

$$\Delta\varphi(z, \Delta t) = \angle \left\{ FT \left\{ I(k, t = t_0) \right\} \right\} - \angle \left\{ FT \left\{ I(k, t = t_0 + \Delta t) \right\} \right\}. \quad (\text{I.8})$$

With the axial phase information localized at each measurement point, a relative phase change  $\Delta\varphi(z, \Delta t)$  between two adjacent frames after  $FT$  gives access to the Doppler shift. Leitgeb *et al.* [81] showed the potential of this Doppler shift in FDOCT by measuring the flow profiles of small blood vessels. The detected speed is given by

$$v(z) = \frac{\Delta\varphi(z, \Delta t)}{\Delta t \cos(\theta)} \frac{\lambda}{4\pi}, \quad (\text{I.9})$$

with  $\theta$  the angle between the flow vector and the optical axis and  $\Delta t$  the time period between the two acquisitions, which is in general given by the read out rate of the camera:  $\Delta t = T$ . A convenient way to calculate the phase change at each position in depth was proposed by Wang *et al.* [82].

For reliable phase change retrieval it is necessary to have at least two data points within  $\pm\pi$ . The corresponding maximal accessible longitudinal velocity component is obtained with  $\Delta\varphi_{\max} = \pm\pi$ :

$$v_{\max}(z) = \pm \frac{\lambda}{4T_{\min}}, \quad (\text{I.10})$$

with  $T_{\min} = f_{\text{CCD}}^{-1}$  the highest camera speed. The smallest resolvable velocity is given by the phase noise present in the system [22, 83]. The phase noise is taken as the standard deviation of phases  $\sigma_{\Delta\varphi}$  evaluated at an interface at rest:

$$v_{\min}(z) = \pm \frac{\sigma_{\Delta\varphi}(z, T)}{T} \frac{\lambda}{4\pi}. \quad (\text{I.11})$$

In contrast to TDOCT, in FDOCT no moving reference arm has to be used and therefore phase stability is inherently increased. Several papers discussed phase-sensitive measurements and related phase errors in FDOCT, including [16, 22, 83-87] (see also Chapter 6 in Part II). Color Doppler measurements can be used in a multitude of biological applications like small animal imaging, dermatology and ophthalmology (see also Part III).

In addition, phase information combined from two neighboring measurement points allows phase contrast measurements [88]. Analyses of cellular dynamics were performed using FDOCT revealing changes in cell thickness on a sub-micrometer scale associated with spontaneous cardiomyocyte contraction [86].

#### References:

1. A. F. Fercher, C. K. Hitzenberger, G. Kamp, and S. Y. Elzaiat, "Measurement of Intraocular Distances by Backscattering Spectral Interferometry," *Opt. Commun.* **117**, 43-48 (1995).
2. G. Hausler, and M. W. Lindner, "Coherence radar and spectral radar-new tools for dermatological diagnosis," *J. Biomed. Opt.* **3**, 21-31 (1998).
3. M. Wojtkowski, R. Leitgeb, A. Kowalczyk, T. Bajraszewski, and A. F. Fercher, "In vivo human retinal imaging by Fourier domain optical coherence tomography," *J. Biomed. Opt.* **7**, 457-463 (2002).

4. M. Wojtkowski, V. J. Srinivasan, T. H. Ko, J. G. Fujimoto, A. Kowalczyk, and J. S. Duker, "Ultrahigh-resolution, high-speed, Fourier domain optical coherence tomography and methods for dispersion compensation," *Opt. Express* **12**, 2404-2422 (2004).
5. R. A. Leitgeb, W. Drexler, A. Unterhuber, B. Hermann, T. Bajraszewski, T. Le, A. Stingl, and A. F. Fercher, "Ultrahigh resolution Fourier domain optical coherence tomography," *Opt. Express* **12**, 2156-2165 (2004).
6. M. A. Choma, M. V. Sarunic, C. H. Yang, and J. A. Izatt, "Sensitivity advantage of swept source and Fourier domain optical coherence tomography," *Opt. Express* **11**, 2183-2189 (2003).
7. N. A. Nassif, B. Cense, B. H. Park, M. C. Pierce, S. H. Yun, B. E. Bouma, G. J. Tearney, T. C. Chen, and J. F. de Boer, "In vivo high-resolution video-rate spectral-domain optical coherence tomography of the human retina and optic nerve," *Opt. Express* **12**, 367-376 (2004).
8. N. Nassif, B. Cense, B. H. Park, S. H. Yun, T. C. Chen, B. E. Bouma, G. J. Tearney, and J. F. de Boer, "In vivo human retinal imaging by ultrahigh-speed spectral domain optical coherence tomography," *Opt. Lett.* **29**, 480-482 (2004).
9. R. Leitgeb, C. K. Hitzenberger, and A. F. Fercher, "Performance of fourier domain vs. time domain optical coherence tomography," *Opt. Express* **11**, 889-894 (2003).
10. J. F. de Boer, B. Cense, B. H. Park, M. C. Pierce, G. J. Tearney, and B. E. Bouma, "Improved signal-to-noise ratio in spectral-domain compared with time-domain optical coherence tomography," *Opt. Lett.* **28**, 2067-2069 (2003).
11. M. Wojtkowski, V. Srinivasan, J. G. Fujimoto, T. Ko, J. S. Schuman, A. Kowalczyk, and J. S. Duker, "Three-dimensional retinal imaging with high-speed ultrahigh-resolution optical coherence tomography," *Ophthalmology* **112**, 1734-1746 (2005).
12. U. Schmidt-Erfurth, R. A. Leitgeb, S. Michels, B. Povazay, S. Sacu, B. Hermann, C. Ahlers, H. Sattmann, C. Scholda, A. F. Fercher, and W. Drexler, "Three-dimensional ultrahigh-resolution optical coherence tomography of macular diseases," *Invest Ophthalmol Vis Sci* **46**, 3393-3402 (2005).
13. R. Leitgeb, L. Schmetterer, W. Drexler, F. Berisha, C. Hitzenberger, M. Wojtkowski, T. Bajraszewski, and A. F. Fercher, "Real-time measurement of in-vitro and in-vivo blood flow with Fourier domain optical coherence tomography," in *Coherence Domain Optical Methods And Optical Coherence Tomography In Biomedicine Viii* (Spie-Int Society Optical Engineering, Bellingham, 2004), pp. 141-146.
14. E. Gotzinger, M. Pircher, and C. K. Hitzenberger, "High speed spectral domain polarization sensitive optical coherence tomography of the human retina," *Opt. Express* **13**, 10217-10229 (2005).
15. Y. Yasuno, S. Makita, Y. Sutoh, M. Itoh, and T. Yatagai, "Birefringence imaging of human skin by polarization-sensitive spectral interferometric optical coherence tomography," *Opt. Lett.* **27**, 1803-1805 (2002).
16. B. H. Park, M. C. Pierce, B. Cense, S. H. Yun, M. Mujat, G. J. Tearney, B. E. Bouma, and J. F. de Boer, "Real-time fiber-based multi-functional spectral-domain optical coherence tomography at 1.3  $\mu\text{m}$  ," *Opt. Express* **13**, 3931-3944 (2005).
17. S. Makita, Y. Yasuno, T. Endo, M. Itoh, and T. Yatagai, "Polarization contrast imaging of biological tissues by polarization-sensitive Fourier-domain optical coherence tomography " *Applied Optics* **45**, 1142-1147 (2006).
18. R. A. Leitgeb, L. Schmetterer, C. K. Hitzenberger, A. F. Fercher, F. Berisha, M. Wojtkowski, and T. Bajraszewski, "Real-time measurement of in vitro flow by Fourier-domain color Doppler optical coherence tomography," *Opt. Lett.* **29**, 171-173 (2004).
19. R. A. Leitgeb, L. Schmetterer, W. Drexler, A. F. Fercher, R. J. Zawadzki, and T. Bajraszewski, "Real-time assessment of retinal blood flow with ultrafast acquisition by color Doppler Fourier domain optical coherence tomography," *Opt. Express* **11**, 3116-3121 (2003).
20. B. R. White, M. C. Pierce, N. Nassif, B. Cense, B. H. Park, G. J. Tearney, B. E. Bouma, T. C. Chen, and J. F. de Boer, "In vivo dynamic human retinal blood flow imaging using ultra-high-speed spectral domain optical Doppler tomography," *Opt. Express* **11**, 3490-3497 (2003).
21. S. Makita, Y. Hong, M. Yamanari, T. Yatagai, and Y. Yasuno, "Optical coherence angiography," *Opt. Express* **14**, 7821-7840 (2006).
22. M. A. Choma, A. K. Ellerbee, S. Yazdanfar, and J. A. Izatt, "Doppler flow imaging of cytoplasmic streaming using spectral domain phase microscopy," *J. Biomed. Opt.* **11** (2006).
23. R. Leitgeb, M. Wojtkowski, A. Kowalczyk, C. K. Hitzenberger, M. Sticker, and A. F. Fercher, "Spectral measurement of absorption by spectroscopic frequency-domain optical coherence tomography," *Opt. Lett.* **25**, 820-822 (2000).
24. R. Leitgeb, M. Wojtkowski, C. Hitzenberger, A. Fercher, and H. Sattmann, "Spectroscopic analysis of substances by frequency domain Optical Coherence Tomography," in *Coherence Domain Optical Methods*

- In Biomedical Science And Clinica Applications V*(Spie-Int Society Optical Engineering, Bellingham, 2001), pp. 123-127.
25. R. A. Leitgeb, W. Drexler, B. Povazay, B. Hermann, H. Sattmann, and A. F. Fercher, "Spectroscopic Fourier domain optical coherence tomography: Principle, limitations, and applications," in *Progress in Biomedical Optics and Imaging - Proceedings of SPIE*(2005), pp. 151-158.
  26. S. H. Yun, C. Boudoux, G. J. Tearney, and B. E. Bouma, "High-speed wavelength-swept semiconductor laser with a polygon-scanner-based wavelength filter," *Opt. Lett.* **28**, 1981-1983 (2003).
  27. M. A. Choma, K. Hsu, and J. A. Izatt, "Swept source optical coherence tomography using an all-fiber 1300-nm ring laser source," *J Biomed Opt* **10**, 44009 (2005).
  28. R. Huber, D. C. Adler, and J. G. Fujimoto, "Buffered Fourier domain mode locking: unidirectional swept laser sources for optical coherence tomography imaging at 370,000 lines/s," *Opt. Lett.* **31**, 2975-2977 (2006).
  29. R. Huber, M. Wojtkowski, and J. G. Fujimoto, "Fourier Domain Mode Locking (FDML): A new laser operating regime and applications for optical coherence tomography," *Opt. Express* **14**, 3225-3237 (2006).
  30. D. C. Adler, R. Huber, and J. G. Fujimoto, "Phase-sensitive optical coherence tomography at up to 370,000 lines per second using buffered Fourier domain mode-locked lasers," *Opt. Lett.* **32**, 626-628 (2007).
  31. J. W. You, T. C. Chen, M. Mujat, B. H. Park, and J. F. de Boer, "Pulsed illumination spectral-domain optical coherence tomography for human retinal imaging," *Opt. Express* **14**, 6739-6748 (2006).
  32. A. F. Fercher, R. Leitgeb, C. K. Hitzenberger, H. Sattmann, and M. Wojtkowski, "Complex spectral interferometry OCT," in *Medical Applications Of Lasers In Dermatology, Cardiology, Ophthalmology, And Dentistry Ii, Proceedings Of*(1999), pp. 173-178.
  33. M. Wojtkowski, A. Kowalczyk, R. Leitgeb, and A. F. Fercher, "Full range complex spectral optical coherence tomography technique in eye imaging," *Opt. Lett.* **27**, 1415-1417 (2002).
  34. E. Gotzinger, M. Pircher, R. A. Leitgeb, and C. K. Hitzenberger, "High speed full range complex spectral domain optical coherence tomography," *Opt. Express* **13**, 583-594 (2005).
  35. J. Zhang, W. G. Jung, J. S. Nelson, and Z. P. Chen, "Full range polarization-sensitive Fourier domain optical coherence tomography," *Opt. Express* **12**, 6033-6039 (2004).
  36. J. Zhang, J. S. Nelson, and Z. P. Chen, "Removal of a mirror image and enhancement of the signal-to-noise ratio in Fourier-domain optical coherence tomography using an electro-optic phase modulator," *Opt. Lett.* **30**, 147-149 (2005).
  37. R. A. Leitgeb, C. K. Hitzenberger, A. F. Fercher, and T. Bajraszewski, "Phase-shifting algorithm to achieve high-speed long-depth-range probing by frequency-domain optical coherence tomography," *Opt. Lett.* **28**, 2201-2203 (2003).
  38. A. H. Bachmann, R. A. Leitgeb, and T. Lasser, "Heterodyne Fourier domain optical coherence tomography for full range probing with high axial resolution," *Opt. Express* **14**, 1487-1496 (2006).
  39. M. K. Barnoski, and S. M. Jensen, "FIBER WAVEGUIDES: A NOVEL TECHNIQUE FOR INVESTIGATING ATTENUATION CHARACTERISTICS," *Applied Optics* **15**, 2112-2115 (1976).
  40. B. R. Masters, "Early development of optical low-coherence reflectometry and some recent biomedical applications," *J. Biomed. Opt.* **4**, 236-247 (1999).
  41. A. F. Fercher, W. Drexler, C. K. Hitzenberger, and T. Lasser, "Optical coherence tomography - principles and applications," *Rep. Prog. Phys.* **66**, 239-303 (2003).
  42. P. Connes, "EARLY HISTORY OF FOURIER TRANSFORM SPECTROSCOPY," *Infrared Physics* **24**, 69-93 (1983).
  43. H. Fizeau, and L. Foucault, *C.r. Acad. Sci. Paris* **21** (1845).
  44. C. Froehly, A. Lacourt, and J. C. Vienot, "Time Impulse Response and Time Frequency Response of Optical Pupils. Experimental Confirmations and Applications," *NOTIONS DE REPONSE IMPULSIONNELLE ET DE FONCTION DE TRANSFERT TEMPORELLES DES PUPILLES OPTIQUES, JUSTIFICATIONS EXPERIMENTALES ET APPLICATIONS.* **4**, 183-196 (1973).
  45. C. K. Hitzenberger, W. Drexler, and A. F. Fercher, "Measurement of Corneal Thickness by Laser Doppler Interferometry," *Investigative Ophthalmology & Visual Science* **33**, 98-103 (1992).
  46. C. K. Hitzenberger, "Measurement of Corneal Thickness by Low-Coherence Interferometry," *Applied Optics* **31**, 6637-6642 (1992).
  47. C. K. Hitzenberger, "Optical Measurement of the Axial Eye Length by Laser Doppler Interferometry," *Investigative Ophthalmology & Visual Science* **32**, 616-624 (1991).
  48. D. Huang, E. A. Swanson, C. P. Lin, J. S. Schuman, W. G. Stinson, W. Chang, M. R. Hee, T. Flotte, K. Gregory, C. A. Puliafito, and J. G. Fujimoto, "Optical Coherence Tomography," *Science* **254**, 1178-1181 (1991).
  49. E. A. Swanson, J. A. Izatt, M. R. Hee, D. Huang, C. P. Lin, J. S. Schuman, C. A. Puliafito, and J. G. Fujimoto, "In vivo retinal imaging by optical coherence tomography," *Opt. Lett.* **18**, 1864-1869 (1993).

50. J. A. Izatt, M. R. Hee, D. Huang, E. A. Swanson, C. P. Lin, J. S. Schuman, C. A. Puliafito, and J. G. Fujimoto, "Micron-resolution biomedical imaging with optical coherence tomography," *Opt. Photon. News* **4**, 14-19 (1993).
51. A. F. Fercher, C. K. Hitzenberger, W. Drexler, G. Kamp, and H. Sattmann, "In-Vivo Optical Coherence Tomography," *Am. J. Ophthalmol.* **116**, 113-115 (1993).
52. J. A. Izatt, M. R. Hee, G. M. Owen, E. A. Swanson, and J. G. Fujimoto, "Optical coherence microscopy in scattering media," *Opt. Lett.* **19**, 590-592 (1994).
53. J. A. Izatt, M. D. Kulkarni, H. W. Wang, K. Kobayashi, and M. V. Sivak Jr, "Optical coherence tomography and microscopy in gastrointestinal tissues," *IEEE Journal on Selected Topics in Quantum Electronics* **2**, 1017-1028 (1996).
54. G. J. Tearney, B. E. Bouma, and J. G. Fujimoto, "High-speed phase- and group-delay scanning with a grating-based phase control delay line," *Opt. Lett.* **22**, 1811-1813 (1997).
55. A. Dubois, L. Vabre, A. C. Boccara, and E. Beaurepaire, "High-resolution full-field optical coherence tomography with a Linnik microscope," *Applied Optics* **41**, 805-812 (2002).
56. M. Laubscher, M. Ducros, B. Karamata, T. Lasser, and R. Salathe, "Video-rate three-dimensional optical coherence tomography," *Opt. Express* **10**, 429-435 (2002).
57. M. Ducros, M. Laubscher, B. Karamata, S. Bourquin, T. Lasser, and R. P. Salathe, "Parallel optical coherence tomography in scattering samples using a two-dimensional smart-pixel detector array," *Opt. Commun.* **202**, 29-35 (2002).
58. W. Drexler, U. Morgner, R. K. Ghanta, F. X. Kärtner, J. S. Schuman, and J. G. Fujimoto, "Ultrahigh-resolution ophthalmic optical coherence tomography," *Nat Med* **7**, 502-507 (2001).
59. W. Drexler, "Ultrahigh-resolution optical coherence tomography," *J. Biomed. Opt.* **9**, 47-74 (2004).
60. A. M. Rollins, and J. A. Izatt, "Optimal interferometer designs for optical coherence tomography," *Opt. Lett.* **24**, 1484-1486 (1999).
61. B. E. Applegate, C. Yang, and J. A. Izatt, "Theoretical comparison of the sensitivity of molecular contrast optical coherence tomography techniques," *Opt. Express* **13**, 8146-8163 (2005).
62. B. E. Applegate, and J. A. Izatt, "Molecular imaging of endogenous and exogenous chromophores using ground state recovery pump-probe optical coherence tomography," *Opt. Express* **14**, 9142-9155 (2006).
63. R. Huber, M. Wojtkowski, J. G. Fujimoto, J. Y. Jiang, and A. Cable, "Three-dimensional and C-mode OCT imaging with a compact, frequency swept laser source at 1300 nm," *Opt. Express* **13**, 10523-10538 (2006).
64. R. A. Leitgeb, "Paradigm shifts in optical coherence tomography," in *SPIE Conference on Optical Metrology* (Munich, 2007).
65. T. Freeman, "OCT moves beyond the tipping point," (Optics Org, 2007), <http://optics.org/cws/article/industry/27518>.
66. J. W. Goodman, *Statistical Optics* (Wiley and Sons Inc, New York, 1995).
67. B. E. A. Saleh, and M. C. Teich, *Fundamentals of Photonics* (John Wiley & Sons, Inc., New York, 1991).
68. B. Cense, N. A. Nassif, T. C. Chen, M. C. Pierce, S. H. Yun, B. H. Park, B. E. Bouma, G. J. Tearney, and J. F. De Boer, "Ultrahigh-resolution high-speed retinal imaging using spectral-domain optical coherence tomography," *Opt. Express* **12**, 2435-2447 (2004).
69. P. Hariharan, *Optical Interferometry* (Elsevier, Amsterdam, 2003).
70. P. Targowski, M. Wojtkowski, A. Kowalczyk, T. Bajraszewski, M. Szkulmowski, and W. Gorczynska, "Complex spectral OCT in human eye imaging in vivo," *Opt. Commun.* **229**, 79-84 (2004).
71. J. Schmit, and K. Creath, "Extended Averaging Technique for Derivation of Error-Compensating Algorithms in Phase-Shifting Interferometry," *Applied Optics* **34**, 3610-3619 (1995).
72. R. K. Wang, "In vivo full range complex Fourier domain optical coherence tomography," *Appl. Phys. Lett.* **90** (2007).
73. Y. K. Tao, M. Zhao, and J. A. Izatt, "Complex Conjugate RESolved Retinal SDOCT using Integrating Buckets," in *SPIE Coherence Domain Optical Methods and Optical Coherence Tomography in Biomedicine XI* (San Jose, 2007).
74. A. B. Vakhtin, K. A. Peterson, and D. J. Kane, "Resolving the complex conjugate ambiguity in Fourier-domain OCT by harmonic lock-in detection of the spectral interferogram," *Opt. Lett.* **31**, 1271-1273 (2006).
75. A. M. Davis, M. A. Choma, and J. A. Izatt, "Heterodyne swept-source optical coherence tomography for complete complex conjugate ambiguity removal," *J. Biomed. Opt.* **10** (2005).
76. M. V. Sarunic, M. A. Choma, C. H. Yang, and J. A. Izatt, "Instantaneous complex conjugate resolved spectral domain and swept-source OCT using 3x3 fiber couplers," *Opt. Express* **13**, 957-967 (2005).
77. M. V. Sarunic, B. E. Applegate, and J. A. Izatt, "Real-time quadrature projection complex conjugate resolved Fourier domain optical coherence tomography," *Opt. Lett.* **31**, 2426-2428 (2006).

78. Y. Yasuno, S. Makita, T. Endo, G. Aoki, H. Sumimura, M. Itoh, and T. Yatagai, "One-shot-phase-shifting Fourier domain optical coherence tomography by reference wavefront tilting," *Opt. Express* **12**, 6184-6191 (2004).
79. B. J. Vakoc, S. H. Yun, G. J. Tearney, and B. E. Bouma, "Elimination of depth degeneracy in optical frequency-domain imaging through polarization-based optical demodulation," *Opt. Lett.* **31**, 362-364 (2006).
80. M. Sasaki, and H. Okazaki, "Sinusoidal phase modulating interferometry for surface profile measurement," *Applied Optics* **25**, 3137-3140 (1986).
81. R. Leitgeb, L. Schmetterer, M. Wojtkowski, C. K. Hitzenberger, M. Stricker, and A. F. Fercher, "Flow Velocity Measurement by Frequency Domain Short Coherence Interferometry," in *Coherence Domain Optical Methods And Optical Coherence Tomography In Biomedicine Vi*(2002), pp. 16-21.
82. L. Wang, Y. Wang, S. Guo, J. Zhang, M. Bachman, G. P. Li, and Z. Chen, "Frequency domain phase-resolved optical Doppler and Doppler variance tomography," *Opt. Commun.* **242**, 345-350 (2004).
83. S. Yazdanfar, C. Yang, M. V. Sarunic, and J. A. Izatt, "Frequency estimation precision in Doppler optical coherence tomography using the Cramer-Rao lower bound," *Opt. Express* **13**, 410-416 (2005).
84. A. K. Ellerbee, and J. A. Izatt, "Phase retrieval in low-coherence interferometric microscopy," *Opt. Lett.* **32**, 388-390 (2007).
85. S. H. Yun, G. J. Tearney, J. F. de Boer, and B. E. Bouma, "Motion artifacts in optical coherence tomography with frequency-domain ranging," *Opt. Express* **12**, 2977-2998 (2004).
86. M. A. Choma, A. K. Ellerbee, C. H. Yang, T. L. Creazzo, and J. A. Izatt, "Spectral-domain phase microscopy," *Opt. Lett.* **30**, 1162-1164 (2005).
87. B. J. Vakoc, S. H. Yun, J. F. De Boer, G. J. Tearney, and B. E. Bouma, "Phase-resolved optical frequency domain imaging," *Opt. Express* **13**, 5483-5493 (2005).
88. C. Joo, T. Akkin, B. Cense, B. H. Park, and J. F. De Boer, "Spectral-domain optical coherence phase microscopy for quantitative phase-contrast imaging," *Opt. Lett.* **30**, 2131-2133 (2005).



## **Part II**

# **Heterodyne spectrometer-based Fourier domain optical coherence tomography**



## Chapter 3

### Heterodyne FDOCT

#### 3.1 Introduction\*

Part I introduced the general principles of Fourier domain optical coherence tomography (FDOCT) with emphasis on spectrometer-based FDOCT. We have seen that axial resolution, completely independent of lateral resolution, improves with increasing bandwidth of the employed light source. It was also stated that spectrometer-based FDOCT has still an advantage in axial resolution as compared to swept-source FDOCT. Today, tunable lasers achieve considerably higher scan rates than line detectors and therefore spectrometer-based FDOCT is more focused on high and ultra-high resolution applications in the near infrared (NIR around 800nm) and visible spectral range (VIS), both spectral regions not easily accessible to swept-source FDOCT. In consequence, rather large spectral bandwidths, suitable for axial resolutions below 5  $\mu\text{m}$ , are of main interest for spectrometer-based FDOCT.

In order to prevent truncation of the light spectrum by the finite size of the spectrometer line detector, the spatial extent of the spectrum after dispersion by the diffraction grating and focusing must be matched to the width of the detector. This defines the spectral width seen by one pixel, known as the spectrometer spectral resolution; it is obvious that the grating must support this spectral resolution as well. The spectral width of one spectral channel is defined as  $\delta\lambda = \Delta\lambda_{\text{spec}}/N$ , with  $\Delta\lambda_{\text{spec}}$  being the full spectral width covered by the spectrometer, and  $N$  the number of elements (pixel) of the line detector.  $\delta\lambda$  defines the maximum achievable depth range. A larger optical bandwidth results in reduced spectrometer resolution and thus in smaller depth range. In principle one could use a detector with higher pixel number but this has severe implications on the optical design of the spectrometer to keep its diffraction limited performance. Also, the data volume to be dealt with increases with detector size and the data handling becomes more challenging.

The tendencies in OCT are manifold. Among them, higher speed, improved axial resolution, and increased probing depth can be enumerated as issues for further research. All these points are interrelated with the subject of the current Part II. An overview of the mutual dependencies can be listed in a small house of quality and is given in the following table:

---

\* This chapter was partly published in the following peer-reviewed article:

A. H. Bachmann, R. A. Leitgeb, and T. Lasser, „Heterodyne Fourier domain optical coherence tomography for full range probing with high axial resolution,“ *Opt. Express* **14**, 1487-1496 (2006).

Goal	Mutual impact		
	Increase speed	Improve axial resolution	Achieve decent probing depth
Increase speed = Smaller detector	-	<i>No negative impact in FDOCT</i>	⇒ Less probing depth
Improve axial resolution = Increase spectral bandwidth	⇒ Increased detector size needed (more pixel) ⇒ Slower	-	⇒ Smaller probing depth or increased detector size needed
Achieve decent probing depth = Decent detector size	⇒ Slower if increased detector size	⇒ Increased detector size for keeping same axial resolution	-

**Table II-1. Mutual (negative) impact of three important OCT parameters.**

Considering Table II-1, one clearly sees that high speed, high axial resolution, and decent probing depth have a strong mutual interdependency. Probing depths of in general  $1\text{mm}$  and more are in most cases required. Sensitivity decay with increased relative distance from the zero delay (caused mainly by the modulation transfer function of the detection system and finite coherence length of one spectral channel) is a strong motivation to place the structure (biological or technical) as close to the zero delay as possible. However, axial displacement of the sample (*e.g.* slight movement of the proband head in ophthalmology) or intrinsic structural depth variations very often cause the structure to pass over the zero delay and generate so-called mirror terms (see Figure II-1).

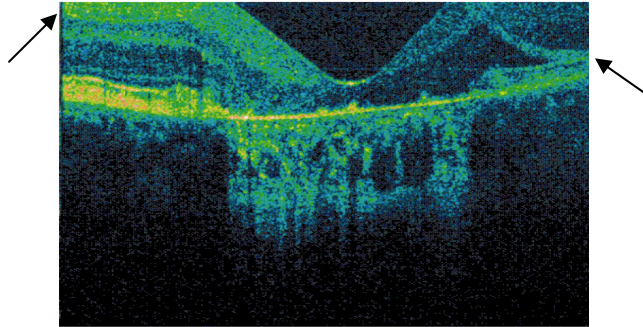


**Figure II-1. Retinal tomogram with strong mirror terms, indicated with arrows**  
[Courtesy: R.A. Leitgeb *et al.*, Medical University of Vienna].

For these reasons a long probing depth, even considerably longer than the penetration depth into the tissue for biological samples, is desirable. Besides increasing the number of detector pixels, an efficient way for increasing the depth range is achieved by generating the full complex signal [1]. The Fourier transform of the real valued spectrum yields redundant information for positive and negative frequencies corresponding to positive and negative path length differences between sample and reference. As a result one needs to adjust the reference arm delay so that it is slightly shorter than the relative distance of the first sample interface. In this case the axial structure does not mix with its mirrored counterpart in the adjoint Fourier half space. Hence only half of the Fourier space can be used for the sample structure.

The reconstruction of the full complex signal resolves this ambiguity and the signal space is doubled [2]. This needs at least two phase-shifted copies of the cross correlation between sample and reference signal. The phase shift is commonly realized by changing the path length of the reference arm using for example a mirror mounted on a piezo actuator.

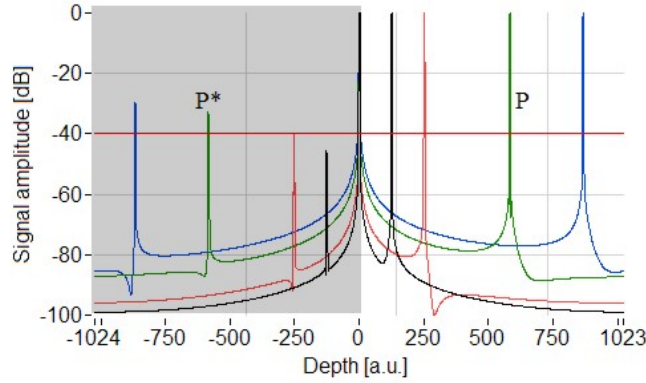


**Figure II-2. Simulation of complex FDOCT signal reconstruction with chromatic phase shifting (with no other phase errors present). Mirror terms in the left half ( $P^*$ , grey shaded area) are not totally suppressed. The signals are normalized to the true signal peak amplitudes ( $P$ ) in the right half space. The ratio between  $P^*$  and  $P$  indicates the mirror term suppression. The simulation supposes a Gaussian spectral distribution with a spectral width (FWHM) of 20nm (black), 40nm (red), 90nm (green) and 130nm (blue) respectively. The central wavelengths are 800nm for all cases.**

Shifting the reference optical delay  $\Delta z$  results in general in a chromatic phase error since the effective phase shift  $\Delta\phi$  is wavelength-dependent, *i.e.*  $\Delta\phi(\lambda) = 4\pi\Delta z/\lambda$ . First complex FDOCT systems used five phase-shifted signals and employed five-frame phase retrieval algorithms known from white light interferometry [1-4]. They have the advantage of being quasi achromatic and correct for the intrinsic phase error. Nevertheless they are only of limited use for *in-vivo* imaging since motion artifacts introduce stochastic phase errors that can only be handled by elaborate post processing algorithms [4]. Recently, an alternative approach has been used where phase-shifted spectra are recorded simultaneously on different lines of an area detector [5]. However the need for an area detector reduces the speed performance of the technique and the light efficiency is critical. Again five phase-shifted spectral interference patterns have been selected to reconstruct the sample signal.

For small optical bandwidths, using reference phase shifting, it is sufficient to record only two spectra shifted by  $\pi/2$  [6]. A fast and precise way of producing such phase-shifted spectra has been demonstrated recently with an electro-optic modulator [7]. Nevertheless, if the chromatic phase error increases, the mirror terms in the adjoint Fourier space will no longer be suppressed and the complex reconstruction fails. Figure II-2 shows a simulated complex FDOCT signal reconstruction based on the above mentioned two-frame algorithm for four different optical bandwidths (at 800nm central wavelength), keeping always the same ratio between spectral width of the detected spectrum and that of the spectrometer. The situation corresponds to the interference between signals from two mirrors placed in the sample and reference arm. Figure II-3 shows the height ratio of the two adjoint peaks in both Fourier half spaces,  $P$  and  $P^*$ , depending on the optical bandwidth. Assuming a typical dynamic range in an OCT tomogram of up to 40dB, we observe that the mirror terms are sufficiently suppressed for standard resolution complex FDOCT. However, for high resolution systems, with bandwidths above 40nm (for a Gaussian spectrum), the mirror terms reappear. One should note that this model does not account for scanning effects, phase noise or other disturbing

effects altering complex signal reconstruction. It is a pure chromatic effect. In Chapter 6 phase stability issues will be addressed in more detail.

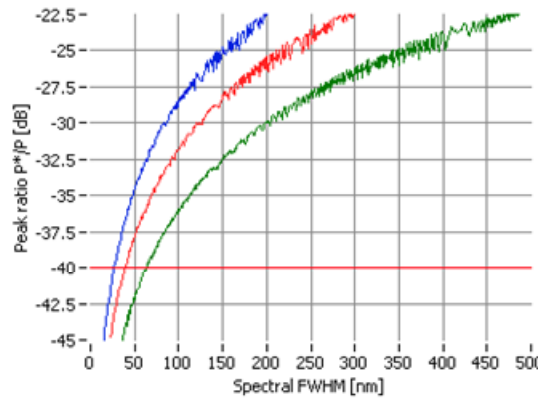


**Figure II-3.** The three plotted curves show the suppression ratio of  $P^*$  (mirror term) with respect to  $P$  (signal peak) for three different central wavelengths of the light source depending on optical bandwidth ( $\lambda_0=550\text{nm}$  (blue),  $\lambda_0=800\text{nm}$  (red),  $\lambda_0=1300\text{nm}$  (green)). Above  $-40\text{dB}$  mirror terms can become visible and the reconstruction algorithm fails. The “noisy” characteristics of the curves at larger bandwidths are due to leakage after discrete FFT. Again, no other than chromatic phase errors are present.

A different complex two frame approach is based on the use of a 3x3 fiber coupler that allows simultaneous quadrature detection [8]. Despite its elegance there are some difficulties in particular with broad optical bandwidths concerning the fact that two individual but phase matched spectrometers are needed and that the actual splitting ratio of fiber couplers is wavelength dependent.

In this part of the thesis we will introduce a new concept with true achromatic complex FDOCT signal reconstruction by employing frequency shifting devices in order to create a beating signal with a wavelength-independent frequency on the spectrometer detector. For swept-source FDOCT, similar concepts have been published recently [9, 10].

### 3.2 Theory

The most common way of introducing frequency shifts is by means of acousto-optic frequency shifters (AOFS). There, an ultrasonic wave is launched into an acoustic-wave-supporting material of usually high refractive index by means of a piezoelectric transducer. This acoustic wave alters the light frequency resulting in a constant and wavelength independent frequency shift of the original electromagnetic light field.

By employing two AOFS in the reference and sample path of an interferometer respectively, the frequency shifted light fields are  $E_R(\omega'_R, t, k) = \sqrt{I_R(k)} e^{j(k z_R - (\omega_0 + \omega_R)t)}$  and  $E_S(\omega'_S, t, k) = \sum_i \sqrt{I_{S,i}(k)} e^{j(k z_{i,R} - (\omega_0 + \omega_S)t)}$  with  $\omega'_{R,S} = \omega_0 + \omega_{R,S}$  being the frequencies of the

reference and the sample light fields after respective frequency shifting.  $\omega_0$  is the frequency of the original light field and  $\omega_{R,S}$  are the frequencies of the respective AOFS in the reference and sample path respectively.  $z_{i,R}$  denote the reference and sample interface positions. The summation runs over all sample interfaces with  $I_{S,i}(k)$  being the respective spectral intensities of the backscattered light fields and  $I_R(k)$  the reference field intensity as functions of wavenumber  $k$ . The interference field at the detector can then be written as

$$I(k) = I_R(k) + I_S(k) + \sum_{i,j;i \neq j} E_{S,i}(k) E_{S,j}^*(k) + \sum_i E_R(k) E_{S,i}^*(k) + c.c., \quad (\text{II.1})$$

where  $I_{R,S}(k)$  denote the reference and the total sample light intensities in the  $k$ -space with  $E_R(k)$  and  $E_{S,i}(k)$  as the reference and individual sample interface light fields and the asterix denoting their complex conjugates ( $c.c.$ ). The first two terms on the rhs of Equation (II.1) are DC terms, the second part together with its  $c.c.$  are autocorrelation terms due to interference of light fields from different sample interfaces. Only the last term and its  $c.c.$  known as cross-correlation terms contain the actual sample structure. By inserting the above described light field expressions into Equation (II.1), one observes that only the cross-correlation term containing the sample structure is modulated by a beating frequency  $\Omega = |\omega'_R - \omega'_S| = |\omega_R - \omega_S|$ . Denoting this term with its  $c.c.$  by  $I_{AC}$  we can write

$$I_{AC}(k, t) = 2 \sum_i \sqrt{I_R(k) I_{S,i}(k)} \cos(\Omega t - \Psi_i), \quad (\text{II.2})$$

with  $\Psi_i$  containing all time-independent phase terms. Note that the frequency shifting gives rise to a wavelength independent phase term  $\Omega t$  that governs the time dependence of the signal. If this signal is integrated over a certain time period, the modulation amplitude is reduced [11] and the recorded interference signal becomes

$$I_{AC,int}(k, t) = 2 \sum_i \sqrt{I_R(k) I_{S,i}(k)} \cos(\Omega t - \Psi_i) \text{sinc}\left(\frac{\tau \Omega}{2\pi}\right), \quad (\text{II.3})$$

where  $\tau$  is the integration or exposure time and with the definition  $\text{sinc}(x) \equiv \sin(\pi x)/(\pi x)$ . This attenuation term depends on the ratio between integration time and beating period.

### 3.2.1 Complex FDOCT signal

The complex signal can finally be constructed if two spectral interference patterns with a  $\pi/2$  phase difference are recorded. This is achieved by synchronizing the array detector with the beating frequency and by recording four spectra within one beating period. Hence successive spectra exhibit a phase difference of  $\pi/2$ . The complex signal becomes therefore [6]

$$\tilde{I}(k) = I(k, t_0) - jI\left(k, t_0 + \frac{\pi/2}{\Omega}\right), \quad (\text{II.4})$$

at arbitrary time instant  $t_0$ . The important difference to previous complex FDOCT approaches is that according to Equation (II.2) the phase difference between the two spectra is truly wavelength independent. Hence even large bandwidth sources can be employed without suffering from chromatic errors.

Since the signal phase changes continuously during detector exposure the signal intensity will be reduced according to Equation (II.3). Nevertheless, the exposure time will always be smaller than a quarter of the beating period ( $\tau < \Omega/4$ ) and therefore the attenuation cannot exceed  $-4\text{dB}$ . The above signal reconstruction resolves the complex ambiguity after performing the Fourier transform and leads therefore to a doubled depth range with respect to standard FDOCT [6]. Another important advantage results for the sensitivity of FDOCT. Due to the finite pixel size of the detector the modulation transfer function of the spectrometer decreases with increasing spectral modulation frequency, *i.e.*, with increasing path length difference between sample and reference [12]. Hence the sensitivity is best close to the DC

value. With a complex signal the structure can be placed across the DC line without being disturbed by its adjoint mirror terms.

It should be mentioned that with signal reconstruction based on Equation (II.4) neither the DC nor autocorrelation terms will vanish after performing the Fourier transform. However, autocorrelation terms are rather small in biological samples and the DC term can be strongly reduced by subtracting for example the separately recorded spectrum of the reference arm signal from each recorded spectrum before Fourier transform. An alternative way is to calculate a reference spectrum by averaging the recorded spectral interference patterns over a whole tomogram in post processing. In other approaches the complex conjugate of the signal in Equation (II.4) is taken and the difference of the absolute values after the Fourier transform is calculated [6]. Such differential methods become critical especially if the structure strongly overlaps with its mirror image [7].

### 3.2.2 Differential complex reconstruction

Equation (II.4) is a two-frame method where two recorded interference patterns with a phase difference of  $\pi/2$  constitute the complex signal. By subtracting two such complex signals with a relative time delay of half a beating period the parasitic DC and autocorrelation terms will efficiently be removed (see Figure II-4). This is due to the fact that these terms appear as static signals across the detector since their phase is independent of the beating frequency. As a result they will be eliminated already on the spectral level whereas the actual signal will be enhanced:

$$\begin{aligned}\tilde{I}_{2x2}(k) &= \tilde{I}(k, t_0) - \tilde{I}\left(k, t_0 + \frac{\pi}{\Omega}\right) = \\ &= \left[ I_{AC}(k, t_0) - I_{AC}\left(k, t_0 + \frac{\pi}{\Omega}\right) \right] - j \left[ I_{AC}\left(k, t_0 + \frac{\pi/2}{\Omega}\right) - I_{AC}\left(k, t_0 + \frac{3\pi/2}{\Omega}\right) \right] = \quad (\text{II.5}) \\ &= 2 \left( I_{AC}(k, t_0) - j I_{AC}\left(k, t_0 + \frac{\pi/2}{\Omega}\right) \right).\end{aligned}$$

After Fourier transform of Equation (II.5) the pure structure terms result. Theoretically a signal enhancement of +3dB is obtained which counterbalances approximately the -4dB signal loss mentioned in the previous section.

It is important to notice that the elimination of parasitic terms is insensitive to the exact phase difference of  $\pi$  between the two complex signals. Nevertheless the exact phase relation of  $\pi/2$  is important for the respective two frames that constitute the complex signal.



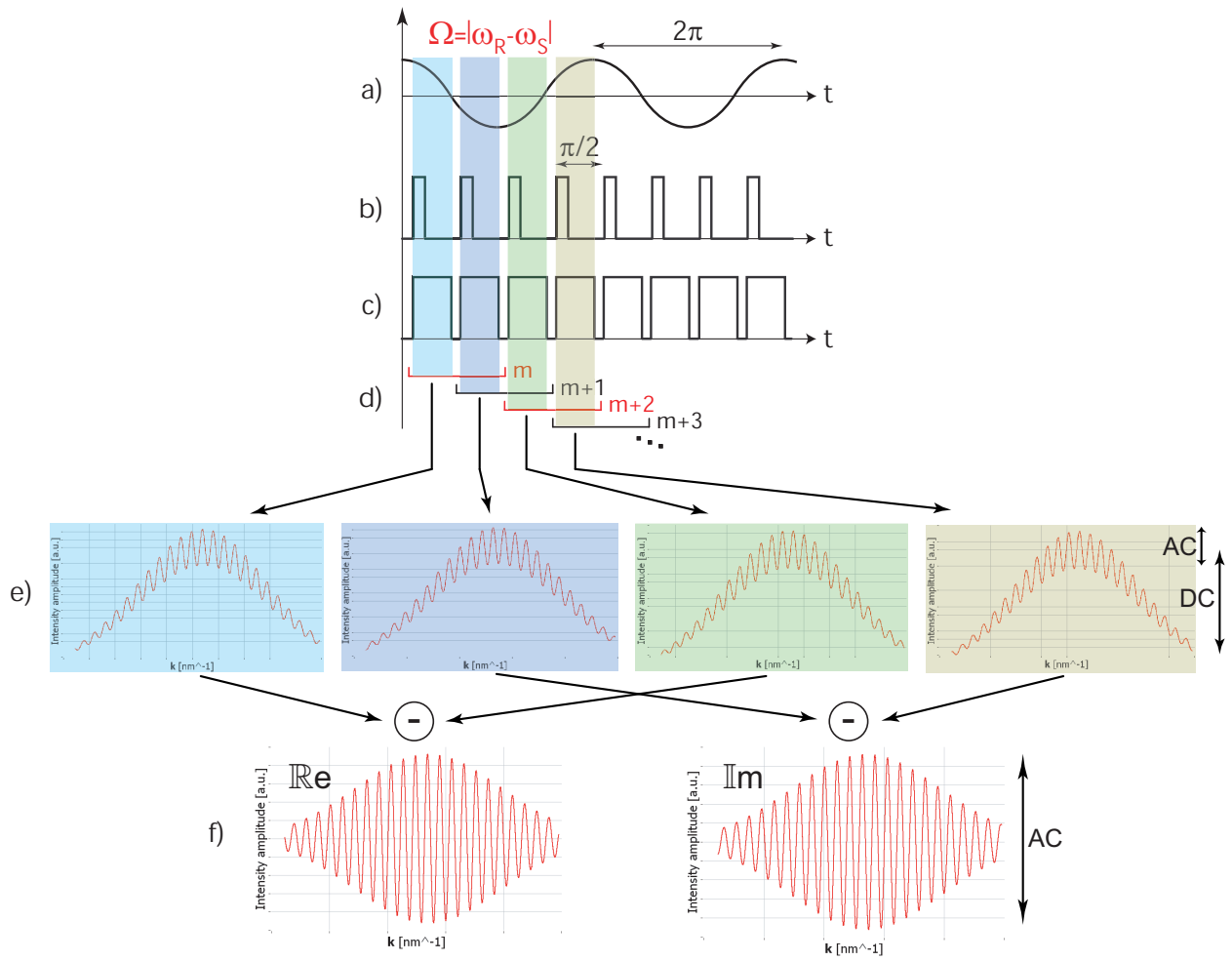


**Figure II-4. Differential complex reconstruction.** (a) beating signal; (b) camera trigger; (c) camera exposure; (d) brackets indicate the frames used for complex two-frame reconstruction; different colors indicate frames used for differential complex technique. (e,f) 1<sup>st</sup> and 3<sup>rd</sup> spectrum combined result in the real part (bottom left) while 2<sup>nd</sup> and 4<sup>th</sup> spectrum combined result in the imaginary part of the complex AC value (bottom right).

### 3.3 Experimental

#### 3.3.1 Setup

A Mach-Zehnder like interferometer setup as shown in Figure II-6 was built. The source was a mode-locked fs-Ti:Sapphire (fs-Ti:S) laser (Femtolasers Inc.) with a central wavelength at  $\lambda_0 = 800\text{nm}$  and a spectral full width at half maximum (FWHM) of  $\Delta\lambda_{\text{FWHM}} = 130\text{nm}$ . The light was split via a 90:10 fiber coupler into the sample and reference arm respectively. The two pigtailed AOFS<sub>1,2</sub> (Brimrose Inc.) operated at 100 and 100.005MHz ( $\omega_R = 2\pi \cdot 100.005\text{MHz} \pm 0.1\text{Hz}$  and  $\omega_S = 2\pi \cdot 100\text{MHz} \pm 0.1\text{Hz}$ ). They generated a beating signal at the detector of the spectrometer at 5kHz.

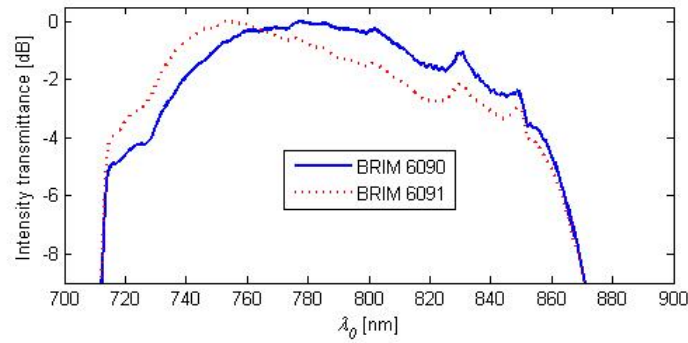


**Figure II-5. Logarithmic spectral characteristics of the two pigtailed AOFS. The -3dB spectral transmittance is approximately 120nm.**

The spectral transmittance of the two AOFS was characterized by its -3dB width  $\Delta\lambda_{-3dB} \approx 120nm$  (see Figure II-5). The translation stage (TS) in the reference arm was used for adjusting the relative delay to the sample. In order to exploit the full depth range, the zero-delay was matched to the focal plane of the imaging optics. The dispersion mismatch between both arms was compensated by using BK7 wedges (Disp). The scanning unit (Cambridge Technology) allowed for a 2D scanning of the sample. For imaging an achromatic lens with a focal distance of 60mm was chosen resulting in a theoretical lateral resolution of  $23.2\mu m$  and a depth of focus of 1.05mm. The transverse scanning speed across the sample was 30mm/s and the average illumination power 4.5mW. The array detector of the spectrometer was a 12bit line scan CCD with 2048 pixels (ATMEL AVIIVA), working at 20kHz and with an integration time of 30μs per acquisition. According to Equation (II.3) the interference modulation amplitude was attenuated by -1.3dB. The detector trigger (Figure II-6(b)) was synchronized with the beating frequency (Figure II-6(a)) such that four equally delayed images within the full period of the beating signal were recorded (Figure II-6(c)). Since the phase changes continuously there was a constant  $\pi/2$  phase shift between successive frames. Hence ‘moving’ two-frame reconstruction according to Equation (II.4) was used as shown in Figure II-6(d). For the differential complex reconstruction four successive frames were used. However, the block of four frames constituting the next complex “A-scan” overlaps by three frames with the previous block such that again a moving signal reconstruction is realized (Figure II-6(d)). As a result the actual number of complex “A-scans” per tomogram is equal to the number of recorded spectra minus three, which can be neglected. The spectrometer was equipped with a transmission diffraction grating of 1200lines/mm. The camera lens (CL) was a 135mm objective. The full spectral width covered by the spectrometer was  $\Delta\lambda_{Spec} = 156nm$ . The actual FWHM of the spectrum at the detector was 90nm resulting in an axial resolution of  $4\mu m$  in air. The measured sensitivity close to the zero delay was 111dB and decayed by -15dB as one approached the maximal depth position.

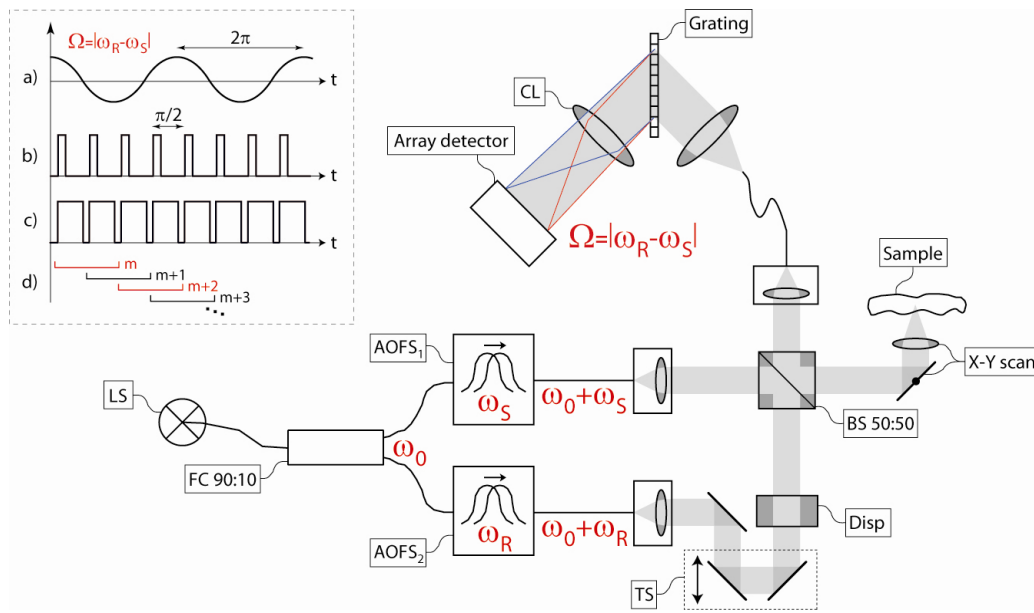


**Figure II-6. Mach-Zehnder like interferometer comprising: fs-Ti:S light source (LS), 90:10 fiber coupler (FC), AOFS shifting the light fields by  $\omega_{R,S}$ , translation stage (TS), dispersion compensation (Disp), 50:50 beamsplitter (BS), galvo scanners (X-Y scan), camera lens (CL). Box in top left corner shows: (a) beating signal; (b) camera trigger; (c) camera exposure; (d) brackets indicate the frames used for complex two-frame reconstruction; different colors indicate frames used for differential complex technique.**

### 3.3.2 Detailed synchronization scheme

Phase accuracy and long time relative frequency stability is important for phase-locked FDOCT. A convenient way for achieving such stability and keeping a very high flexibility is the use of individual electronics devices being connected to one and the same timebase (see Figure II-7). The resulting beating frequency is in the order of  $kHz$  and phase accuracy of the system (without scanning effects etc.) is desired to be better than  $\lambda/1000$ . Such performance is achieved and experimentally verified with this approach (see also §6.2). The relative frequency stability of the frequency generators was observed with a universal counter, connected to the same timebase.

Since FDOCT still needs one or two dimensional scanning for 3D image acquisition, scanners have to be driven with a certain scanning pattern (typically X: fast sawtooth, Y: slow sawtooth) and the frame grabber has to be synchronized with respect to the line acquisition and the performed scan. Again, this is very conveniently achieved with individual, commercially available devices. Function generators were used with the voltage output driving the scanning pattern and their synchronization output serving as logic signal for triggering the data recording via the frame grabber board (see Figure II-7).

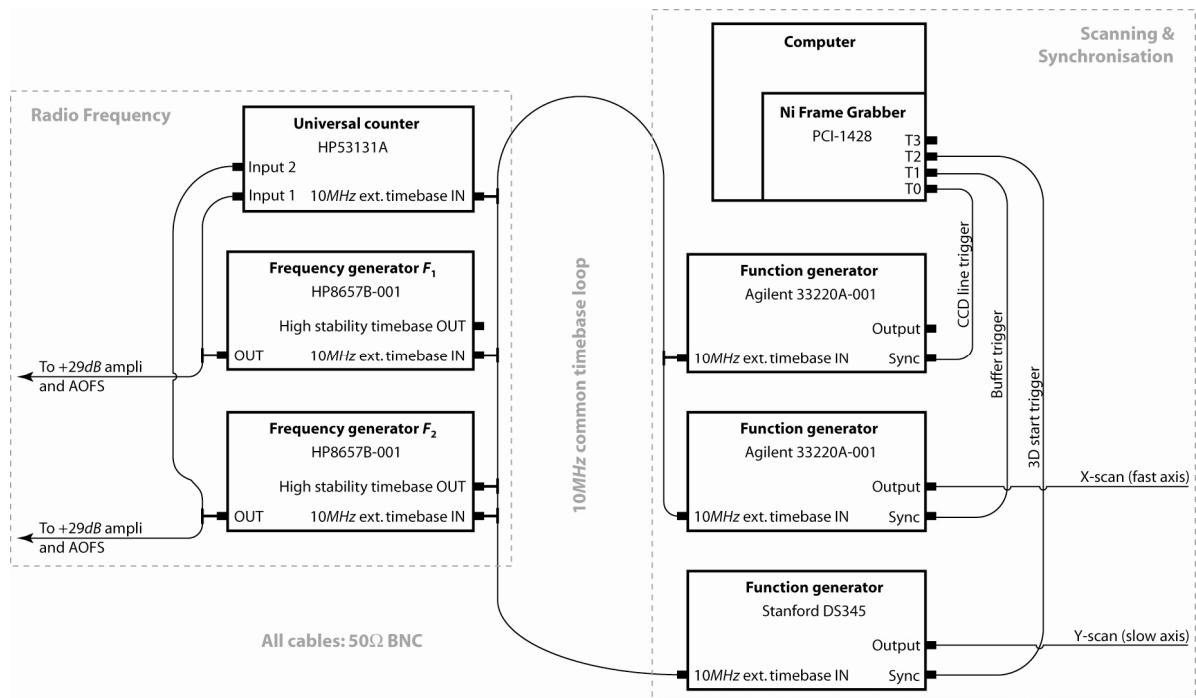
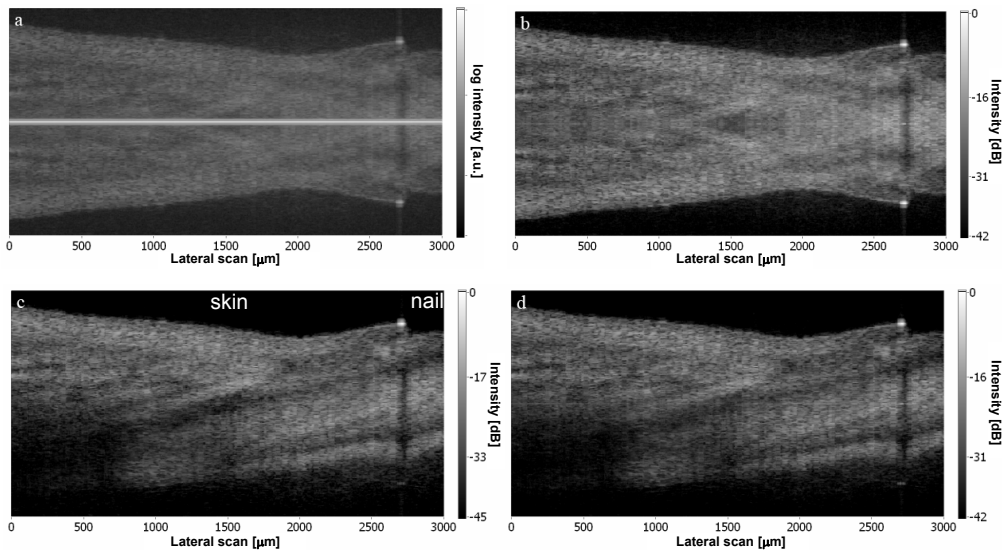


**Figure II-7. Synchronization scheme for heterodyne FDOCT. A common timebase is very important for relative frequency accuracy and long time stability. A very convenient synchronization for line/buffer acquisition and scanning is using individual function generators with external 10MHz timebase input.**

### 3.4 Results and discussion

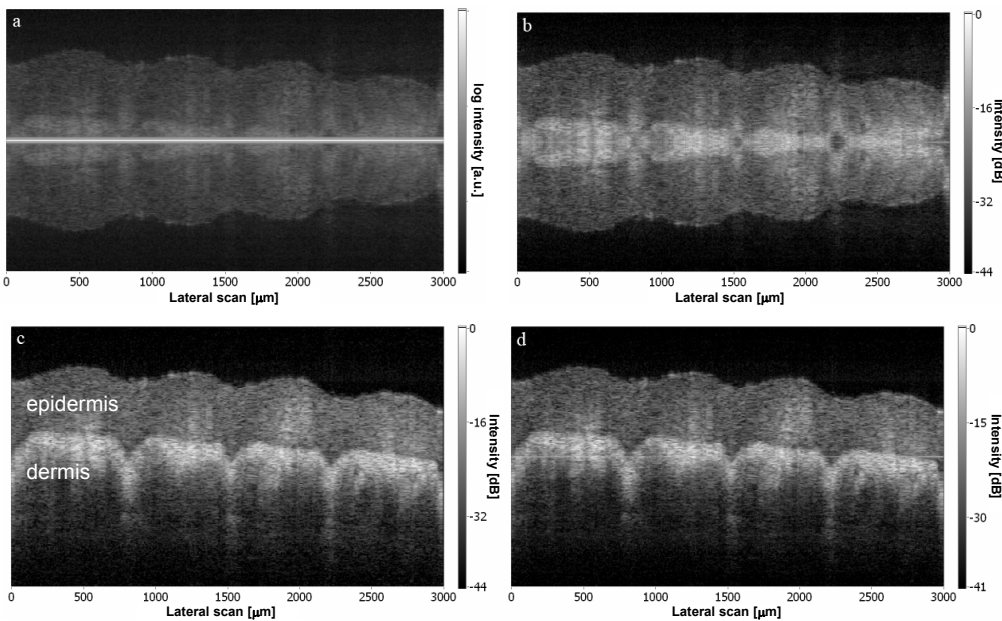
In order to test the heterodyne FDOCT setup *in-vivo* measurements on human skin were performed. Figure II-8 and Figure II-9 show tomograms with 2'000 “A-scans” and a lateral extension of 3mm. The acquisition time for a full tomogram was 100ms. The scanning was performed at continuous speed with a 15x over-sampling with respect to the theoretical lateral resolution.

Figure II-8 and Figure II-9 show the respective reconstructed sample structures of the nailfold region and of skin at the finger tip of an adult. The reference arm was adjusted such that the zero delay corresponded to a place within the structures. Figure II-8(a) and Figure II-9(a) show resulting tomograms using standard FDOCT without any DC correction, whereas for Figure II-8(b) and Figure II-9(b) a DC subtraction is applied in post processing (see §3.2.1). Standard FDOCT means that the recorded interference patterns that constitute a tomogram are first re-sampled to compensate for the spectrometer dispersion and to change from wavelength to wavenumber coordinate, and afterwards are Fourier transformed using FFT [13]. As a result of the complex ambiguity the structure is completely deteriorated by the overlapping mirror terms.



**Figure II-8.** (a) Tomogram of a fingernail fold region with standard FDOCT and no DC correction. The zero-delay is clearly visible due to the strong DC signal (bright line in the center). (b) As (a) but with calculated DC correction. (c) As (a) but reconstruction of complex signal according to differential complex method (see Equation (II.5)) described in §3.2.2. (d) As (a) but reconstruction of complex signal according to Equation (II.4) in §3.2.1 with a calculated DC correction. All tomograms are based on the same dataset. The tomogram depth shown is  $1.75\text{mm}$  (in air).

Figure II-8(d) and Figure II-9(d) show the reconstruction of the tomogram using the two-frame method described by Equation (II.4) in §3.2.1 with a DC correction. As one can see the structure is correctly reconstructed and the mirror terms are suppressed. Still, part of the DC term remains slightly visible but the influence on the image quality is negligible. Figure II-8(c) and Figure II-9(c) show the reconstruction of the tomogram using the differential complex algorithm described by Equation (II.5) in §3.2.2. As for the two-frame reconstruction the structure is correctly displayed (mirror term suppression approx.  $-30\text{dB}$ ) and the DC line is completely suppressed. The dynamic range of the tomograms lies around  $40\text{dB}$ .



**Figure II-9.** (a)-(d) Same remarks as for Figure II-8. *In-vivo* object was a fingertip of an adult and the tomogram depth shown is  $1.95\text{mm}$  (in air).

The fact that no reference spectrum must be recorded or calculated in post processing to suppress the DC component is an advantage of the differential complex reconstruction method. Moreover not only the DC part but also autocorrelation terms are suppressed and the dynamic range is improved by up to  $+3dB$  with respect to the two-frame complex reconstruction. Currently we are employing transverse over sampling in order to keep defined phase relation between consecutive spectra. As already mentioned in §3.2.2 the differential complex algorithm is relatively stable against phase errors. Nevertheless it is expected that with considerably lower transverse sampling the gain in dynamic range decreases and the suppression of the DC and autocorrelation terms will be less efficient [14].

In §3.3 we pointed out that the sensitivity of FDOCT is highest close to the zero delay. By placing the object across the zero delay one has a clear advantage in sensitivity as compared to concepts where only half of the Fourier space is available. Especially for *in-vivo* applications structure movements are difficult to handle. For standard FDOCT enough distance to the zero delay needs to be kept in order to avoid overlapping with the mirror image. Thus, one sacrifices part of the high sensitivity of FDOCT and effective depth range. The tomograms in Figure II-8(c,d) and Figure II-9(c,d) demonstrate the sensitivity advantage for structures that cross the zero delay. Even for a central wavelength of  $800nm$  it is possible to visualize dermal structures as shown in Figure II-9(c,d) with sufficient penetration depth.

The main limitation of the above presented experimental realization is the fiberized AOFS with a  $-3dB$  transmittance bandwidth of only  $120nm$  as the axial resolving power of the system is reduced by approximately 40%.

### 3.5 Conclusion

In this chapter, spectrometer-based heterodyne FDOCT was presented and discussed. *In-vivo* measurements showed experimentally the suppression of artifacts like mirror terms due to full complex signal reconstruction by quadrature detection of a stable beating frequency at 20'000 depth-scans per second. The beating frequency is generated by two AOFS and is wavelength-independent; therefore no mirror terms interfere with the actual structure terms even if large bandwidth sources are employed. A novel differential complex reconstruction algorithm is proposed and experimentally verified that allows efficient elimination of DC and autocorrelation terms and shows a sensitivity advantage of approximately  $+3dB$  with respect to a complex two-frame algorithm. The present achromatic, heterodyne spectrometer-based FDOCT systems would exploit its full potential when combined with a true heterodyne detector that performs the signal demodulation for each pixel on-chip instead of an integrated bucket approach as in our case. In this case a decently higher modulation frequency than the one we employed should be used in order to limit adverse effects caused by phase and amplitude errors issuing from scanning.

## Chapter 4

### Broadband fiberized acousto-optic frequency shifter

#### 4.1 Introduction

In the previous chapter we have seen that available acousto-optic frequency shifters (AOFS) are the limiting factor for achieving ultra-high resolution tomograms based on the presented heterodyne FDOCT method. Especially fiberized AOFS have a rather limited spectral bandwidth. As we will show in detail throughout the following paragraphs, these limitations are strongly related to the diffractive nature of these AOFS. Since the high axial resolution is one of the key motivations for this OCT project, the necessity of broadband devices becomes an important issue. The main goals for the design therefore are: increased bandwidth, flat spectral response and high fiber coupling efficiency.

Some effort concerning bandwidth issues of AOFS related to OCT was done by Chen *et al.* [15, 16]. However, it is neither a fiberized solution nor an approach where both interferometer arms are equilibrated with respect to their dispersive behavior by placing one frequency shifter into each arm. In [15] dispersion of latter devices is compensated in the sample arm by introducing an extra length of single mode fiber and dispersion compensation up to the third order is reported. Fiberized AOFS were already used in OCT, but rather in previous time domain solutions [17] or swept-source FDOCT [9, 10], where the devices presented in the following paragraphs would perfectly well be suited for. In the case of swept-source FDOCT, where very high modulation frequencies for heterodyne detection are required, a single AOFS with high spectral bandwidth would even be necessary since no second device can partly compensate diffraction by placing it right behind the first one. In latter case the second frequency shifter is driven in the down-shifted mode [15, 18], simplifying beam control due to improved co-linearity behind the second device. However, dispersion compensation will be more challenging since the interferometer will not be compensated as if one AOFS is placed in each interferometer arm.

#### 4.2 Theory

##### 4.2.1 Principe of acousto-optics

Acousto-optic interaction describes the interference of (in approximation) two plane waves: an electromagnetic and acoustic wave. This interaction happens within a – for the considered spectral range – transparent medium. The acoustic wave induces periodic variations of the refractive index due to a photoelastic effect. The material compression increases refractive index, whereas rarefaction will have a decreased refractive index. Thus, a dynamic medium

with gradual and periodic variations in refractive index is induced by the acoustic wave propagation [19-23].

In the case of a harmonic acoustic wave with frequency  $F$  (throughout the rest of this chapter capital letters are acoustic variables) and the wavenumber  $K=2\pi/\Lambda$  propagating in the  $x$ -direction with  $\Lambda$  being the acoustic wavelength, the varying refractive index  $n$ , caused by the acoustic wave, can be written as [19, 21-23]

$$n(x,t) = n_0 + \Delta n \sin(2\pi Ft - Kx), \quad (\text{II.6})$$

where  $n_0$  is the refractive index of the medium without acoustic perturbation and  $\Delta n$  the maximum variation amplitude caused by the acoustic wave. As a result a sinusoidal grating with period  $\Lambda=V/F$  is generated, propagating as a “plane” wave at the acoustic speed  $V$  within the medium. Therefore, an optical wave interacting with its acoustic counterpart can be diffracted. As  $V$  is much smaller than the speed of light, the acoustic wave can be considered as quasi-stationary with a fixed grating with respect to the optical beam. Its lateral displacement will only induce a frequency shift due to Doppler effect.

#### 4.2.2 Acousto-optical diffraction regimes

In order to characterize the diffraction regime a quality factor  $Q$  is introduced, called Klein-Cook parameter [21-23]:

$$Q = \frac{LK^2}{k_{0,m}} = \frac{2\pi\lambda_0 L}{n\Lambda^2}, \quad (\text{II.7})$$

where  $\lambda_0$  is the wavelength in vacuum,  $k_{0,m}$  its wavenumber in the medium,  $L$  the interaction length between optical and acoustic wave, and  $n$  the refractive index of the crystal.

Analytic solutions to the problem of acousto-optic diffraction are given for the two cases where

- $Q \ll 1$  Raman-Nath regime
- $Q \gg 1$  Bragg regime

The Raman-Nath regime (see Figure II-10(a)) presents multiple diffraction orders and corresponds to a thin phase grating. It is used for realizing *mode lockers* and *Q-switches* in lasers [20, 23]. For our design goal the more interesting case is the Bragg regime where  $Q \gg 1$  (see Figure II-10(b)).

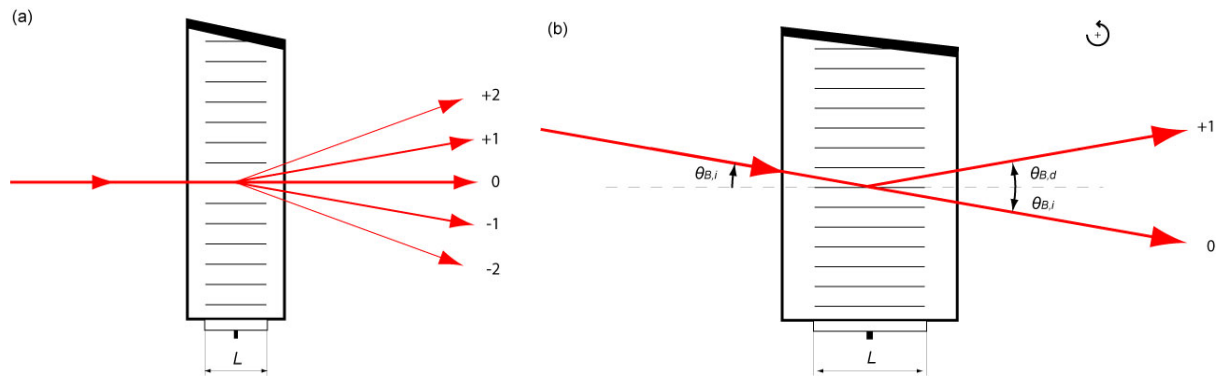


**Figure II-10. (a) Raman-Nath regime with multiple diffraction orders. (b) Bragg regime, crystal illuminated under the Bragg angle  $\theta_B$ .**



In the Bragg regime the interaction length  $L$  and the acoustic frequency  $F$  are higher than in the Raman-Nath regime. In this case the acousto-optic interaction acts like a thick phase grating, ideally producing only two diffraction orders (-1 and 0 or +1 and 0) [20-22]. However, the Bragg condition has to be satisfied defining the incident angle of the optical beam within the medium to be [19-23]

$$\sin \theta_{B,m} = \frac{K}{2k_m} = \frac{\lambda}{2\Lambda} = \frac{\lambda_0}{2n\Lambda}, \quad (\text{II.8})$$

where the index  $m$  stands for the light propagating inside the medium. Accordingly  $\theta_{B,m}$  stands for the Bragg angle inside the medium.

A vector diagram shown in Figure II-11 depicts the situation where a monochromatic plane optical wave, with an incident angle satisfying the Bragg condition, interacts with a plane acoustic wave. Such diagram can be attributed to an Ewald sphere construction. One observes that the system is symmetric. Since  $F \ll \nu$  and dealing with an isotropic medium (or the polarization state is linear, propagating along the ordinary axis), with  $\nu$  being the optical frequency, the modulus of the incident and diffracted wavevectors are identical:  $|k_{d,m}| \approx |k_{i,m}|$ .

Thus we can write:  $|\theta_{d,m}| = |\theta_{i,m}| = |\theta_{B,m}|$ .

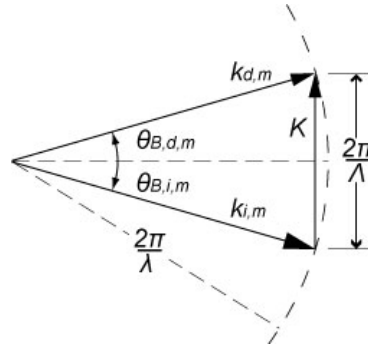


Figure II-11. Vector diagram (Ewald sphere construction) for the acousto-optic interaction resulting in a so-called *up-shift*.  $k_{i,m}$  and  $k_{d,m}$ : incident and diffracted optical wavevectors respectively.

From Ewald sphere construction follows that energy and momentum are conserved. The following relations result:

$$\begin{aligned} \vec{k}_{d,m} &= \vec{k}_{i,m} \pm \vec{K} \\ \omega_d &= \omega_i \pm \Omega_A \end{aligned}, \quad (\text{II.9})$$

where  $\Omega_A$  is the angular acoustic frequency increasing (*up-shift*) or decreasing (*down-shift*) the optical frequency due to the Doppler effect. Depending on the incident angle with respect to the acoustic wavevector we are either left with an *up-shift* or a *down-shift*. This change in frequency, which is the same for all wavelengths and thus achromatic, is the essence for the achromatic beating signal used previously already in our heterodyne FDOCT system.

#### 4.2.3 Diffraction efficiency under Bragg condition

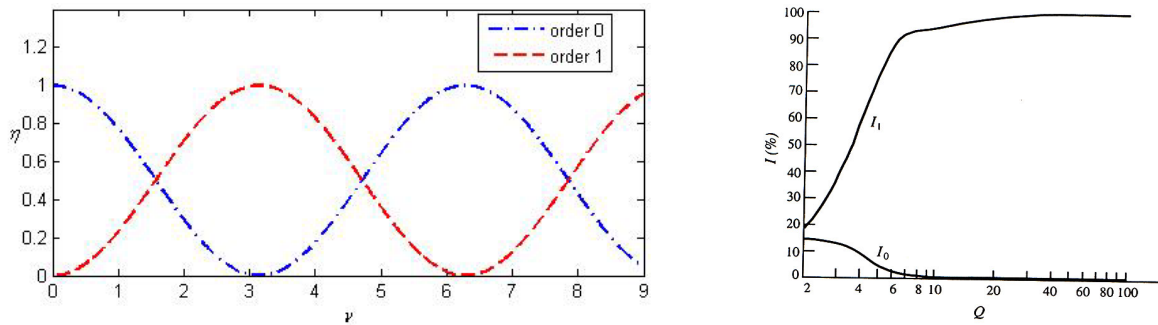
Coupled wave theory allows calculating diffraction efficiency  $\eta_1$  as a function of the Raman-Nath parameter  $\nu_{RN}$ , in the case of Bragg regime (see Figure II-12(lhs)) [21, 22]:

$$\begin{aligned}\eta_1 &= I_{+1,-1}/I_i = \sin^2\left(\frac{\nu_{RN}}{2}\right) \\ \eta_0 &= I_0/I_i = \cos^2\left(\frac{\nu_{RN}}{2}\right),\end{aligned}\quad (II.10)$$

with indices 0, +1, and -1 indicating the diffraction order and  $I_i$  being the incident beam intensity. The Raman-Nath parameter is defined as [21, 22]:

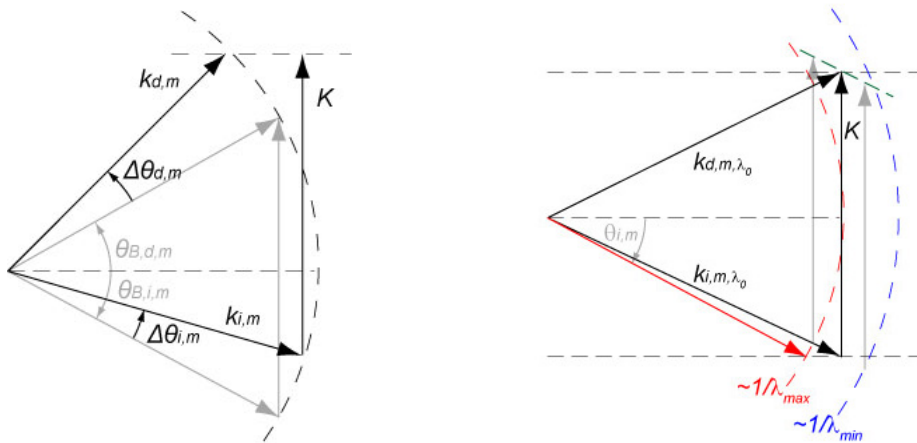
$$\nu_{RN} = \frac{2\pi}{\lambda_0} |\Delta n| L. \quad (II.11)$$

From Equation (II.10) one can conclude that all light intensity is distributed within these two orders. An acousto-optic frequency shifter is most efficient for the case where  $\nu_{RN} \equiv \pi$ .



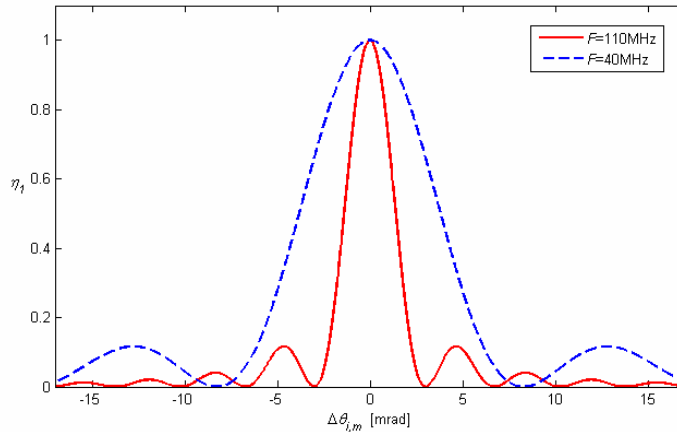
**Figure II-12. (lhs) Diffraction efficiency of order 0 and +1 or -1 as a function of  $\nu_{RN}$  in the case of Bragg regime. (rhs) Diffracted intensity  $I_1$  and intensity in order zero  $I_0$  for optimal interaction ( $\nu_{RN}=\pi$ ) as a function of the quality factor  $Q$  [22].**

Figure II-12(rhs) shows the diffraction efficiency as a function of the quality factor  $Q$  for optimal interaction ( $\nu_{RN} = \pi$ ) [22, 23]. As shown,  $Q$  should be at least above  $\sim 7$  in order to achieve high diffraction efficiencies, resulting in a necessary interaction length  $L$  being typically above 1cm (depending on the acoustic frequency and the material used).



**Figure II-13. (lhs) vector diagram for interaction not satisfying the Bragg condition. See text for details. (rhs) Ewald sphere construction with broad bandwidth. Diffraction ideally occurs between the two horizontal lines representing the deviation induced by the acoustic wavevector  $K$ . Therefore longer wavelengths (=shorter wavevectors, red arrow) should have an increased incident angle  $\theta_{i,m}$  for matching Bragg condition again.**

If the incident beam does not satisfying Bragg condition, decreased diffraction efficiency will result. This situation is illustrated in Figure II-13(lhs). For a non-monochromatic beam this will even be inevitable, since the Bragg condition is depending also on the optical wavelength. A convenient way for illustrating the condition of broad bandwidth is again the Ewald sphere construction Figure II-13(rhs). The circles indicate the wavelength range of the incident polychromatic light field. As can be seen quite easily in this construction, the incident polychromatic wave field violates the Bragg condition with growing bandwidth. Or as indicated by the red arrow can fulfill, if the incident wave angle is increased.



**Figure II-II-14. Normalized diffraction efficiency outside the Bragg condition for two different acoustic frequencies, with optimal interaction ( $v_{RN}=\pi$ ), interaction length  $L=11mm$  and acoustic speed  $V=4200m/s$ .  $\Delta\theta_{i,m}=0$  corresponds to the Bragg condition.**

Using coupled wave theory the following relation for the diffraction efficiency can be found [21-23]:

$$\eta_1 = \frac{I_{+1,-1}}{I_i} = \left( \frac{v_{RN}}{2} \right)^2 \text{sinc}^2 \sqrt{\left( \frac{v_{RN}}{2} \right)^2 + \left( \frac{K \Delta\theta_{i,m} L}{2} \right)^2}, \quad (\text{II.12})$$

where  $\Delta\theta_{i,m}$  is the difference between the Bragg angle and the effective incidence angle of the considered optical beam inside the medium. This result will be important for the modeling of a broadband device (see §4.3). Figure II-II-14 shows the normalized diffraction efficiency not satisfying the Bragg condition for two different acoustic frequencies.

Following conclusions arise:

- For the limiting case where  $\Delta\theta_{i,m}=0$  Equation (II.10) is found
- Lower frequencies seem to be less critical for broader spectra, since the error on the angle can be bigger. However, there is a square dependency of the quality factor  $Q$  as a function of acoustic frequency, which has an adverse effect on the Bragg regime and therefore requires longer interaction lengths.

Finally it should be noted that the deviation from the Bragg angle for the incident and the diffracted beam can be approximated as identical:  $\Delta\theta_{d,m} \approx \Delta\theta_{i,m}$ , still applying the approximation  $|k_{d,m}| \approx |k_{i,m}|$  and considering the approximation  $\sin(x) \approx x$ .

It is evident that all optical angles and wavenumbers described as being inside a medium (with the index  $m$ ) can be transformed to outside the medium (without index  $m$ ) by simply applying the law from Snell-Descartes  $n_1 \sin(\alpha_1) = n_2 \sin(\alpha_2)$ . Throughout the rest of this chapter optical angles and wavenumbers will be considered as being outside the medium.

#### 4.2.4 Anisotropic interaction

Interaction under Bragg condition as we have seen it until now is so-called *isotropic interaction*. One also talks about longitudinal interaction. In this case, the crystal is compressed longitudinally and the refractive index will be the same for the incident and diffracted light beam. It is a symmetric situation and no polarization change will be induced by the acousto-optic interaction. Latter case is especially produced for non-birefringent or appropriately manufactured and oriented birefringent crystals. Very often tellurium dioxide ( $\text{TeO}_2$ ) is used, a tetragonal crystal with birefringent behavior, transparent in the range of  $0.33\mu\text{m}$  to  $5\mu\text{m}$ . Longitudinal acoustic waves can be induced in the crystalline direction  $[001]$  at a speed of  $V=4200\text{m/s}$  or transverse waves (shearing) in the direction  $[110]$  at a much slower speed of  $617\text{m/s}$ .

Anisotropic interaction is much more complicated to be analyzed than its isotropic counterpart. In addition it is much less described by literature [20, 23]. Birefringent crystals, as it is the case for  $\text{TeO}_2$ , can induce anisotropic interaction. In such case, one can observe a change in polarization as it is explained by Figure II-15.

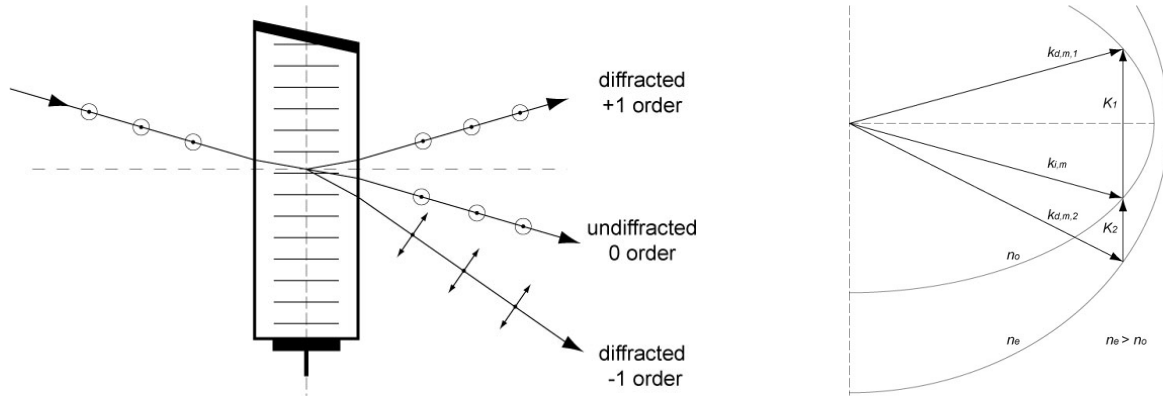


**Figure II-15. Anisotropic interaction. (lhs) An incident beam with TE polarization produces either an up-shifted or a down-shifted copy, depending on the applied acoustic frequency. (rhs) Iso-anisotropic mixing of diffraction orders [24]. For the acoustic wavevector  $K_1$  an isotropic interaction is caused. Incident and diffracted wavevectors both remain with the ordinary refractive index  $n_0$ . For  $K_2$ , however, anisotropic interaction happens and the optical wavevector is linked to the extraordinary refractive index  $n_e$  (change in polarization).**

For our purpose with a stable, highly efficient frequency shift without change in polarization we will try to remain to a maximum within the isotropic case. This defines some conditions to our acousto-optic frequency shifters:

- Incident light beam with linear polarization (in general TE mode)
- Stable acoustic frequency with as little harmonics as possible
- Collimated light beam and plane acoustic wave in order to have well-oriented wavenumbers (acoustic and optic)

If this is not the case, diffraction efficiency will drop and polarization-dependent effects might occur. For an interferometric system like OCT this can rapidly get annoying since coherent amplification amplifies even very parasitic signal.

### 4.2.5 Beam shaping and acoustic power

For completeness we mention briefly two additional points.

In §4.2.2 the vector diagram was shown; it is valid for plane waves. As a matter of fact, a convergent or divergent wave has a spectrum of wavenumbers with a certain spectral distribution. In such a situation the above simplified description would become much more complex. However, within the Rayleigh range of a beam the wave is pseudo-planar. Supposing a plane acoustic wave, the acousto-optic interaction length of a focused light beam would be of approximately the length of the Rayleigh range, resulting in decreased diffraction efficiency [23]. However, such a configuration is sometimes interesting, especially when very short transit times are needed (*i.e.* rapid switching in acousto-optic modulators or acousto-optic tunable filters), but is of much less importance for frequency shifters.

Another important parameter is the acoustic power  $P_A$  which must be induced into the crystal. It seems quite logic that some optimum might occur while increasing acoustic power. The important conclusion after some calculation leads to an expression for acousto-optic frequency shifters reading [21-23]:

$$\eta_1 = \sin^2 \left( \frac{\pi}{\lambda_0} \sqrt{\frac{M_2 L}{2H}} P_A \right), \quad (\text{II.13})$$

where  $M_2$  is the figure of merit often found in manufacturers data sheets and  $H$  the height of the acoustically active zone. This function has a maximum for its argument to be equal to  $\pi/2$ . In addition it is important to notice that the figure of merit  $M_2$  is proportional to  $n^6$ , explaining why mostly (in general birefringent) crystals rather than standard glasses are used for acousto-optic devices: For a given acousto-optical effect the acoustic power to be applied is considerably lower for materials with high refractive index.

## 4.3 Design of a broadband AOFS

### 4.3.1 Uncorrected case

In the previous paragraphs we have seen that high diffraction efficiency can be realized by satisfying the Bragg condition with respect to the angle of the incident beam. This Bragg angle, however, will be strongly dependent on the wavelength. Supposing Bragg regime and TE polarisation of the incident beam with a certain spectral width, and assuming Bragg condition to be satisfied with respect to the central wavelength, angular spreading of the spectrum, which is a dispersive effect, will occur as illustrated in Figure II-16. In addition to the spreading, diffraction efficiency will drop for wavelengths violating the Bragg condition.

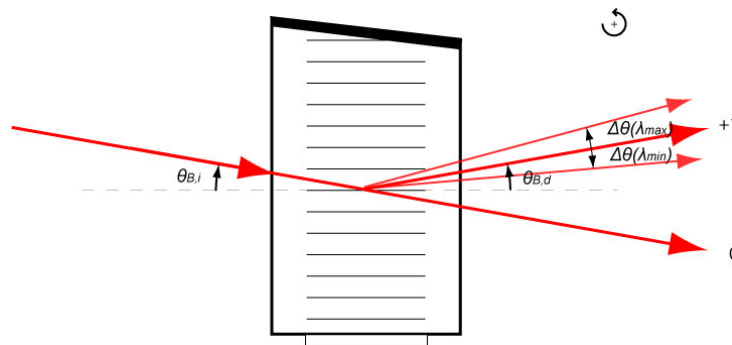


**Figure II-16. Wavelength dependent angular spreading of the diffracted beam. At the exit, wavevectors are not co-linear anymore.**

For an uncorrected case the angular error  $\Delta\theta(\lambda)$  is defined as the difference between Bragg angle of the central wavelength  $\lambda_0$  and the Bragg angle of the wavelength  $\lambda$  to be evaluated:

$$\Delta\theta(\lambda) = \theta_B(\lambda_0) - \theta_B(\lambda). \quad (\text{II.14})$$

In Figure II-17 Equation (II.14) is shown graphically for a spectral range of more than an octave, covering the visible (VIS) and near infrared range (NIR) covered approximately by a fs-Ti:S laser. The angles are given for outside the medium, taking into account the refraction at the crystal interfaces. Throughout the rest of this chapter all angular values will be in air.

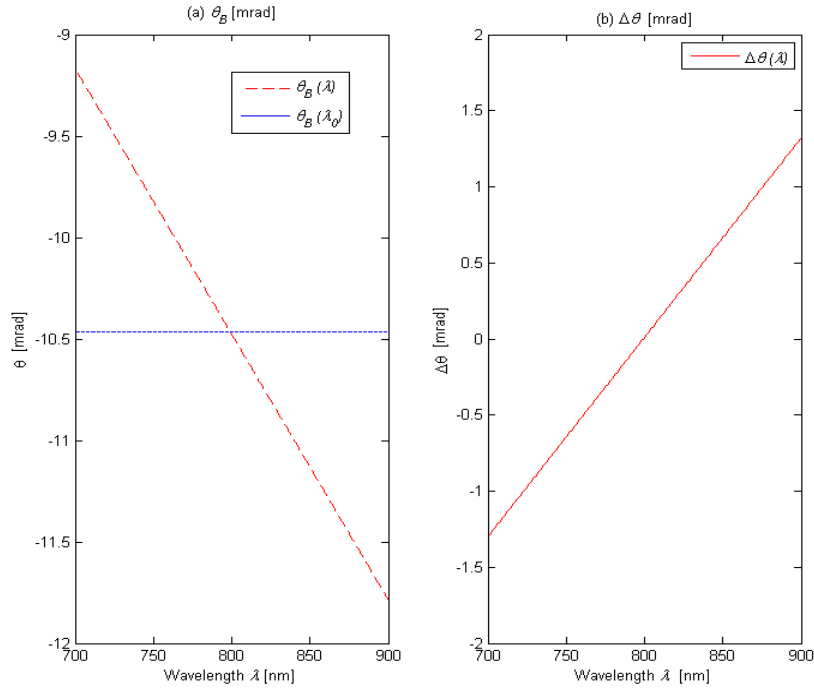


**Figure II-17. (a) Fix Bragg angle  $\theta_B(\lambda_0)$  defining the incident beam angle and effective Bragg angle  $\theta_B(\lambda)$  for an AOFS based on  $\text{TeO}_2$ ,  $F=110\text{MHz}$ . (b) Angular error  $\Delta\theta(\lambda)$ . Angles are outside the crystal.**

It is obvious that such discrepancies will have a strong effect on the diffraction efficiency and reduce the spectral transmittance considerably (see also Figure II-II-14). From Figure II-16 it is also obvious that coupling into a mono mode fiber will be difficult and the spectral transmittance will be further reduced. It becomes clear that angular correction before and after diffraction would potentially increase spectral transmittance considerably. The problem can actually be separated into two quite distinct parts:

- Correction before AOFS: increase diffraction efficiency
- Correction after AOFS: increase fiber coupling

### 4.3.2 Principle of angular correction

Wavelength-dependent angular deviation by passive elements can be either achieved by gratings or prisms. The comparison of properties in Table II-2 allows for choosing which the better choice for our application might be.

	Advantages	Disadvantages
Prism	<ul style="list-style-type: none"> <li>- Only one order</li> <li>- High efficiency if AR-coated</li> <li>- Potentially “quasi-linear” dispersion for achromatic prism</li> </ul>	<ul style="list-style-type: none"> <li>- Non-linear dispersion</li> </ul>
Grating	<ul style="list-style-type: none"> <li>- Quasi-linear dispersion, as AOFS</li> </ul>	<ul style="list-style-type: none"> <li>- Multiple diffraction orders</li> <li>- Low diffraction efficiency because of little lines illuminated</li> <li>- Weak free spectral range in higher diffraction orders</li> </ul>

**Table II-2. Design criteria: comparison prism-grating for evaluating optimal choice for angular error correction.**

The prism clearly seems to be the better candidate, even though it is more complicated to model and it can not be solved analytically but rather numerically.

Let us start with the generalized dispersion equation for a prism as a function of its apex angle  $\alpha$ , the angle of its bisecting line with respect to the vertical orientation  $\beta$ , its refractive index  $n(\lambda)$  and the beam incident angle  $\theta_1$  with respect to the horizontal orientation (see Figure II-18(lhs)) [20]:

$$\theta_4(\alpha, \beta, \theta_1, n(\lambda)) = \arcsin \left( \sin \left( \theta_1 - \left( \beta + \frac{\alpha}{2} \right) \right) \cos(\alpha) + \sqrt{n^2(\lambda) - \sin^2 \left( \theta_1 - \left( \beta + \frac{\alpha}{2} \right) \right)} \sin(\alpha) \right) + \left( \beta - \frac{\alpha}{2} \right). \quad (\text{II.15})$$

This result can be rearranged in order to describe the beam deviation  $\delta$  as illustrated in Figure II-18(rhs):

$$\delta(\alpha, \theta_{p1}, n(\lambda)) = \theta_{p1} + \arcsin \left( \sin(\alpha) \sqrt{n^2(\lambda) - \sin^2(\theta_{p1})} - \cos(\alpha) \sin(\theta_{p1}) \right) - \alpha. \quad (\text{II.16})$$

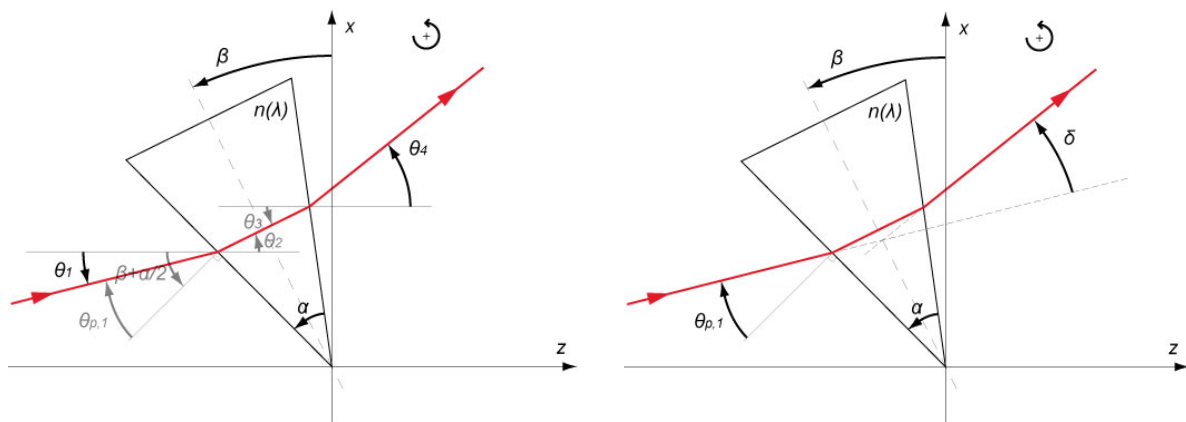


**Figure II-18. (lhs) Generalized prism equation. (rhs) Deviation  $\delta$  of a light beam.**

The refractive index  $n(\lambda)$  will be an important parameter for Equations (II.15) and (II.16) which is responsible for dispersion (angular spreading of spectrum) and also enables for compensating the dispersion induced by the AOFS. However, it is not adjustable since it is an individual property of a material. Theoretically the most linear dispersion characteristics would be most suitable in order to compensate for the linear dispersion induced by the AOFS. Without paying too much attention to this point we have chosen to do the following simulations based on two very common glass types: BK7 and Fused Silica.

In order to quantify numerically refractive indices one uses the Sellmeier equations or modified versions of it. The usual form of this equation reads:

$$n^2(\lambda) - 1 = \sum_i \frac{A_i \lambda^2}{\lambda^2 - \lambda_i^2}, \quad (\text{II.17})$$

where  $A_i$  and  $\lambda_i$  are material specific. Equations have been determined for many optical materials (crystals and glasses) and are valid over a certain spectral range [20].

### 4.3.3 Optimization of diffraction efficiency

From Figure II-17 one clearly sees how diffraction efficiency can be increased. Minimizing the angular difference  $\Delta\theta$  (Equation II.14) by pre-compensating it with a properly designed prism, introduced into the beam path before the AOFS, would probably already do the job.

Let us consider Equation (II.16). For a given material,  $n(\lambda)$  will be fixed. In a first step we will chose to orient the prism in order to achieve minimal deviation. By deriving Equation (II.16) and setting the result to zero one finds the relation:  $\theta_{p1} = -\theta_{p4}$  (see Figure II-18(lhs)), minimal deviation is realized for the central wavelength  $\lambda_0$  of our spectrum. Under this condition the beam within the prism is perpendicular to the bisection line of the prism base surface. It also represents the configuration with the least reflection losses at the interfaces for an uncoated prism and with TE polarization (this will be of some importance for our prototype realization, see §4.4). All variables beside the apex angle  $\alpha$  in Equation (II.16) are now determined (directly or indirectly) and numerical optimization of  $\alpha$  will hopefully lead to less angular errors  $\Delta\theta$ . *Root mean square* (RMS) of  $\Delta\theta$  was calculated with  $\alpha$  as the varying parameter. The resulting values for the apex  $\alpha$  can be seen in Table II-3:

	Spectral ranges	
	NIR: 700nm – 900nm	VIS + NIR: 400nm – 900nm
BK7	$\alpha_{\text{opt}} = 33.8^\circ$	$\alpha_{\text{opt}} = 17.6^\circ$
Fused silica	$\alpha_{\text{opt}} = 38.2^\circ$	$\alpha_{\text{opt}} = 20.7^\circ$

**Table II-3. Optimized apex angle  $\alpha$  for two current glasses and two different spectral ranges potentially interesting.**

Similar to Figure II-17 we trace again the Bragg angle  $\theta(\lambda)$  with calculated curves corresponding to a certain prism apex (see (a) of Figure II-19 and Figure II-20) and the angular difference with respect to the Bragg angle  $\Delta\theta(\lambda)$  ((b) of Figure II-19 and Figure II-20) for two different spectral ranges. One clearly sees a much improved situation. The curve with the  $30^\circ$  prism is the solution we opted for in order to realize a prototype of these devices. This prism was commercially available without need for custom fabrication (see §4.4).



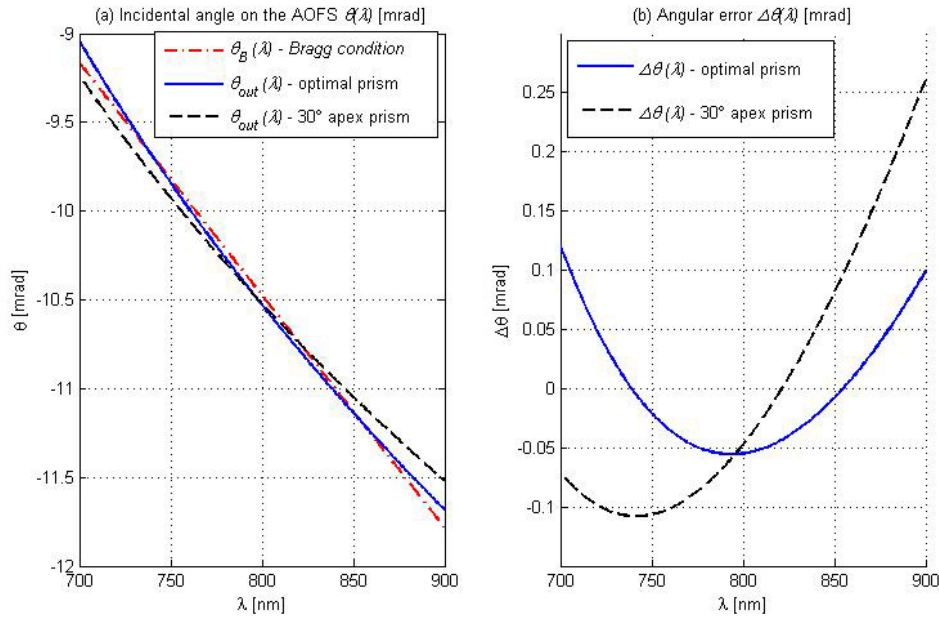


**Figure II-19. (a) Bragg angle  $\theta_B(\lambda)$ , output angle for the optimal prism apex  $\theta_{out,optimal}(\lambda)$ , and  $\theta_{out,30}(\lambda)$  for BK7. (b) Angular error  $\Delta\theta(\lambda)$  for curves in (a). Spectral range is NIR.**

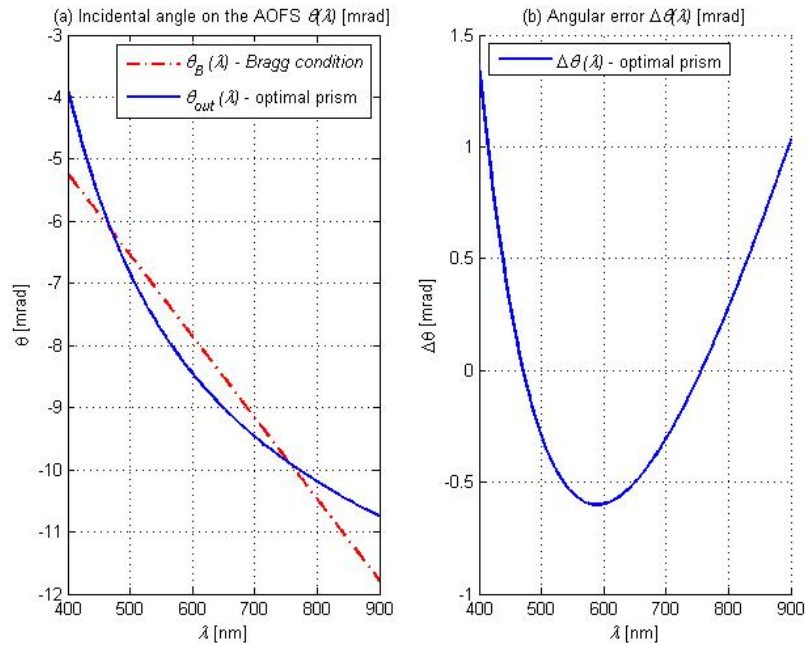


**Figure II-20. (a) Bragg angle  $\theta_B(\lambda)$ , and output angle for the optimal prism apex  $\theta_{out,optimal}(\lambda)$  for BK7. (b) Angular error  $\Delta\theta(\lambda)$  for curves in (a). Spectral range is VIS and NIR.**

The resulting normalized spectral transmittance (without taking into account reflection losses at interfaces) for the above calculated configurations, using Equation (II.12) for calculating the diffraction efficiency of the AOFS, can be seen in Figure II-21.

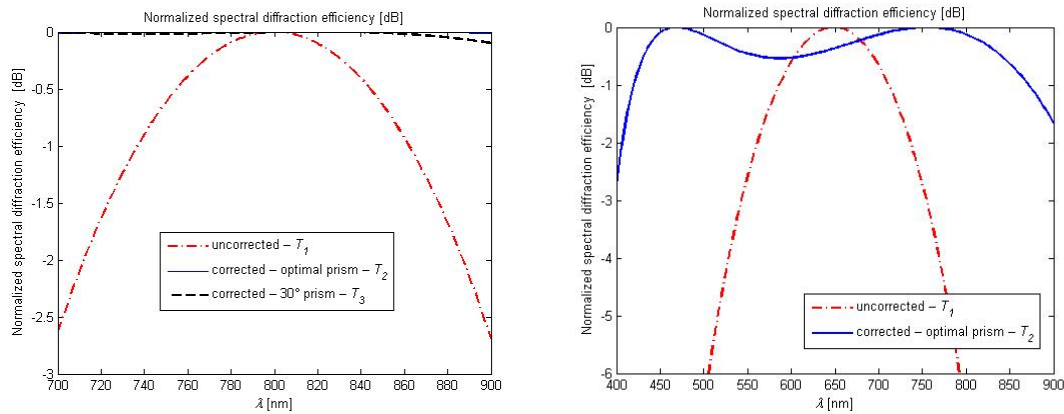


**Figure II-21. Normalized spectral transmittance (diffraction efficiency) for calculated curves in (lhs): Figure II-19 and (rhs): Figure II-20. Note: vertical axis (lhs) different from (rhs) for better visualization of corrected cases.**

#### 4.3.4 Fiber coupling efficiency optimization

In order to achieve maximum coupling efficiency into a glass fiber one has to achieve a maximum co-linearity (and not only parallelism) over the whole spectrum at the output of the AOFS. Such a performance can almost be achieved by placing an identical prism as illustrated in Figure II-22, since the angular distribution behind the AOFS is close to a symmetrical situation with respect to its input. The better the Bragg condition is matched in front of the AOFS, the better co-linearity after the second prism will be achieved. Figure II-13(lhs) is very helpful for understanding where coupling losses initially come from. A Bragg condition mismatch in the positive angular direction will affect the output in the same angular direction and is not symmetric with respect to the Bragg angle. This deviation will then propagate throughout the second prism.

A slightly different prism at the output could eventually present better performance. However, such a configuration was not calculated.

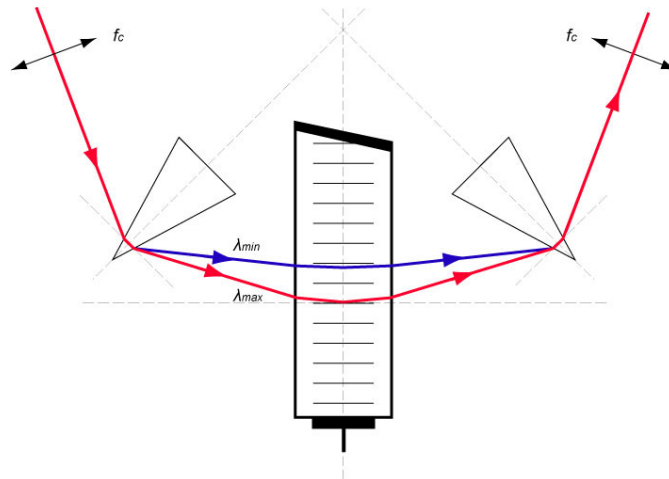


**Figure II-22. Symmetric system with respect to the AOFS longitudinal axis. The whole spectral output becomes collinear for perfectly matched Bragg condition.**

In order to calculate the coupling efficiency into a single mode fiber one can calculate the overlap integral between the electric field of the fiber and the light beam propagated until the fiber input. Assuming that the beam in front of the (paraxial) coupling lens is plane for each

wavelength, and assuming the electric field at the fiber input to be perpendicular with respect to the optical axis and presenting only a lateral displacement, the coupling coefficient reads:

$$C = \int u_1 u_2 \, dx dy = \int \sqrt{\frac{2}{\pi}} \frac{1}{\sigma} e^{-\frac{x^2+y^2}{\sigma^2}} \sqrt{\frac{2}{\pi}} \frac{1}{\sigma} e^{-\frac{(x-\rho)^2+y^2}{\sigma^2}} \, dx dy, \quad (\text{II.18})$$

with  $u_1$  being the electromagnetic mode field of the fiber, and  $u_2$  being the incident electromagnetic mode field as a function of  $\rho(\lambda)$  defined as  $\rho = f_c \cdot \tan(\Delta\theta_{out}(\lambda))$ .  $\sigma$  is defined as the mode waist of the Gaussian fit to the radial intensity variation of the fundamental mode (*i.e.*  $2\sigma$ =mode field diameter of fiber at  $1/e^2$ -intensity) [25]. We additionally assumed the focal length  $f_c$  to perfectly match the numerical aperture of the fiber (which is quite ok since for collimating and coupling the same focal length is used and at the input and output the same fibers are used as well) and neglecting chromatic aberrations (see Figure II-23). The result of this very simplified model is shown in Figure II-24, calculated for a focal length of  $f_c=3\text{mm}$ .

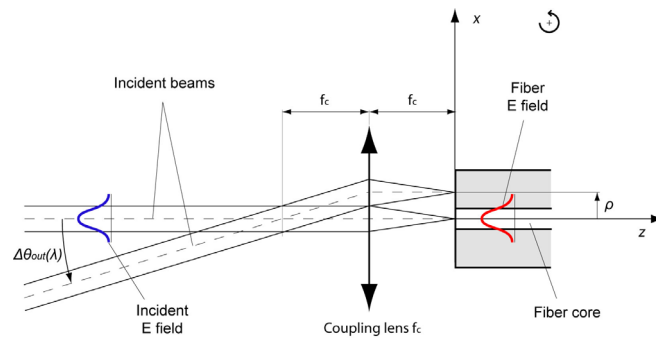


**Figure II-23. Coupling into single mode fiber for ideally coaxial incidence and with angle, for simplicity with pivot-point in back focal plane of collimation lens.**

It appears that the coupling efficiency is much more critical than the impact caused by diffraction efficiency once the prisms are introduced. Of course, shorter focal lengths would improve the situation but become more sensitive axially. The non-linear dispersion characteristics of a prism seems to have a strong influence for the case where an octave or more is aimed as spectral transmittance (diffraction plus coupling efficiency), especially if covering also shorter wavelengths in the VIS range where dispersion increases rapidly. As we will see later in this chapter, achromatic prisms could improve the situation considerably.

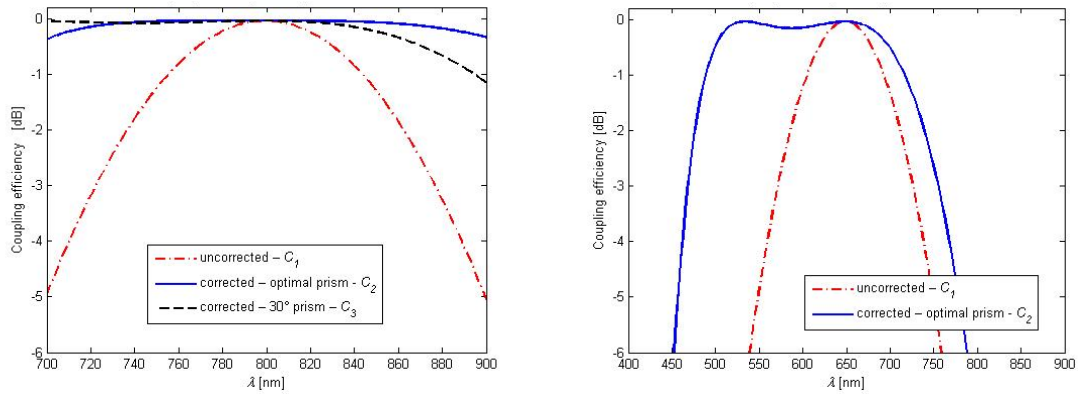


**Figure II-24. Normalized coupling efficiency C into single mode fiber for  $f_c=3\text{mm}$  and standard dispersion prisms positioned in accordance to minimum deviation. (lhs) NIR spectral range.  $C_1$ : uncorrected,  $C_2$ : corrected with optimal prism apex,  $C_3$ : corrected with  $30^\circ$  prism. (rhs) VIS and NIR spectral range. Uncorrected and corrected with optimal prism apex.**

### 4.3.5 Optimized overall spectral transmittance

If we combine the diffraction efficiency or transmission of the AOFS together with the coupling efficiency, a normalized overall transmission can be calculated (see Figure II-25). This graph shows clearly that the fiber coupling is much more limiting the spectral width than the Bragg condition mismatch causing reduced diffraction efficiency.

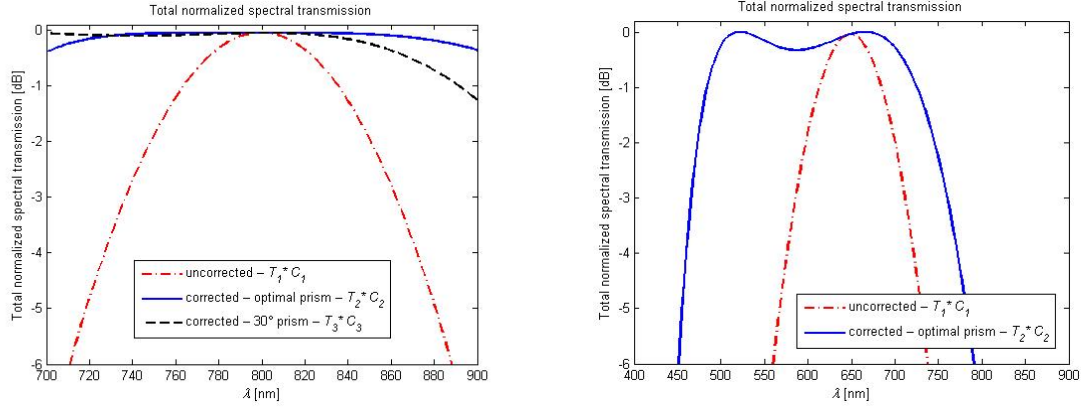


**Figure II-25. Total normalized spectral transmission for uncorrected and corrected cases (see previous paragraphs and figures for details). For ultra-broad spectra (rhs) a simple prism cannot compensate sufficiently anymore. Achromatic prisms with a more linear dispersion are needed.**

The spectral bandwidth of an uncorrected AOFS as calculated in the above paragraphs has a theoretical  $-3dB$  bandwidth of  $90nm$ . The theoretical Gaussian FWHM of a fs-Ti:S laser with central wavelength  $\lambda_0=800nm$  and spectral width  $\Delta\lambda_{FWHM}=140nm$  would be reduced to only  $74nm$ . With the above calculated configuration (blue curve in Figure II-25(lhs)) the bandwidth would be reduced only by  $5nm$  to  $\Delta\lambda_{FWHM}=135nm$ . Considering the price of such a light source it is worth the additional effort on the AOFS.

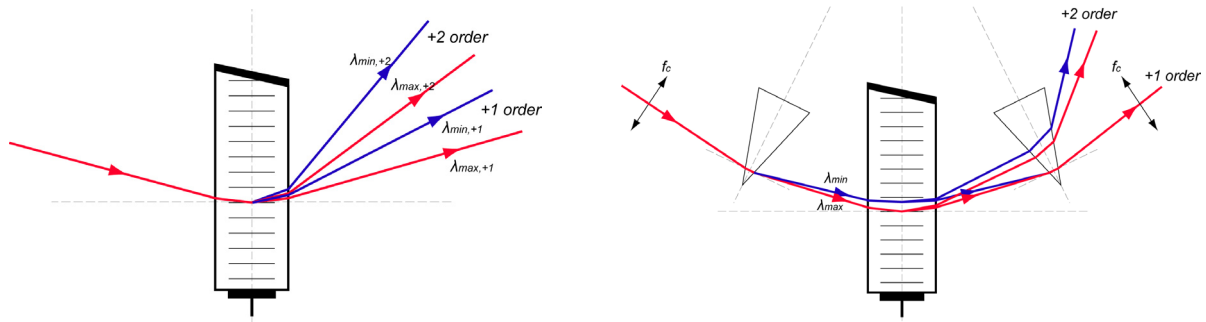


**Figure II-26. Free spectral range is not limiting transmittance if angular correction with prisms is implemented. The second diffraction order is bent away from the collinear direction.**

One could doubt that the spectral range covering more than an octave does not fit into the *free spectral range (FSR)*, often defined as:

$$FSR = \lambda_{max} - \lambda_{min} = \lambda_{max} / |m| + 1, \quad (II.19)$$

with  $m$  being the diffraction order and  $\lambda_{max}$  the wavelength exiting with the same angle as  $\lambda_{min}$  for the next higher diffraction order. For the situation with angular correction as we realized it, this limitation is not as restrictive and does not limiting the spectral bandwidth. If a second

order diffraction does exist, it is refracted away from the “collinear” first order, as illustrated in Figure II-26.

### 4.3.6 Further improvements

All above configurations showed standard dispersion prisms based on BK7, oriented such that deviation by the prisms is minimal (in order to have minimal reflection losses at the interfaces for uncoated prisms). The transmittance curve for an un-optimized apex angle in Figure II-24 showed some asymmetric behavior, suggesting some slight modifications to be done with respect to the orientation of the prisms and the coupling lens-fiber pair. Results after optimizing these parameters are shown in Figure II-28.

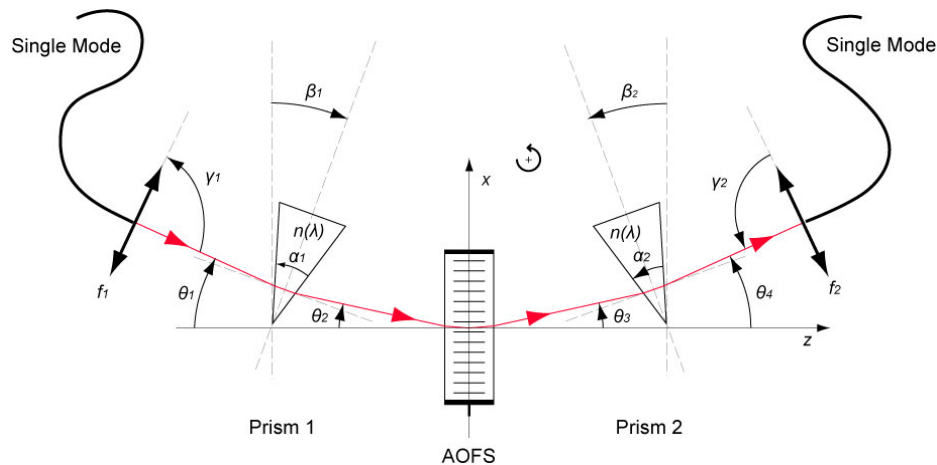


**Figure II-27. Configuration with standard prisms. Several parameters can be adjusted (see Table II-4) resulting in optimized transmittance characteristics as shown in Figure II-28.**

Standard prisms with $\alpha$ and $\beta$ optimal and slight tilt of coupler $\gamma_2$	
$\alpha$	$17.49^\circ$
$\beta_1 = -\beta_2$	$-5.08^\circ$
$\gamma_1$	$90^\circ$
$\gamma_2$	$90^\circ + 0.4 \text{ mrad}$
$\theta_1$	$-9.65^\circ$
$\theta_2$	$-3.9 \text{ mrad}$ to $-10.7 \text{ mrad}$
$\theta_3$	$6.1 \text{ mrad}$ to $12.8 \text{ mrad}$
$\theta_4$	$9.6^\circ$ to $9.8^\circ$

**Table II-4. Calculated parameters for standard prisms in BK7.  $f_c=3mm$ .**

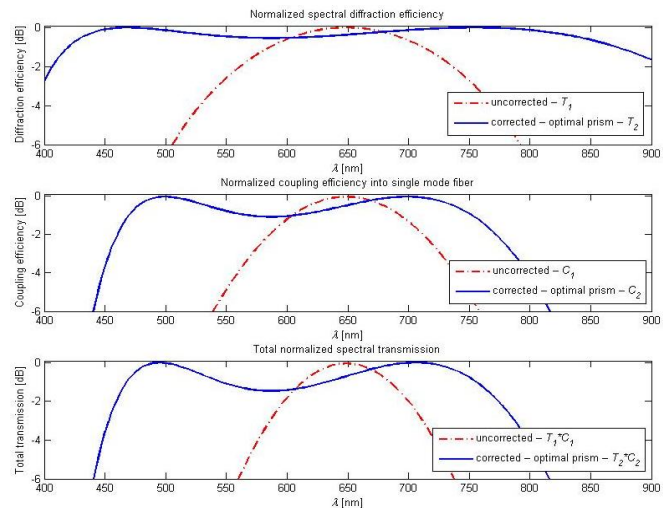


**Figure II-28. Calculated normalized transmittance curves for the standard prism configuration with optimized apex angle and orientation of prisms.**

It was already mentioned that achromatic prisms could potentially increase the transmittance due to a more linear dispersion characteristics. Such a configuration is calculated for a typical pair (crown and flint) of glasses, BK7 and SF6, and shown in Figure II-30. Of course many other combinations exist.

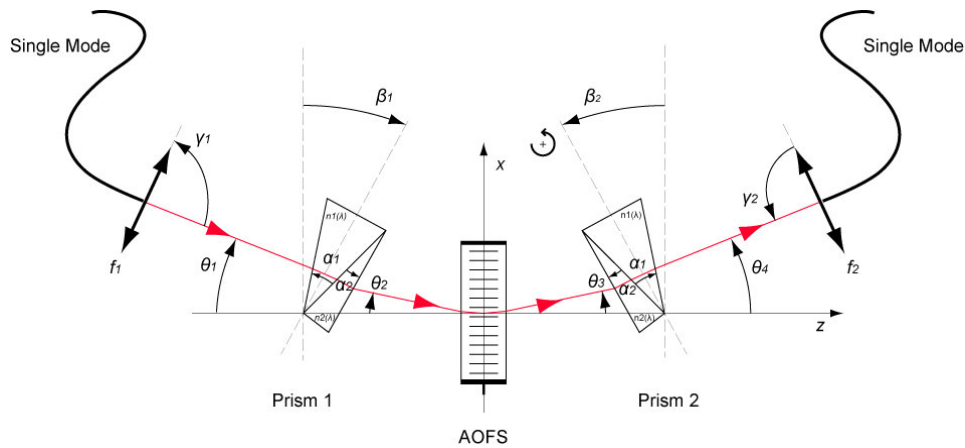


Figure II-29. Configuration with achromatic prisms. Parameters are adjusted according to calculations as shown in Table II-5. The resulting transmittance characteristics are shown in Figure II-30.

Achromatic prisms, $\alpha_1$ , $\alpha_2$ and $\beta$ optimal, no tilt of coupler: $\gamma_2$	
$\alpha_1$	$36.38^\circ$
$\alpha_2$	$6.08^\circ$
Crown ( $\alpha_1$ )	BK7
Flint ( $\alpha_2$ )	SF6
$\beta_1 = -\beta_2$	$-53.90^\circ$
$\gamma_1 = \gamma_2$	$90^\circ$
$\theta_1$	$-22.74^\circ$
$\theta_2$	$-5.53\text{mrad}$ to $-11.56\text{mrad}$
$\theta_3$	$4.88\text{mrad}$ to $11.95\text{mrad}$
$\theta_4$	$22.72^\circ$ to $22.75^\circ$

Table II-5. Calculated parameters for achromatic prism pairs.  $f_c = 3\text{mm}$ .

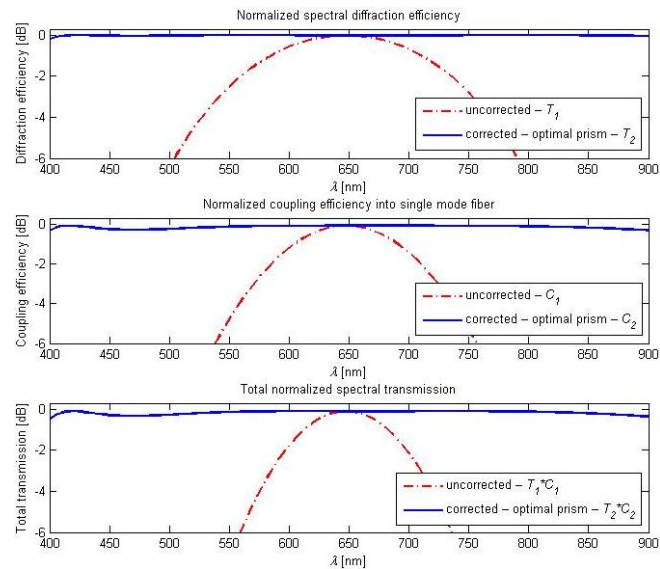


Figure II-30. Calculated normalized transmittance curves for achromatic prism pairs. Configuration with ideal apex angle and optimized tilt of prisms, as shown in Figure II-29.

Even though AR coatings will become very important for such rather steep angles, and input as well as output surfaces need specific coatings, the resulting transmittance characteristics as shown in Figure II-30 should justify a certain effort, since virtually no bandwidth limitation due to acousto-optic effects remain.



#### 4.4 Prototype realization and characterization of spectral transmittance

Two acousto-optic frequency shifters from AA Opto-Electronics with the following characteristics were available in the laboratory (see Figure II-31(lhs)):

Serial number	AA.ST.110/A1.VIS 0x 00.10
Material	TeO <sub>2</sub>
Acoustic frequency $F$	110MHz
Acoustic column height $H$	1mm
Mode	Longitudinal ( $V=4200m/s$ ) Isotropic interaction, TE linear polarisation
AR-coating	450-700nm
Quality factor $Q$ @532nm	11
Acousto-optic interaction length $L$	11mm

**Table II-6.** AOFS from AA Opto-Electronics available in our laboratory for prototype packaging. The devices were designed for the VIS spectral range from 450-750nm and thus not optimal for the use in NIR, but they were the only option available for prototype realization.

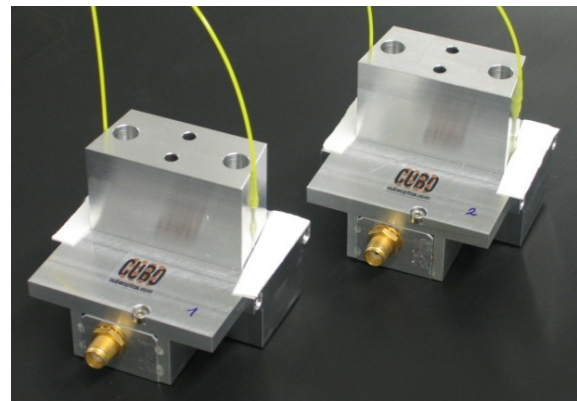
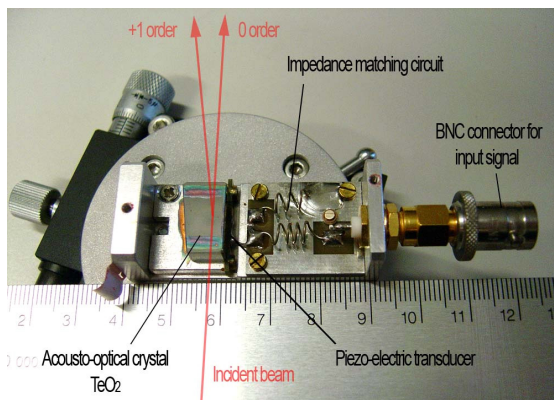


**Figure II-31.** (lhs) Acousto-optic frequency shifter from AA Opto-Electronics without top cover. One clearly sees the TeO<sub>2</sub> crystal with an interaction length of  $L=11mm$ . Two such devices were used in order to test the angular correction principle in order to increase bandwidth of the (fiberized) devices as shown at (rhs).

The main problem with these devices is the spectral range they were fabricated for: VIS from 450nm to 700nm instead of NIR (700nm to 900nm) where we had the OCT light source available. However, since we were less interested in the power transmission than learning about the spectral behavior we were still rather optimistic about manufacturing a first prototype with angular correction according to Figure II-27 and Table II-7, realized at the Cube Optics AG facilities in Mainz (Germany).

A drawing of the optical packaging is shown in Figure II-32 and the two assembled devices are shown in Figure II-31(rhs). Collimating and coupling optics consist of a parabolic 90° off-axis mirror with focal length of approx. 1.5mm (exact value is company-confidential), first mounted onto a miniaturized magnetic base (dark blue element in Figure II-32) and glued afterwards. This very short focal length would perfectly match an acoustic column height of 0.5mm (assuming fiber NA of 0.15). The available AOFS, presenting an acoustic column height of 1mm, would easily work with collimation optics of 3mm focal length (value used for calculations in §4.3.4 to §4.3.6) with negligible losses related to beam size. The two prisms in

BK7 are shown in yellow in Figure II-32. They were glued with a specific angle according to Table II-7 prior to placing and orientation of collimation and coupling optics.

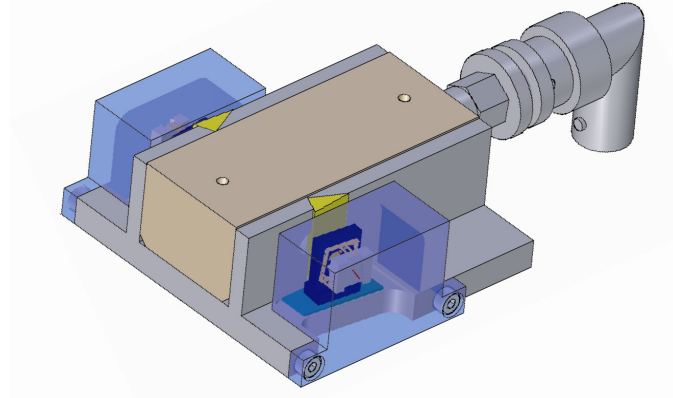


**Figure II-32. Drawing of broadband fiberized AOFS with angular correction. Packaging done at Cube Optics AG facility in Mainz (Germany).**

Prototype design parameters	
$\alpha_1=\alpha_2$	$30^\circ$
$\beta_1=-\beta_2$	$-8.62^\circ$
$\gamma_1$	$90^\circ$
$\gamma_2$	$90^\circ$ +slight tilt
$\theta_1$	$-16.64^\circ$
$\theta_2$	$-9.2\text{mrad}$ to $-11.5\text{mrad}$
$\theta_3$	$9.0\text{mrad}$ to $12\text{mrad}$
$\theta_4$	$16.63^\circ$ to $16.67^\circ$

**Table II-7. Calculated parameters for standard prisms with symmetric orientation for minimum deviation (minimum reflection losses for uncoated surfaces).  $f_1=f_2\approx 1.5\text{mm}$ . See also Figure II-27.**

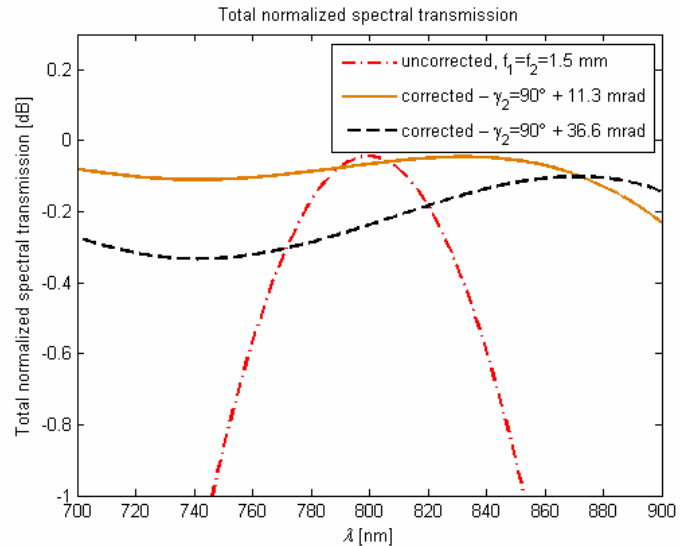


**Figure II-33. Normalized spectral transmittance for parameters as listed in Table II-7. The strong influence by the tilt of the coupling optics is well illustrated by the different curves.**

Spectral transmittance was measured using an optical spectrum analyzer. The spectral content was measured before and after the AOFS, and their ratio was calculated. Afterwards these characteristics were normalized resulting in Figure II-34. The light source employed was a fs-Ti:S laser with spectral FWHM of approximately  $135\text{nm}$  around its  $800\text{nm}$  central wavelength.



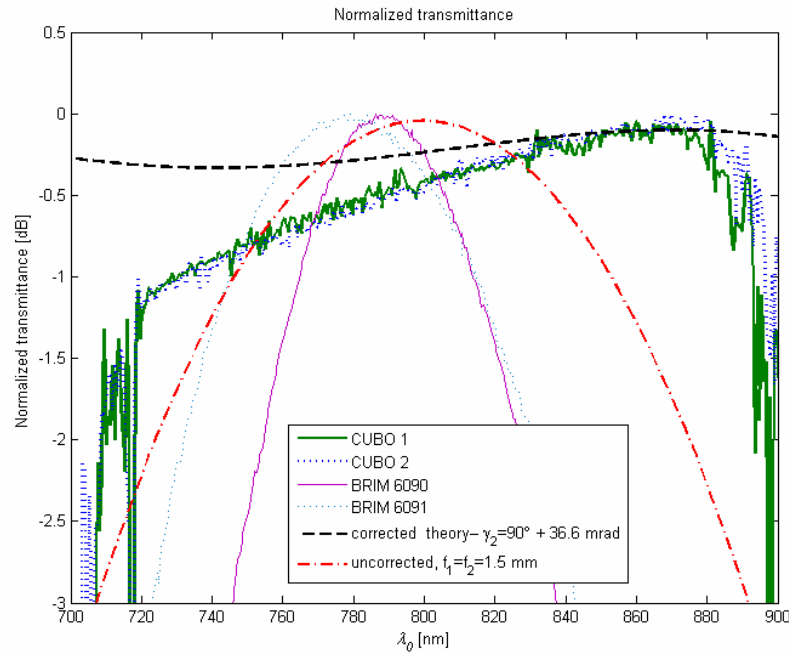


**Figure II-34.** Comparison of normalized transmittance of the two commercially available devices from Brimrose Inc. (BRIM 6090 and BRIM 6091) as used in the initial heterodyne setup (Chapter 3) and our two prototypes assembled at the Cube Optics facility in Mainz (CUBO 1 and CUBO 2). Latter AOFS were tested with the dual beam setup presented in Chapter 5. Linear polarization for this measurement was better than 200:1. For comparison theoretical curves are depicted as well.

One clearly sees a significant improvement in spectral transmittance of the angular corrected fiberized AOFS with respect to the commercial ones. It should be noted that both devices do have about the same focal length for collimating and coupling the light beam. Our prototypes show a very flat, but slightly tilted transmittance curve similar to predictions by theory where the coupling optics gets an additional slight tilt (dashed, blue curve in Figure II-33). The more pronounced tilt of the measured transmittance curve is supposed to be caused by uncompensated errors like residual aberrations, manufacturing adjustment errors (angle and position) as well as residual dispersion terms. As a matter of fact, while aligning during manufacturing, no true broadband light source was available. Three superluminescent diodes with different central wavelength were combined using fused fiber couplers in order to have a pseudo-broadband calibration light source. It could be that this was not optimal and caused some slight misalignment. Also, due to the AR coating in the VIS range the spectral transmission measurements during manufacturing might have lead to a different optimum alignment than with a proper NIR AR coating. With a next generation prototype these still open questions should be answered.

## 4.5 Conclusion

Limitation in spectral transmittance bandwidth was identified as the key limitation for achieving ultra-high resolution tomograms if AOFS are employed. In this chapter we have shown that a significant bandwidth increase is possible by placing two dispersion prisms with a specific angle and orientation in front and behind an acousto-optic device. Further improvement is realized by custom-made achromatic prisms presenting more linear dispersion behavior, useful for spectral bandwidth of more than 200nm. Even though the calculations were performed for a completely fiberized device, all results hold as well for a free-space

realization. In addition, two AOFS in a row, combining up- and down-shift in the same interferometer arm, would benefit from the same concept.

In case of a fs-Ti:S laser as a light source, and due to the improved bandwidth of the presented devices, a significant resolution loss of about 40% can be circumvented (for the case of fiberized devices). The realized prototypes, used for *in-vivo* measurements in the following chapter, show a very clear improvement in spectral transmittance, but do currently suffer from intensity losses, probably mainly due to uncoated prism and “wrongly” coated TeO<sub>2</sub> interfaces (VIS instead of NIR). A next generation broadband fiberized AOFS should present improved intensity transmission characteristics in addition to the shown spectral transmission properties.

Another drawback of the realized prototypes is the lack of polarization maintaining (PM) fibers. As a matter of fact it was not possible to manufacture the devices with PM fibers since this requires very precise angular orientation of the fiber fast axis with respect to the AOFS in order to achieve TE polarization with very high quality. Polarization control through fiber paddles works fine, but is difficult for very broad light sources and less stable over time due to *e.g.* slight temperature dependent behavior of the induced depolarization.

## Chapter 5

### Dual beam heterodyne FDOCT

#### 5.1 Introduction\*

In Chapter 3 we showed that heterodyne FDOCT avoids or suppresses artifacts and therefore it is a potential candidate for removing disturbing artifacts like mirror structures as well as increasing depth range; both for the spectrometer-based [26] as well as for the swept-source modality published by other groups [9, 10, 27]. The main issue for reliable heterodyne reconstruction is phase accuracy. Spectrometer-based FDOCT needs high phase stability between successive spectra. Any phase noise due to sample motion or beam scanning will cause signal degradation as well as insufficient suppression of mirror terms. This will be especially critical for *in-vivo* measurements. Another source of phase instabilities are fiber-based setups employing applicators where moving the sample arm fiber introduces uncontrollable phase changes.

A solution is a common path configuration where sample and reference beam travel through the same fiber to the sample or more generally to an applicator. For the true common path concept a prominent sample arm reflection serves as reference signal in which case reference and sample field exhibit maximum relative phase stability. Particularly phase contrast schemes profit of the enhanced phase stability enabling highly sensitive optical path length variations [28-32]. The other common path variant is to have a separate reference arm by placing the interferometer into the hand piece or applicator, as was demonstrated by Tumlinson *et al.* with an endoscope configuration [33].

The concept of a common path with a prominent sample reflection as a reference captivates by its simplicity due to the fact that it does not need an extra interferometer. As already mentioned a prominent reflection ( $R_1$ ) situated close to the sample structure ( $R_2$ ) serves as the reference arm (see Figure II-35), resulting in a relative delay of  $2\Delta z$ . Such a configuration presents extremely high phase stability; values down to  $18\text{pm}$  for spectrometer-based [34] and  $39\text{pm}$  for swept-source based [32] OCT systems have already been reported. However, not much flexibility is offered since the reference reflector must always be close to the sample structure. Also beam scanning might be problematic if the probe scan is not telecentric in order to guarantee a stable reference reflection intensity. Usually a glass window may serve as

---

\* This chapter was partly published in the following peer-reviewed article:

A. H. Bachmann, R. Michaely, T. Lasser, and R. A. Leitgeb, „Dual beam heterodyne Fourier domain optical coherence tomography,“ *Opt. Express* (2007), in press.

a reference interface. Nevertheless, the thickness of the glass plate will reduce the achievable depth range apart from the possibility of ghost terms due to the reflections on both glass interfaces. Using the interface that is closer to the sample as reference might improve the situation but the drawback will still be a changing reference reflectivity and thus a changing OCT signal if the sample is in contact with the interface. The only sensible application to profit from the extraordinary phase stability of such configuration seems to be coherent phase microscopy [28-31].

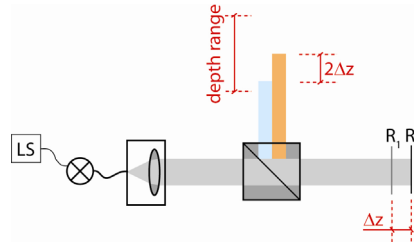


**Figure II-35. Concept of a common path configuration. A prominent reflection ( $R_1$ ) close to the sample structure ( $R_2$ ) is used as reference signal.  $\Delta z$  is the optical path difference between the sample interfaces  $R_1$  and  $R_2$ .**

The motivation for this chapter is to introduce a dual beam FDOCT variant that profits from the high phase stability of a common path configuration if used in conjunction with handheld applicators, without sacrificing measurement depth range, and keeping the flexibility for beam scanning as well as the possibility of dispersion balancing. In the following we present the method with a detailed discussion of signal-to-noise and dynamic range issues. Finally we demonstrate the feasibility to perform *in-vivo* measurements employing spectrometer-based heterodyne FDOCT.

## 5.2 Method

### 5.2.1 FDOCT dual beam configuration

A dual beam configuration is an extension of a common path setup presented in the previous paragraph. Instead of a single light beam traveling the common path to the reference ( $R_1$ ) and the sample ( $R_2$ ) as illustrated in Figure II-35, two beams delayed by an optical path length  $2\Delta z_{ILS}$  enter the common path and travel together to the reference and sample (see Figure II-36(a)). In this case, again, both reference and sample light share the same path and as a result exhibit much improved relative phase stability. This concept has been adapted for time domain OCT in particular for precise eye length measurements in order to remove artifacts due to axial proband motion [35, 36].

In the simplest case, a single reflecting sample surface and one reference reflector cause four light fields with relative respective delays. Depending on the optical distance  $\Delta z$  between reference  $R_1$  and sample  $R_2$  and the introduced delay  $\Delta z_{ILS}$  within the interferometric light source (ILS) (see Figure II-36(a)), a perfect match in relative time delay between the two fields can be achieved, as illustrated in Figure II-36(a) for  $\Delta z_{ILS} = \Delta z_0$ . As a matter of fact, all light fields present within the unambiguous depth range of the Fourier domain system (spectrometer-based or swept source) are coherently summing up and contribute to the detected interference signal. This clearly constrains the achievable system dynamic range. However, the potential of the dual beam configuration lies in the possibility to choose an arbitrarily distant interface in the common path as reference by matching the respective delay  $\Delta z_{ILS}$  of the interferometric light source as illustrated in Figure II-36(b).

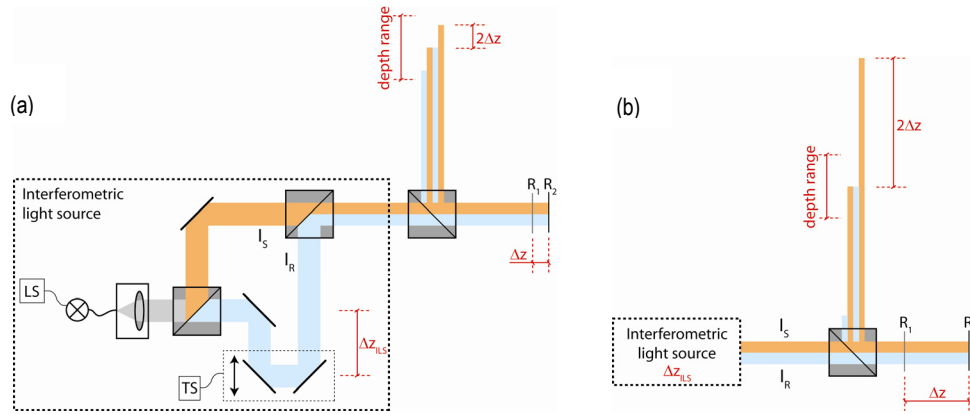


**Figure II-36. (a) Dual beam principle.** The output of an interferometer with a relative delay of  $2\Delta z_{ILS}$  between the two light beam intensities  $I_R$  and  $I_S$  (interferometric light source) is pre-compensating for the relative distance between  $R_1$  (reference surface) and  $R_2$  (sample). The configuration presents a small relative distance  $\Delta z$  between reference surface ( $R_1$ ) and sample ( $R_2$ ) and up to four cross correlation terms might occur. The blue beam can be considered as the reference beam. **(b) Dual beam configuration presenting a large relative distance  $\Delta z$  as compared to the depth range of the spectrometer (or swept source respectively) and only one cross correlation term occurs.**

In the most general way, the intensity of the total optical field adding up on the camera array in case of a single reflecting sample surface can be written as

$$\begin{aligned}
 I_{CCD} &= \left( E_R^{(r)} + E_R^{(s)} + E_S^{(r)} + E_S^{(s)} \right) \cdot \left( E_R^{(r)*} + E_R^{(s)*} + E_S^{(r)*} + E_S^{(s)*} \right) \\
 &= \begin{matrix} E_R^{(r)} E_R^{(r)*} + E_R^{(r)} E_R^{(s)*} + E_R^{(r)} E_S^{(r)*} + E_R^{(r)} E_S^{(s)*} + \\ E_R^{(s)} E_R^{(r)*} + E_R^{(s)} E_R^{(s)*} + E_R^{(s)} E_S^{(r)*} + E_R^{(s)} E_S^{(s)*} + \\ E_S^{(r)} E_R^{(r)*} + E_S^{(r)} E_R^{(s)*} + E_S^{(r)} E_S^{(r)*} + E_S^{(r)} E_S^{(s)*} + \\ E_S^{(s)} E_R^{(r)*} + E_S^{(s)} E_R^{(s)*} + E_S^{(s)} E_S^{(r)*} + E_S^{(s)} E_S^{(s)*} \end{matrix} \quad (II.20)
 \end{aligned}$$

with  $E_{R,S}^{(r,s)} = \sqrt{I_{R,S}^{(r,s)}(k)} e^{j(kz_{R,S}^{(r,s)})}$  being the detected reference and sample light fields respectively, with  $I_{R,S}^{(r,s)} = I_{R,S} \rho_{r,s}^2$  being the light intensity contributions at the detector and  $\rho_r$  being the amplitude reflectivity of  $R_1$  in Figure II-36 and  $\rho_s$  the sample amplitude reflectivity ( $R_2$  in Figure II-36), both also accounting for coupling losses, additional losses on optical elements and the diffraction grating efficiency. The upper indexes (r) or (s) indicate contributions from the reference beam  $I_R$  or the sample beam  $I_S$  of the ILS respectively.  $k$  stands for the wavenumber and  $z_{R,S}$  are the integral optical path lengths traveled by the respective light fields. The shading in Equation (II.20) visualizes the different contributions to the signal generation: the green shaded elements correspond to the four DC terms; the yellow elements are the complex conjugates to the ones on the bottom left side of the DC terms; the red shaded elements are zero if the reference surface is placed far away from the sample surface (see Figure II-36(b)) such that the coherence function becomes zero and no interference will occur anymore; for the same reason the blue shaded elements would vanish as well due to the matched delay  $\Delta z_{ILS} \approx \Delta z$  between the two fields  $E_R$  and  $E_S$ .

Finally the DC components as well as the actual sample-reference cross-correlation term in the lower left corner of Equation (II.20) together with its complex conjugate add to the total intensity  $I_{CCD}$ . The delay  $\Delta z_{ILS}$  can be used to adjust the position of the sample structure within the unambiguous depth range.

In case of the reference interface being close to the actual sample structure all terms given in Equation (II.20) are encountered. One could introduce a dispersion unbalance between the reference ( $R_1$ ) and the sample ( $R_2$ ) field, and place double the dispersion into the reference arm of the ILS. Different undesired cross correlation terms would then be attenuated since they experienced double or quadruple dispersion whereas the actual cross-correlation terms were dispersion balanced.

Nevertheless one still suffers from the complex conjugate mirror terms that lead to a reduced maximum system depth range and might obstruct the structure reconstruction.

### 5.2.2 Heterodyne dual beam FDOCT

The concept of heterodyne spectrometer-based FDOCT [26] was already discussed in Chapter 3: slight detuning of two acousto-optic frequency shifters in the reference and sample arm of the interferometer causes an achromatic beating signal with frequency  $\Omega = |\omega_R - \omega_S|$ . By quadrature detecting this timely varying signal the full complex signal can be reconstructed and the unambiguous depth range is doubled. For this purpose the detector is locked to four times the beating frequency, resulting in  $\pi/2$  phase shifted copies of the time dependent interference signal components. The frequency-shifted light fields can be written as

$$E_{R,S}^{(r,s)} = \sqrt{I_{R,S}^{(r,s)}(k)} e^{j(kz_{R,S}^{(r,s)} - (\omega_0 + \omega_{R,S})t)}, \quad (\text{II.21})$$

with  $\omega_0$  being the light frequency and  $\omega_{R,S}$  the frequency shift induced by the acousto-optic frequency shifters. The resulting signal detected by the line scan camera therefore becomes, for the case where reference and sample are well separated (see Figure II-36(b)),

$$I_{CCD}(k, t) = I_R^{(r)}(k) + I_R^{(s)}(k) + I_S^{(r)}(k) + I_S^{(s)}(k) + 2\sqrt{I_R^{(r)}(k)I_S^{(s)}(k)} \cos(\Omega t - \Psi), \quad (\text{II.22})$$

with  $\Psi$  containing all time-independent phase terms. Beside the additional DC terms  $I_R^{(s)}(k)$  and  $I_S^{(r)}(k)$ , this signal is equal to a standard heterodyne FDOCT configuration and has the same properties with respect to the suppression of mirror terms. Dual beam heterodyne FDOCT therefore allows for displacing the actual sample structure along the full doubled depth range by adjusting the distance  $\Delta z_{ILS}$ .

The DC and auto-correlation terms due to internal interferences between sample structure fields can be further eliminated using a differential complex signal reconstruction according to Equation (II.5):

$$\tilde{I}_{2x2}(k, t_0) = \tilde{I}(k, t_0) - \tilde{I}\left(k, t_0 + \frac{\pi}{\Omega}\right) = 2\left(I_{AC}(k, t_0) - jI_{AC}\left(k, t_0 + \frac{\pi/2}{\Omega}\right)\right), \quad (\text{II.23})$$

with  $\tilde{I}(k, t_0) = I(k, t_0) - jI\left(k, t_0 + \frac{\pi/2}{\Omega}\right)$  being the complex reconstructed interference signal of two adjacent spectra recorded at an arbitrary time instance  $t_0$ .

### 5.2.3 Sensitivity and dynamic range

Sensitivity and dynamic range ( $DR$ ) are important issues in spectrometer-based FDOCT. In practice, the  $DR$  depends on the reference light power being set close to the saturation level of the detector in order to achieve maximum sensitivity. It is evident that the dual beam configuration will present smaller sensitivity than standard FDOCT due to the presence of a second strong DC signal  $I_S^{(r)}(k)$  not serving as reference signal for coherent amplification but

reducing CCD dynamics. We would therefore analyse in detail on *DR* and sensitivity of the dual beam configuration as compared to the standard configuration in spectrometer-based FDOCT.

In §5.2.1 we defined the beam intensities in the ILS (see Figure II-36(a)) to be  $I_R$  and  $I_S$  respectively. The corresponding amount of generated photoelectrons [12, 37, 38] is then  $N_{R,S}(k) = I_{R,S}^{(r,s)}(k) \beta(k) A_{pixel}$  with  $\beta(k) = \tau \eta(k) / \hbar k c$  as the photon conversion factor with the reduced Planck constant  $\hbar$ , the vacuum light speed  $c$ ,  $\tau$  the integration time of the camera,  $\eta(k)$  the detector quantum efficiency,  $\hbar k c$  the photon energy in vacuum, and  $A_{pixel}$  the size of a detector pixel. We further express the total spectrally integrated number of photoelectrons as function of the spectral peak value as  $N_{tot} = \alpha N(k_0)$ , with  $k_0$  being the centre wavenumber where the detected spectrum is assumed to have its maximum. For a Gaussian spectrum with the spectral FWHM being imaged onto  $N/m$  pixels, *i.e.*  $\Delta k_{FWHM}^{(n)} = N/m$ , we have  $\alpha_{Gauss} = \Delta k_{FWHM}^{(n)} \sqrt{\pi / (4 \ln 2)}$ , where  $N$  is the total number of detector pixels, and  $m$  defines the ratio of  $N$  to the FWHM. In case of a rectangular spectrum  $\alpha_{rect} = N$ . According to Equation (II.22) the signal term can be written as

$$N_{signal}(k) = N_{AC}(k) = 2\sqrt{N_{ref}(k) N_{sample}(k)} \cos(\Omega t - \Psi), \quad (\text{II.24})$$

with  $N_{ref}(k) \equiv \beta(k) I_R(k) \rho_r^2 A_{pixel}$  and  $N_{sample}(k) \equiv \beta(k) I_S(k) \rho_s^2 A_{pixel}$ . An additional assumption we make is that the presence of a reference surface in the sample arm does not influence the ratio of sample to reference reflectivity  $\rho_s/\rho_r$  significantly, which means that the transmittance of the reference surface is high. With the approximation  $\rho_r^2 \gg \rho_s^2$ , we consider only those fields for the DC term that are reflected at the reference interface  $R_1$ :

$$N_{DC} \approx N_{ref}(k) + N_{sample}(k) \frac{\rho_r^2}{\rho_s^2} \equiv \gamma N_{sat}, \quad (\text{II.25})$$

where we define a load factor  $\gamma$  as the ratio between DC level and the pixel saturation level  $N_{sat}$ . This definition will be useful for our dynamic range discussion since the maximum sample signal will clearly depend on the remaining pixel capacity. We would further like to find the optimum ratio  $\xi$  between the ILS intensities  $I_R$  and  $I_S$ . With the definition  $I_S \equiv \xi I_R$  and Equation (II.25), the number of photoelectrons corresponding to the sample signal becomes

$$N_{sample} = \xi \frac{\rho_s^2}{\rho_r^2} N_{ref} = \frac{\xi}{1 + \xi} \frac{\rho_s^2}{\rho_r^2} \gamma N_{sat}. \quad (\text{II.26})$$

The signal-to-noise ratio (SNR) can be defined as  $SNR = \langle S_{OCT}^2 \rangle / \hat{\sigma}^2$ , with  $\langle \bullet \rangle$  being the time average,  $S_{OCT} = FT\{N_D(k)\}|_{z_0}$  being the signal peak at the position  $z_0 = \Delta z - \Delta z_{ILS}$  after Fourier Transform (FT) and  $\hat{\sigma}$  the noise variance after FT. Following [12] the squared OCT signal reads  $\langle S_{OCT}^2 \rangle = (\alpha N_{AC}(k_0) / (2N))^2$ . The noise variances before and after FT are related via  $\hat{\sigma}^2 = \sigma^2 / N$ . For shot-noise limited detection it can be expressed by the pixel-averaged total DC signal with Equation (II.25) as  $\hat{\sigma}^2 \approx (1/N)(\alpha \gamma N_{sat} / N)$ . Together with Equation (II.26), the SNR becomes

$$SNR = \alpha \gamma N_{sat} \frac{\rho_s^2}{\rho_r^2} \frac{\xi}{(1 + \xi)^2}. \quad (II.27)$$

First, we observe that the SNR increases linearly with the load factor  $\gamma$ . Second, the SNR expression reaches a maximum for  $\xi=1$ , or  $I_R=I_S$ . In words, the two interferometer arms of the ILS should have the same intensity in order to achieve a maximum SNR in dual beam interferometry. This is an important conclusion which will facilitate the following comparison of dual beam to standard FDOCT.

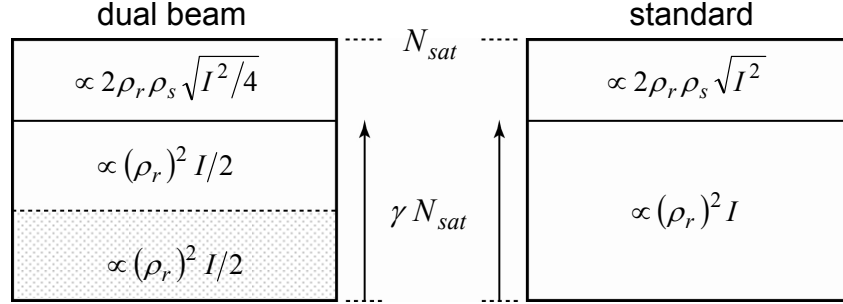


**Figure II-37. Scheme illustrating the filling of a camera pixel in case of dual beam and standard FDOCT respectively.**

Figure II-37 shows in an intuitive way the signal contributions on camera pixel level at spectral position  $k_0$  with equal load factor  $\gamma$  (detected signal when sample light is blocked) where we assume the cosine in Equation (II.22) to be 1. Since maximum SNR is achieved for both arms of the ILS at equal intensity ( $\xi=1$ ) we can write  $I_R=I_S=I/2$ . The dotted region indicates the light intensity reflected by the reference surface  $R_1$  which does not contribute to coherent amplification – but still contributes to shot noise and burdens the sample with additional light power. Hence, the effective reference signal for dual beam is only half that of the standard configuration with equal noise floor which results in a decreased SNR. According to Figure II-37 the SNR can be expressed as:

$$SNR_{dual} \propto \rho_s^2 I, \text{ and } SNR_{std} \propto 4\rho_s^2 I, \text{ thus } SNR_{dual} = SNR_{std}/4. \quad (II.28)$$

However, the maximum SNR is the same for both configurations as it is limited by the saturation value of the camera pixel. This implies the relation for the maximum sample reflectivity assuming equal reference signal:

$$\left(\rho_{s,dual}^{(max)}\right)^2 = 4\left(\rho_{s,std}^{(max)}\right)^2. \quad (II.29)$$

The sensitivity  $\Sigma$  on the other hand is defined as the inverse of the smallest detectable sample reflectivity  $\left(\rho_s^{(min)}\right)^2$  i.e.  $\Sigma = 1/\left(\rho_s^{(min)}\right)^2$  for  $SNR \equiv 1$ . From Equation (II.28) and with the same load factor  $\gamma$  for both configurations, we can write:

$$\Sigma_{dual} = \frac{1}{4} \Sigma_{std}, \quad (II.30)$$

which is a -6dB disadvantage in sensitivity for dual beam as compared to standard FDOCT. Together with Equation (II.29) we can deduce the following relation:

$$\left(\rho_{s,dual}^{(max)}\right)^2 / \left(\rho_{s,std}^{(max)}\right)^2 = \left(\rho_{s,dual}^{(min)}\right)^2 / \left(\rho_{s,std}^{(min)}\right)^2, \quad (II.31)$$



*i.e.* the ratio between maximum and minimum sample reflectivity remains the same.

This relation leads directly to an implication for  $DR$  which is defined as the ratio between the maximum to the minimum  $SNR$ . For a given reference intensity and load factor  $\gamma$ , the maximum  $SNR$  is achieved for the maximum sample reflectivity  $(\rho_s^{(max)})^2$ . Since the minimum  $SNR$  depends on the minimum sample reflectivity and considering Equation (II.31), the  $DR$  will remain the same for dual beam and standard FDOCT:

$$DR_{dual} = DR_{std} \propto N_{sat} \frac{(1-\gamma)^2}{\gamma}. \quad (II.32)$$

One could be tempted to increase the  $SNR$  by increasing the load factor  $\gamma$  (cf. Equation (II.27)). However, changing  $\gamma$  from *e.g.* 0.7 to 0.8 increases the  $SNR$  by less than +1dB while decreasing the  $DR$  already by -4dB (cf. Equation (II.32)). The situation becomes even worse for larger load factors.

### 5.3 Experimental

A Mach-Zehnder interferometer concept as shown in Figure II-38 was built. The spectrometer consisted of a collimator with a focal length of 80mm, a transmission diffraction grating (1200lines/mm), an objective (CL) with a focal length of 135mm and a line scan camera (ATEMEL AVIIVA M2, 2048pixel, 12bit) driven at 17.4kHz line rate. The light source (LS) was a fs-Ti:S laser with centre wavelength at 800nm and a bandwidth (FWHM) of 130nm. The effectively by the spectrometer detected bandwidth (FWHM) was 90nm (the strong bandwidth reduction was caused by multiple collimation and fiber coupling with aspheric instead of achromatic lenses: current availability in the laboratory). The maximum depth range (after complex signal reconstruction) was 4mm and the axial resolution in air was 4μm. The signal drop-off along the depth range was approximately -7dB/mm.

The peculiarity of the proposed system is the light source module comprising an interferometer with two acousto-optic frequency shifters (AOFS) (AA Opto-Electronic SA, packaged by Cube Optics AG (see also §4.4),  $\omega_R=2\pi\cdot 100MHz$ ,  $\omega_S=2\pi\cdot 100MHz+4.35kHz$ ). Since our acousto-optic elements are based on a birefringent crystal (tellurium dioxide (TeO<sub>2</sub>)) light has to enter these devices in a controlled, linear polarization state (TE mode). In addition, in order to maximize interference contrast, the light field states at the common path input have to be oriented accordingly, employing polarization control paddles (PC) also after frequency shifting (see Figure II-38). The sample was finally illuminated by two frequency shifted copies of the original light field. The dispersion compensation (Disp) in the reference arm of the ILS pre-compensated for the additional dispersion mainly induced by the applicator. The reference arm length could be adjusted by means of a translation stage (TS). Beam splitting and recombination was realized by a fiber coupler (FC) and a 50:50 beam splitter (BS) respectively.

Two different applicators, presented more in detail in §5.4, were designed and realized in order to test the concept on biological samples. The hand piece shown in Figure II-38 and presented in §5.4.1 consisted of a scanning unit based on a single mirror tip/tilt scanner (X/Y scan) [39]. A prominent reference reflection ( $R_1$ ) was realized by means of an uncoated glass wedge. The theoretical beam width on the sample in this case was 26.5μm (1/e<sup>2</sup>-intensity) with a Rayleigh range of 1.3mm and was defined by the ratio of the focal lengths ( $f_1=15mm$ ,  $f_2=75mm$ ) used in the applicator and the mode field diameter of the one meter long single

mode (SM) fiber. With a transverse scanning speed across the sample of  $40\text{mm/s}$  the resulting transverse over-sampling was approximately  $12\times$ . The sensitivity close to the zero delay was about  $95\text{dB}$  with  $2\times 1.1\text{mW}$  light power incident on the sample and a load factor  $\gamma$  of 0.8. Using Equation (II.27) the theoretical sensitivity is calculated to be  $\Sigma_{\text{dual}} \approx 101\text{dB}$  with  $\xi=1$ ,  $\alpha=800$ ,  $\gamma=0.8$ ,  $N_{\text{sat}} \approx 1.2 \cdot 10^5$  and  $\rho_r^2 \approx 1.4 \cdot 10^{-3}$ .

In order to properly reconstruct the complex signal as described in §5.2.2 and §3.2.2 respectively, special attention has to be paid to the synchronization of the camera with the resulting beating frequency (see (a) in inlet A of Figure II-38). The complex differential reconstruction needs two pairs of complex reconstructed spectra  $\tilde{I}(k)$  (thus in total four by  $90^\circ$  retarded acquisitions) which is realized by externally triggering the camera frame grabber (see (b) in inlet A of Figure II-38). Identical to standard heterodyne FDOCT (see Chapter 3), frequency shifters and trigger signal generators were linked and synchronized via a common  $10\text{MHz}$  time base (see also §3.3.2). The exposure time  $\tau$  (see (c) in inlet A of Figure II-38) was  $45\mu\text{s}$ . The complex spectra  $\tilde{I}(k)$  (see §5.2.2) were finally reconstructed using two successively recorded spectra as indicated by (d) in inlet A of Figure II-38(d).

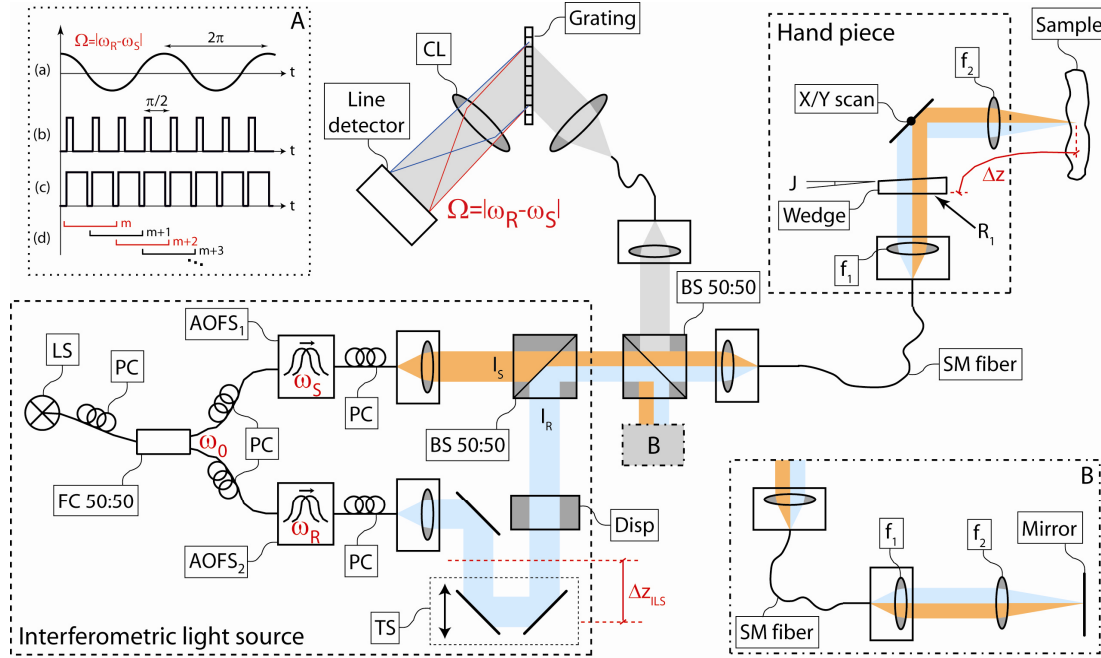


**Figure II-38. Dual beam heterodyne FDOCT.** Inlet A depicts synchronization of the line detector ((b) trigger and (c) exposure time) with (a) the beating signal. Inlet B shows the reference arm added (same fiber length as in sample arm) and used for phase stability comparison (§4) between the dual beam and the standard configuration. See text for details.

With the extension shown in inlet B of Figure II-38 we had the flexibility to compare the phase stability of the following three configurations (see §5.5):

- Common path: By blocking the dual beam arm and placing a thin glass plate instead of the mirror in inlet B.
- Dual beam: By blocking the external reference arm (inlet B). For phase stability measurement a mirror was used as sample without X/Y scanner.
- Standard: Cross-correlation between mirror of inlet B and mirror at sample position of the dual beam arm (top right corner in Figure II-38).

Dual beam and standard FDOCT could be measured simultaneously by adjusting the two respective reference signals  $R_1$  (for dual beam) and mirror of inlet B (for standard) to  $\gamma \approx 0.4$  each.

## 5.4 Applicators

### 5.4.1 Single mirror tip/tilt scanner

A first hand piece was based on an existing single mirror tip/tilt scanner [39]. The scanning device was placed in the back focal plane of lens  $f_2$ , allowing a two-dimensional transverse (telecentric) scanning of the sample (see Figure II-38). Such configuration scans with a convergent cone parallel to the optical axis. This results in a constant magnification in depth. Beside that, the main advantage of a single pivot point for a bi-dimensional scan consists in the fact that pupil matching is achieved with one single relay optics. Pupil matching is especially important for ophthalmic imaging or microscopy applications, but less for this particular design.

The reference reflector ( $R_1$ ) was realized by placing a wedge glass plate into the collimated beam before the scanner, generating a single, stable reference signal issuing from the wedge front surface. The beam deviation angle is  $2^\circ$  (geometrical wedge angle  $\theta \approx 3.1^\circ$ ). Such configuration can be seen as auto-collimation and the reference signal intensity is adjusted by slightly tilting the glass wedge. Collimation and focusing optics was chosen in order to achieve a Rayleigh range of  $1.3\text{mm}$  and a theoretical beam size on the sample of  $26.5\mu\text{m}$  ( $1/e^2$ -intensity).

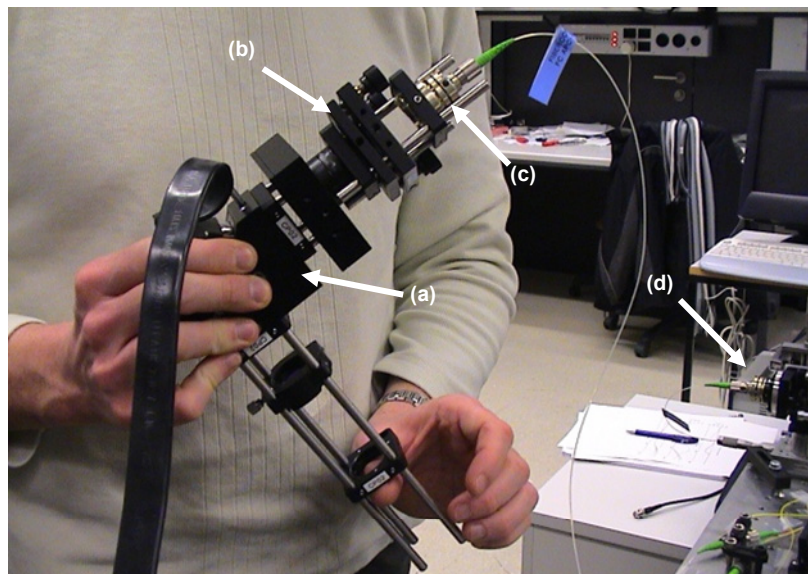


**Figure II-39.** Handheld probe with: (a) single mirror tip/tilt scanner, (b) glass wedge, (c) collimation optics with focal length  $f_1$ , (d) coupling from interferometer setup into fiber leading to handheld probe.

Attention has to be paid to the positioning of the beam with respect to the scanner pivot point since slight misalignment introduces undesired phase shifts during scanning. As a drawback of such a one point scanner one should mention the mechanical cross talk between the two orthogonal scanning axes which are driven by two pairs of electro-magnetic actuators. Since ideal orthogonality is impossible to achieve, slight cross talk may remain even with scanner-internal closed-loop regulation. This manifests as a slight oscillation in the slow scanning axis when the fast axis is snapping back while both axes are driven with a saw tooth function at

different frequencies. The effect increases with higher scan amplitudes but could certainly be decreased using a smaller and lighter mirror. As a matter of fact, this single mirror tip/tilt scanner was designed for high power laser applications [39] and presents a mirror surface of approx.  $40 \times 30 \text{ mm}$ . A picture of the realized, rather bulky handheld probe is shown in Figure II-39.

#### 5.4.2 Endoscope probe

In addition a rigid endoscope was designed and built. The requirements for this device were defined as follows:

- Simple, rigid design for use as esophagoscope or bronchoscope
- Angular scanning by rotation (lateral view)
- Adjustable focus position
- One single reference reflection in sample beam path

The resulting design is schematically shown in Figure II-40 with sectional drawings.

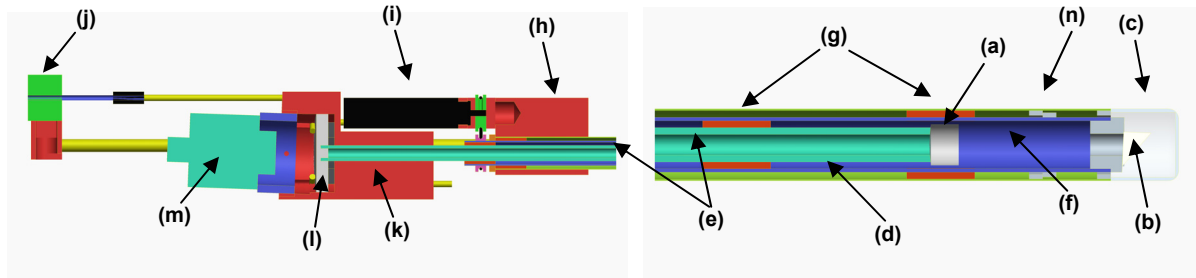


**Figure II-40. Sectional drawings of rigid esophagoscope design for use with dual beam heterodyne FDOCT. (lhs) Handle with reference reflector (l) and motor (i) for rotational scanning; (rhs) distal end with achromatic lens (a) and reflection prism (b). See text for details.**

The realized esophagoscope can be divided into a handle (see Figure II-40(lhs)) and a distal part (Figure II-40(rhs)). The distal part essentially consists of an achromatic lens (a) with focal length  $40 \text{ mm}$  and external diameter of  $6 \text{ mm}$  for focusing of the parallel beam, an uncoated right angle reflection micro prism (b) (Thorlabs) mounted with a slight tilt in order to achieve  $86^\circ$  deflection avoiding parasitic reflections, and a glass cap (c) cut from a Duran test tube for hermetic sealing. The glass cap was glued with biocompatible glue, resistant to disinfection and sterilization methods and acids within the human body, on top of the outer AISI 304 (Unimed) steel tube (d). Within this tube, two additional tubes (e,f) were mounted concentrically, spaced and guided by maintenance-free sliding bearings (g) with  $1 \text{ mm}$  wall thickness. Sliding bearings allow for axial displacement and rotation. The inner tube (e) serving as optical channel, the middle tube (f) has to rotate the mounted reflection prism (b). Placed in the mobile part of the handle (h), a DC motor with 16:1 reduction gear and optical encoder (i) (Maxon) rotates this middle tube (f) via a round belt (NBR o-ring) at nominal speeds from  $0.5$  to  $8.3 \text{ rps}$ . Since the motor is placed in the handle and not at the distal end of the endoscope, no power cable shadows the tomograms. A linear drive (j) (Nanotec) allows for axially displacing the reflection prism (b) via the middle tube (f), allowing for precisely adjusting the focus position radially without the necessity of re-adjusting the interferometric light source for optical path length compensation. The latter benefit is achieved by a fix position of the focusing lens (a) with respect to the handle (k), and a reference reflector generated at the second surface of an uncoated glass wedge (l) (with optical deviation angle of  $2^\circ$ ) mounted in the same part of the handle. The glass wedge is placed against a caoutchouc

disc allowing for slight tilt correction of the wedge in order to properly adjust the reference intensity. A beam collimator (m) (Schäfter & Kirchhoff) with focal length of  $8.1\text{mm}$  collimates the beam to a diameter of  $2\text{mm}$  propagating easily through the central tube (e) with inner diameter of  $3\text{mm}$ . In order to keep a stable position of the focus in depth, the middle (f) and outer tube (d) are axially blocked one against the other by means of brass discs (n). A picture of the custom-made esophagoscope is shown in Figure II-41.

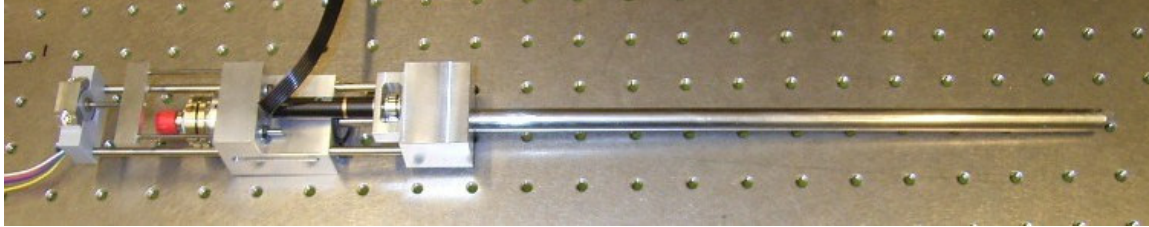


**Figure II-41.** Picture of designed and manufactured rigid esophagoscope with angular scanning according to sectional drawings shown in Figure II-40. Length of tube from handle until reflection prism is  $295\text{mm}$ . Typical length for rigid bronchoscopes is  $300\text{mm}$ .

## 5.5 Results and discussion

In order to demonstrate the advantage of dual beam versus standard FDOCT in terms of phase stability, the previously described three configurations were used (Figure II-38). For each configuration the  $SNR$  of the signal peak was adjusted to approximately  $26.5\text{dB}$ . The phase fluctuations at the signal peak position were measured while the system was unperturbed and perturbed respectively. The perturbation consisted in bending and moving the sample arm fiber guiding during measurement. The resulting standard deviations of the phase fluctuations  $\sigma_{\Delta\phi}$  are shown in Table II-8. The measured values are close to shot noise limited phase stability defined by the relation  $\sigma_{\Delta\phi} = (SNR)^{-1/2}$  [14]. For the perturbed case of the standard FDOCT configuration no clear value could be measured since the phase fluctuations are strongly varying (see Figure II-42).

	Without perturbation	With perturbation
Common path	$\sigma_{\Delta\phi} \approx 47.7\text{mrad}$	$\sigma_{\Delta\phi} \approx 48.8\text{mrad}$
Dual beam	$\sigma_{\Delta\phi} \approx 48.5\text{mrad}$	$\sigma_{\Delta\phi} \approx 51.2\text{mrad}$
Standard	$\sigma_{\Delta\phi} \approx 49.5\text{mrad}$	N.A.

**Table II-8.** Phase fluctuations for three different configurations with similar local  $SNR \approx 26.5\text{dB}$ .

The phase signals were extracted after FFT at the mean signal peak positions. By touching and bending the SM fiber, the signal of the standard setup is heavily perturbed, even resulting in up to  $100\mu\text{m}$  signal peak shift in depth. This displacement is caused by a change in optical path length due to a stress-induced change in refractive index. Both signal peaks were again adjusted to approximately the same  $SNR \approx 26.5\text{dB}$ . The strong fluctuations of the standard signal peak intensity are mainly due to fringe washout and stress-induced polarization state changes in the perturbed fiber, resulting in reduced interference fringe contrast. These measurements proof clearly the advantage of dual beam FDOCT over standard FDOCT for employing fiberized handheld applicators.



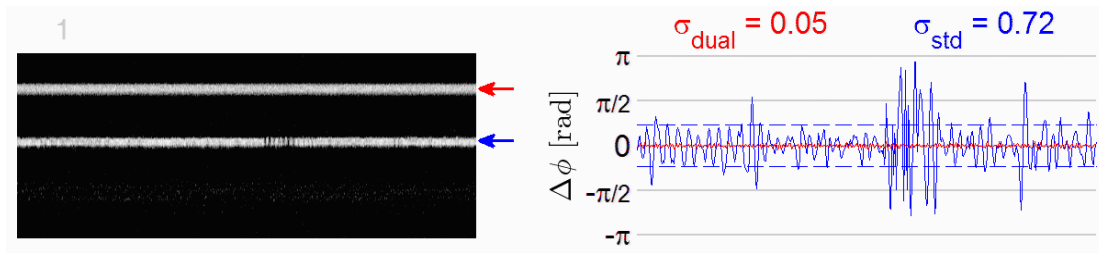


**Figure II-42.** (Movie: 2.2 MB) Time sequence of 500 depth scans per tomogram at same position, using the setup depicted in Fig. 4. The movie is shown at 5fps (7x reduced speed with respect to original acquisition rate). The dual beam signal (red) remains stable even if the fiber is perturbed whereas the signal peak corresponding to the standard setup (blue) is heavily perturbed. The dashed line indicates the standard deviation  $\sigma_{\text{std}}$  of the phase fluctuations over one tomogram. The shown tomogram depth is approximately  $400\mu\text{m}$  (in air),  $\text{SNR} \approx 26.5\text{dB}$ . Multimedia file is available at Optics Express at: <http://www.opticsexpress.org/browse.cfm?journal=4&strVol=15> (article in press, 2007).

In the following we demonstrate the feasibility of the introduced dual beam FDOCT principle to perform *in-vivo* imaging of human skin on the finger tip of a male subject. For this task we employed the fiberized handheld probe with a single mirror tip/tilt scanner (see §5.4.1). *In-vivo* measurements were conducted with a transverse over-sampling of approximately 12x and  $2 \times 1.1\text{mW}$  light power incident on the sample, thus sample and reference channel at same intensity for optimal  $\text{SNR}$  according to §5.2.3. The total distance  $\Delta z$  between reference and sample was  $200\text{mm}$  which had to be pre-compensated by adjusting  $\Delta z_{\text{ILS}}$  within the ILS. The recorded tomograms consist of 1100 depth scans each, covering a transverse range of  $2.5\text{mm}$ . The measurements had been performed by first adjusting the focal plane to the zero delay using a mirror and then placing the sample structure across this position.

The recorded signal was reconstructed following the differential complex scheme from §3.2.2 (see Figure II-43(c)). The dynamic range within the tomogram is about  $40\text{dB}$  with a system sensitivity of  $95\text{dB}$ . One observes that the DC term is strongly suppressed as compared to its original amplitude (directly after Fast Fourier Transform (FFT)). If we define the DC suppression ratio as  $DC_{\text{suppress}} \equiv DC_{2x2}/DC_{\text{FFT}}$ , with  $DC_{2x2}$  being the DC signal value in Figure II-43(c) and  $DC_{\text{FFT}}$  the one in Figure II-43(a) we have  $DC_{\text{suppress}} = -47\text{dB}$ . The fact that the DC term is not fully suppressed is explained by the presence of slight intensity fluctuations throughout the tomogram. These fluctuations were measured to be in the  $\text{kHz}$ -range with a standard deviation of 0.33%.

In Figure II-43 we compare the differential complex reconstruction technique (Equation (II.23)) (Figure II-43(c)) to the standard complex reconstruction based on two adjacent lines (Equation (II.4) in §3.2.1) with background correction (Figure II-43(d)). The background for the tomogram is obtained by averaging of all transversally recorded spectra. The brightness of the tomograms was adjusted by first normalizing the intensity to that of a common bright structure (sweat gland) and then setting the minimum of the intensity scale bar to the calculated noise floor. The maximum scale bar value is given by the highest intensity in the tomogram. This results in a linear gray scale spanning over a  $DR$  of  $28.5\text{dB}$  for standard complex reconstruction and  $31\text{dB}$  for the differential complex reconstruction. As expected, the  $\text{SNR}$  for the differential complex method is better by approximately  $+3\text{dB}$  as compared to the standard complex reconstruction. It can also be observed that DC suppression works slightly better for the differential complex approach (Figure II-43(c) and (d)).

The tomogram in Figure II-43(a) shows the measured data with standard reconstruction employing straight-forward FFT reconstruction. One can clearly see that the structure had

been measured across the zero delay due to the presence of mirror structures. Figure II-43(b) finally shows a standard reconstruction as in Figure II-43(a) but with background subtraction in post-processing. Again, a slight DC term remains together with sample structure obstructing mirror terms.

Investigating the mirror term suppression within different 2D tomograms for bright scattering structures, the suppression ratio can be measured to be better than  $-15\text{dB}$ . Higher over-sampling would increase the suppression ratio as one remains tighter within the speckle pattern [14].

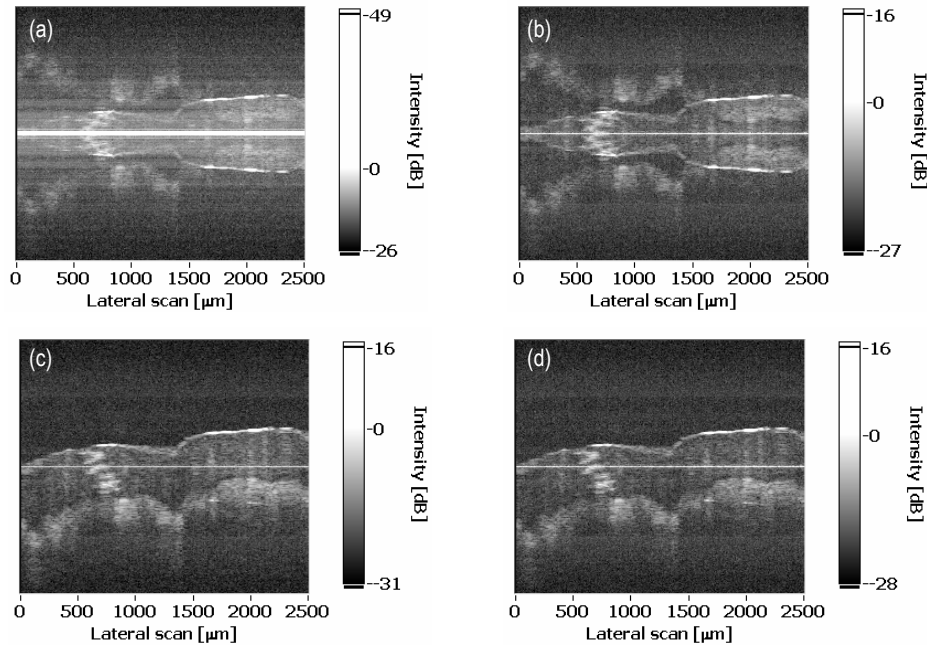


**Figure II-43.** Tomogram of human fingertip with sweat gland, slice from 3D stack of Figure II-44(a), indicated by red frame. (a) Direct FFT on measured data, (b) with background correction employing averaging before FFT, (c) differential complex reconstruction and (d) standard complex reconstruction with background correction. Frame size:  $2.5\text{mm}$  lateral  $\times$   $1.92\text{mm}$  depth, in air.

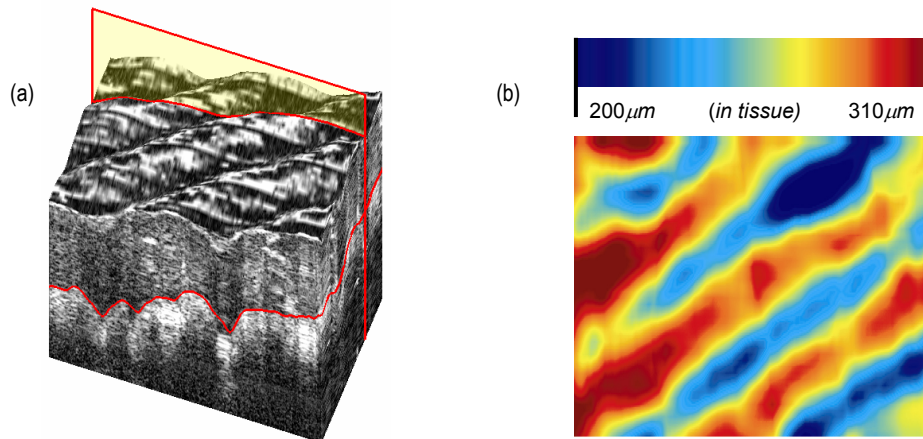


**Figure II-44.** (a) Tomogram of human finger tip (structure size:  $2.5\text{mm} \times 2\text{mm} \times \sim 1.1\text{mm}$ , in air) with the lower wavy red line delimiting the dermis-epidermis border and the red frame indicating the position of the 2D tomogram shown in Figure II-43. (b) Thickness map of epidermis in (a) (top view, size:  $2.5\text{mm} \times 2\text{mm}$ , corrected for  $n_{\text{tissue}}=1.34$ ).

Figure II-44(a) shows a 3D data set of a human finger tip, consisting of 66 2D tomograms and reconstructed using the differential complex scheme. The total recording time was 4.5s. By performing edge detection on each individual 2D tomogram, the user has access *e.g.* to a thickness map of the epidermis as illustrated in Figure II-44(b). The red frame in Figure II-44(a) indicates the position of the 2D tomograms presented in Figure II-43 within the 3D data cube. The rudimentary DC peak at the zero-delay, visible in Figure II-43(c), was removed from Figure II-44(a) by first setting it to zero and afterwards interpolating the intensities in post processing.

As second biological target porcine esophagus was imaged *ex vivo*, using the custom-made rigid esophagoscope described in §5.4.2. The focus was placed at 6mm from the rotation axis inside the imaged structure. The resulting circumference for one full rotation was 37.7mm and the theoretical spot size on the sample was  $26\mu\text{m}$  ( $1/e^2$ -intensity) with a Rayleigh range of 1.2mm. The path length difference between reference and sample was 400mm which was pre-compensated by adjusting  $\Delta z_{\text{ILS}}$  within the interferometric light source in order to place the zero-delay at the focus position. *In-vivo* measurements were conducted with  $2 \times 340\mu\text{W}$  light power incident on the sample.

The recorded  $360^\circ$  tomograms consist of 15'400 (Figure II-45) and 20'000 lines (Figure II-46) respectively. The structure was first reconstructed following the differential complex scheme from §5.2.2 and second mapped from Cartesian to radial coordinates using interpolation based on cubic B-splines (see Figure II-45 and Figure II-46). As mapping parameters for a  $360^\circ$  tomogram the focus position (6mm) and the selected tomogram depth (3mm) is needed (lhs of Figure II-45 and Figure II-46). For better visualization a second radial mapping with doubled depth (6mm, but for effectively selected 3mm) was performed, resulting in a “zoom-like” structure (rhs of Figure II-45 and Figure II-46). Mapping from Cartesian to radial coordinates resulted in an apparent dynamic range (DR) increase due to interpolation. DR within the  $360^\circ$  tomograms is measured to be between 26dB and 29dB with a system sensitivity of close to the zero-delay of approximately 89dB. Penetration depth was up to  $500\mu\text{m}$  (value in tissue). A zoomed region of interest (ROI) in Figure II-46(rhs) is shown in Figure II-47. With an increased incident power this rather small penetration depth and the low system sensitivity could be improved. Still, a double-layer structure is visible with some vascularization present in the second layer.

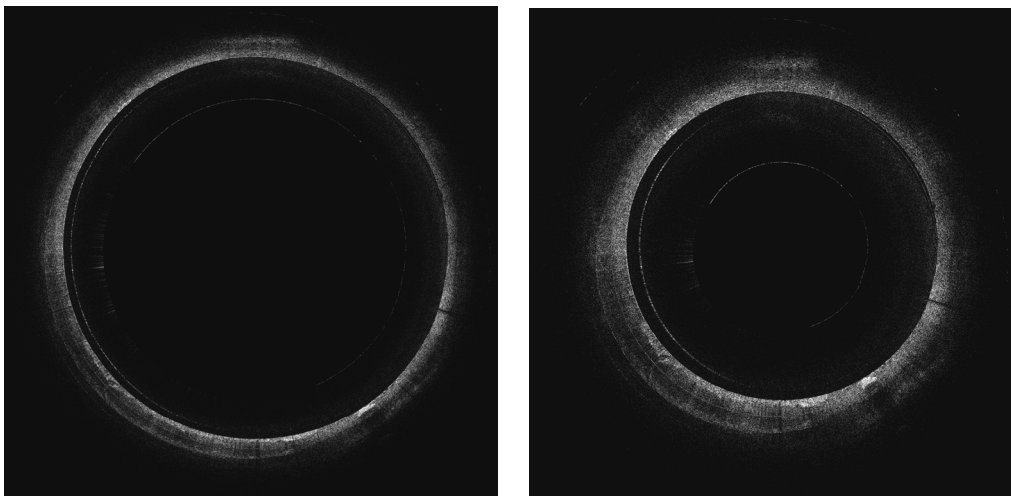


**Figure II-45.** Tomogram of porcine esophagus *ex vivo*, consisting of 15'400 lines with 10.5x over-sampling. Linear grayscale with 29.3dB (lhs) and 28.4dB (rhs) dynamic range, noise floor at 58.1dB. Sizes: (lhs) 15mm x 15mm in air, (rhs) radial structure depth scaled by factor of 2. Original DR before radial mapping: 27.6dB.



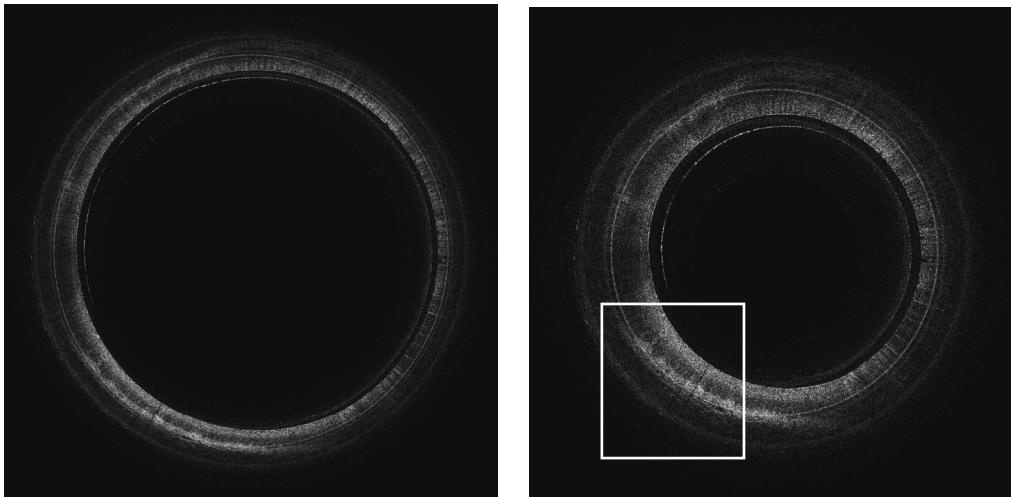


Figure II-46. Tomogram of porcine esophagus *ex vivo*, consisting of 20'000 lines with 13.6x over-sampling. Linear grayscale with 26.1dB (lhs) and 25.7dB (rhs) dynamic range, noise floor at 66.3dB. The CCD camera gain was set to +12dB. Sizes: (lhs) 15mm x 15mm in air, (rhs) radial structure depth scaled by factor of 2. Original DR before radial mapping: 24.4dB. ROI: see Figure II-47.

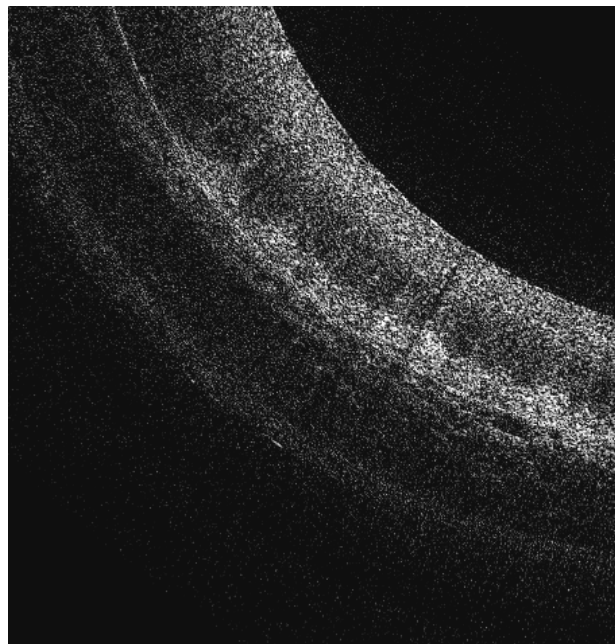


Figure II-47. ROI of Figure II-46(rhs). Circle-like residual mirror structures are visible in the lower left direction of the structure. Linear grayscale in [dB].

Following conclusions can be drawn from above endoscope tomograms:

- With approx. -15dB and better (measured in original tomogram before radial mapping), mirror term suppression sufficient for this DR
- Slight residual ghost images (echoes) due to polarization effects in the fiberized part of the interferometer

Even though the long relative distance from the reference reflector to the sample did not influence the phase stability considerably, shorter distances would be much more preferable. A quite promising modification would be the implementation of a diffractive optical element (DOE) focusing a certain fraction of light onto the exit surface of the reflection prism (which

would ideally be not exactly  $90^\circ$  in order to prevent parasite reflections). The main problem with such a diffractive element is the strong dependency of the focal length with respect to the wavelength. For a spectral range of  $\pm 100\text{nm}$  centered at  $800\text{nm}$  approximately  $\pm 10\%$  variation on the focal length has to be expected. In addition, diffraction efficiency will depend on wavelength as well. Both effects together would add up and severely limit the spectral bandwidth of the system. Therefore, broad bandwidth light sources would be difficult to be employed with a DOE, challenging of course the principle reason for achromatic complex FDOCT based on acousto-optic frequency shifters.

The demonstrated principle can easily be adapted for common path ophthalmic imaging. In particular the phase stability can be enhanced by using actually a sample reflection such as at the cornea front surface as reference. This could be achieved again using a DOE focusing a certain fraction of light onto the cornea (with the same limitations as discussed above). Such an approach was already proposed by Baumgartner *et al.* [40] and Möller *et al.* [41] for time domain OCT. Attention has to be paid to the resulting Rayleigh range of the focused beam fraction since the Rayleigh range has to support proband motion. For a collimated beam with  $2\text{mm}$  diameter ( $1/e^2$ -intensity)  $60\text{mm}$  focal length would be a good value. The advantage of such a system would be that one could achieve complete axial proband motion suppression which is especially interesting for functional imaging extensions such as Doppler FDOCT [42-45]. Still, using dual beam FDOCT in conjunction with illumination power limited applications such as in ophthalmology one would have a  $-6\text{dB}$  sensitivity disadvantage which cannot be compensated by simply increasing illumination power.

Finally, one should mention that the principle of dual-beam heterodyne FDOCT can equally be used for swept source FDOCT. The latter would have the advantage of larger dynamic range, as well as the high depth-scan rates of modern swept-sources.

## 5.6 Conclusion

In this chapter dual beam FDOCT was introduced, allowing for phase sensitive measurements even through long probing fibers and employing applicators. A detailed theoretical analysis of the sensitivity and the dynamic range capabilities of a dual beam configuration was presented showing a  $-6\text{dB}$  disadvantage in sensitivity with an equal dynamic range as compared to standard FDOCT. Even though the dual beam concept is suitable for swept source and spectrometer-based FDOCT equally, it was tested on latter method employing two different applicators with a single mirror tip/tilt scanner performing *in-vivo* measurements on human skin and a custom-made esophagoscope performing *ex-vivo* measurements on porcine esophagus. The measurements showed results consistent with theory.

## Chapter 6

### Phase stability

#### 6.1 Theory

In Chapters 3 and 5 we discussed the importance of phase stability for the complex signal reconstruction. Experimental results on biological samples showed that the complex signal are reconstructed using the reconstruction formula given in Equation (II.4) in Chapter 3:

$$\tilde{I}(k) = I(k, t_0) - jI\left(k, t_0 + \frac{\pi/2}{\Omega}\right). \quad (\text{II.33})$$

Equation (II.5) in Chapter 3, describing the differential complex signal reconstruction, is basically an extension of Equation (II.33) to compensate for DC signal and coherent noise. However, in this chapter we will not need DC and coherent noise removal and therefore following tomograms will be reconstructed using Equation (II.33) if not otherwise indicated.

The essential step for reconstructing the tomographic data is the fast Fourier transform (FFT). FFT is a linear transformation, linking the frequency space  $k$  to the relative depth coordinate  $\Delta z$ . The FFT algorithm is a discrete transformation resulting in an equal number of bins corresponding to positive and negative frequencies. To each bin after FFT a cosine function with a certain frequency can be attributed (depth coordinate). Such a bin consists of a value for the amplitude and the phase of this cosine function, together describing a complex phasor  $V$ . For one pair of bins (e.g. bins  $N_0$  and  $-N_0$ ) the amplitude of the phasor  $V$  is identical, but its argument will be opposite. The FFT allows analyzing phase stability issues either on the spectral or the complex phasor level, obviously with the same result. It follows that the complex signal can be reconstructed on a spectral level (as it was performed in Chapters 3 and 5) or after FFT with the complex phasors (see Figure II-48).

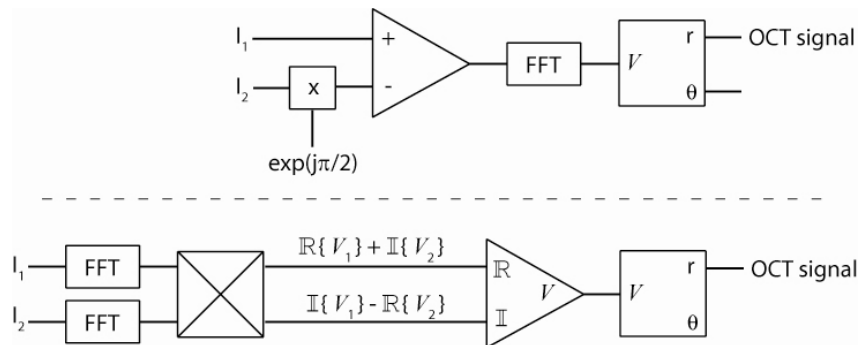


**Figure II-48. Complex signal reconstruction before or after FFT with equivalent result.**

Equations (II.1) and (II.2) (Chapter 3) describe the signal as detected by the spectrometer. It is the real-valued part of a complex signal, the superposition of reference ( $E_R$ ) and sample ( $E_S$ ) electromagnetic field. Figure II-49 depicts a graphical representation of a single reflecting surface as a sample (without DC), resulting in one cosine function spread over the whole detector array. Any phase or amplitude error of the complex field vector  $E_R E_S^*$  will result in a detected intensity error. The detected amplitude error on the spectrometer can also be considered as a phase error.

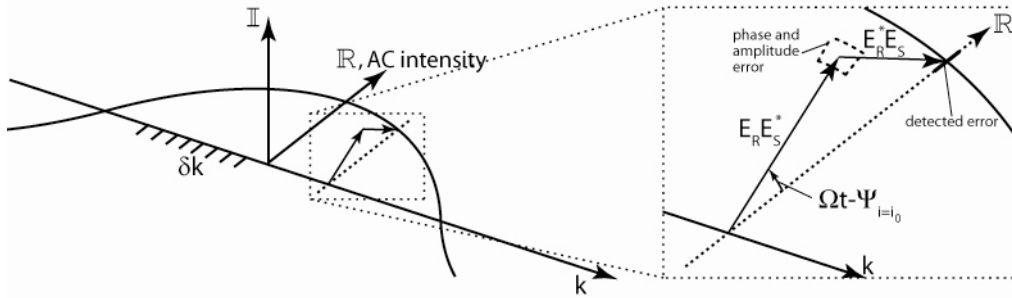


**Figure II-49. Cosine modulation on spectrometer representing one reflecting sample surface, without DC term. Phase and amplitude errors of the complex electromagnetic reference and sample fields result in detected phase and amplitude errors.**

After FFT this single cosine modulation will result in two complex vectors  $V_1$  and  $V_1^*$ , its complex conjugate (see Figure II-50). They represent the positive and negative frequency respectively. Each bin after FFT therefore carries a complex phasor, in the case of heterodyne FDOCT with the argument  $\Omega t - \Psi_i$ . After a quarter period of the beating signal, the phasor rotated by  $\pi/2$  ( $V_2$ ) and  $-\pi/2$  ( $V_2^*$ ) respectively. This second acquisition is useful for eliminating complex ambiguity. However, the same second phasor is responsible for imperfect complex signal reconstruction as it is a relative measurement which should match a  $\pi/2$  phase shift as best as possible. If the second phasor resulting from the second acquisition adds some amplitude and/or phase errors, the complex signal reconstruction will bear these error contributions and mirror terms will still be visible.

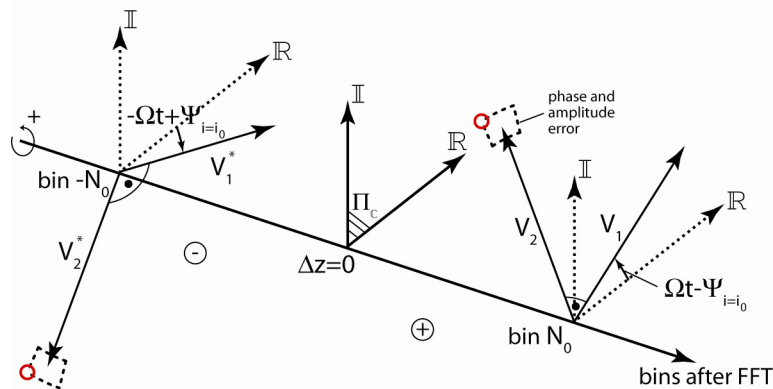


**Figure II-50. Complex phasors after FFT of a cosine function, representing a positive (bin  $N_0$ ) and negative frequency (bin  $-N_0$ ). The phasor pair rotates within its respectively attributed complex plane in opposite directions.**

Figure II-51 is equivalent to Figure II-50 but represented as two separate 2D graphs. The complex signal reconstruction mixes the information of a second acquisition ( $I_2$ ) in order to reconstruct the complex value of a first acquisition ( $I_1$ ). Mirror terms are suppressed if the complex phasors  $V_1$  and  $-jV_2$  ( $V_2$  rotated by  $-90^\circ$ ) add up in the same direction (rhs of Figure II-51) and cancel out by summation (lhs of Figure II-51). An error indicated by the red circle

will result in a residual vector at the mirror position and the ratio of their norm values will define the degree of mirror term suppression.

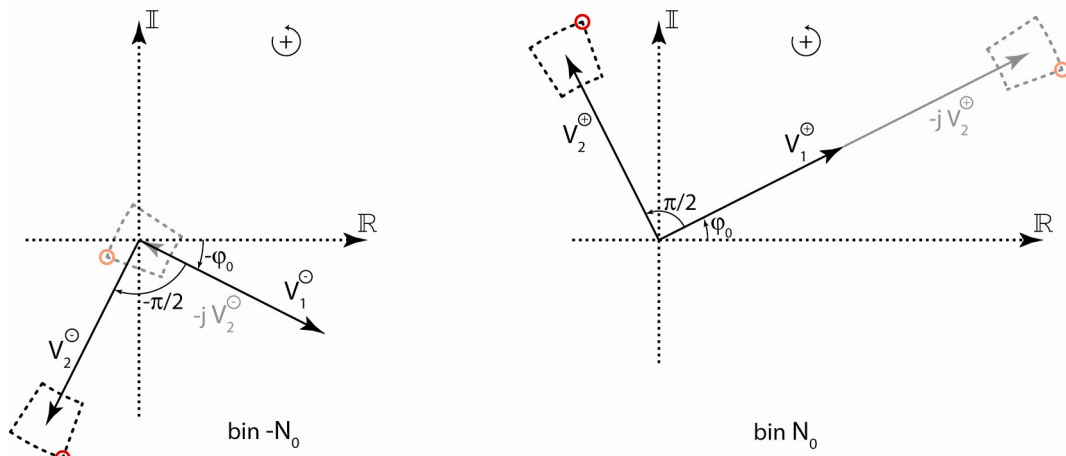


**Figure II-51. Complex phasors from Figure II-50 in 2D for two conjugated Fourier bins after FFT.**

Without loss of generality normalized vectors and  $\varphi_0=0$  can be considered. The position in the complex plane of the slightly transparent red circle (see Figure II-51) for Fourier bin  $-N_0$  and bin  $N_0$  in this case can be expressed as follows:

$$\begin{array}{cc} \text{bin } -N_0 & \text{bin } N_0 \\ \mathcal{R} = 1 - (1+q)\cos(\Delta\varphi_{err}) & \mathcal{R} = 1 + (1+q)\cos(\Delta\varphi_{err}), \\ \mathcal{I} = (1+q)\sin(\Delta\varphi_{err}) & \mathcal{I} = (1+q)\sin(\Delta\varphi_{err}) \end{array} \quad (\text{II.34})$$

with  $q$  as the relative amplitude error being defined as  $q = \Delta A / |V_1^{\oplus}|$  and  $\Delta\varphi$  the phase error with respect to the desired  $90^\circ$  phase shift. The mirror term suppression ratio (MTSR) (see also Figure II-2 and Figure II-3) therefore results in:

$$\begin{aligned} \frac{P^*}{P} [dB] &= 10 \log \left( \frac{[1 - (1+q)\cos(\Delta\varphi_{err})]^2 + [(1+q)\sin(\Delta\varphi_{err})]^2}{[1 + (1+q)\cos(\Delta\varphi_{err})]^2 + [(1+q)\sin(\Delta\varphi_{err})]^2} \right) = \\ &= 10 \log \left( \frac{q^2 + 2(1+q)(1 - \cos(\Delta\varphi_{err}))}{q^2 + 2(1+q)(1 + \cos(\Delta\varphi_{err}))} \right) \end{aligned} \quad (\text{II.35})$$

For  $q = \Delta\varphi_{err}=0$  the suppression ratio is perfect, as expected. Setting  $q=0$ , i.e. no amplitude errors but only phase errors, Equation (II.35) becomes:

$$\underbrace{\frac{P^*}{P} [dB]}_{\text{phase error}} = 10 \log \left( \tan^2 \left( \frac{\Delta\varphi_{err}}{2} \right) \right). \quad (\text{II.36})$$

Next, this analytical result is compared to measurements in the following paragraph. It represents the central vertical line in Figure II-52 where the MTSR is plotted as function of phase and amplitude error. As shown, phase errors of approximately  $\pm 4^\circ$  or relative amplitude errors between the two phasors of approximately  $+8\%$  and  $-7\%$  are acceptable to still have MTSR of  $-30dB$ . For pure phase error (vertical dotted line) the plot shows perfectly symmetric behavior whereas for amplitude errors it is slightly asymmetric.

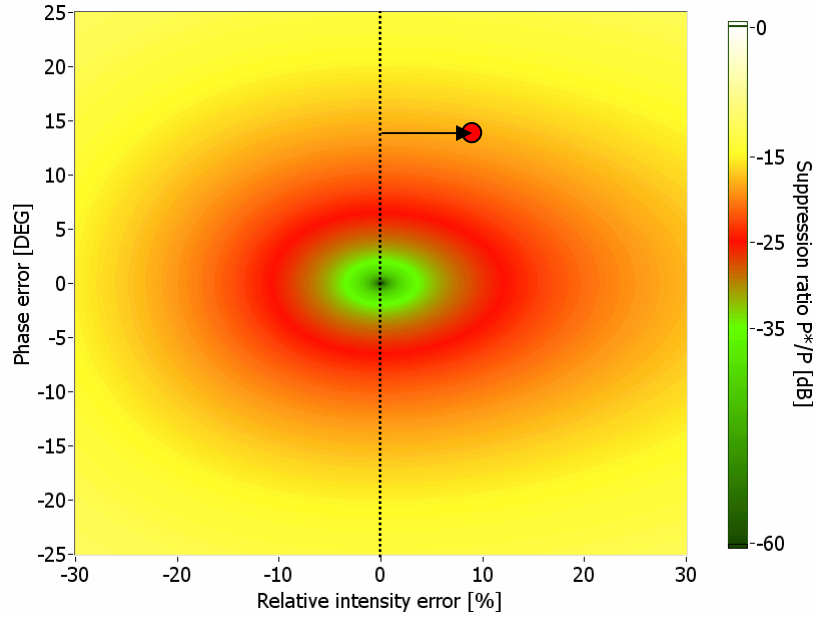


**Figure II-52. Mirror term suppression ratio (MTSR) as function of relative amplitude errors and phase errors with respect to the desired 90° phase shift between two successive acquisitions.**

According to Park *et al.* [14], the overall phase error standard deviation  $\sigma_{\Delta\phi_{err}}$  can be expressed as  $\sigma_{\Delta\phi_{err}} = \sqrt{\sigma_{\Delta\phi}^2 + \sigma_{\Delta x}^2}$  with:

$$\sigma_{\Delta\phi} = \frac{1}{\sqrt{SNR}} \quad \text{and} \quad \sigma_{\Delta x} = \sqrt{\frac{4\pi}{3} \left( 1 - \exp \left( -2 \left( \frac{\Delta x}{2w_0} \right)^2 \right) \right)}, \quad (\text{II.37})$$

where  $\sigma_{\Delta\phi}$  is a fundamental, shot-noise limited value and  $\sigma_{\Delta x}$  is the phase error due to scanning for a uniformly scattering sample.  $\Delta x$  is the step width between two acquired lines and  $2w_0$  is the  $1/e^2$ -intensity beam width at the beam focus.

## 6.2 Experimental

In order to validate this model, first a reflecting sample was measured during a short time period. We used the heterodyne FDOCT system with precise 90° phase shift between two successive acquisitions. The probing beam was fixed, but slight perturbations have been induced (*i.e.* vibrations of the optical setup). This resulted in phase errors (with respect to the 90° phase shift) but negligible amplitude errors. The resulting tomogram, showing fluctuating mirror term intensities, is presented in Figure II-53.

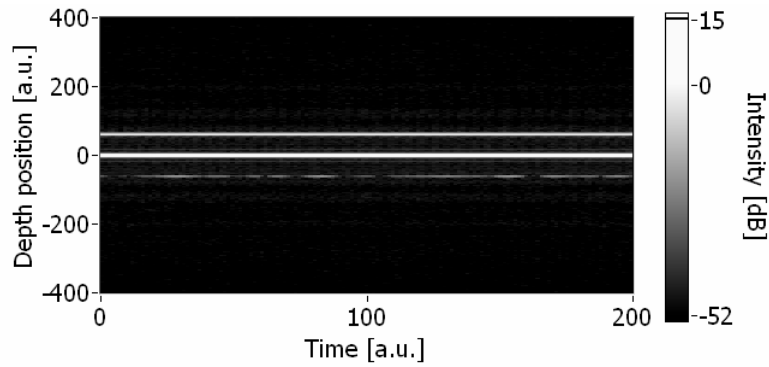


**Figure II-53. Complex reconstructed tomogram of mirror surface with induced phase errors. Mirror terms are not sufficiently suppressed and appear. DC is at zero position.**

A time trace along the signal peak shows relative amplitude errors  $q$  with a standard deviation  $\sigma_q$  of 0.006 (see Figure II-54(lhs)) and phase errors  $\Delta\varphi_{err}$  with  $\sigma_{\Delta\varphi_{err}} = 8^\circ$  (Figure II-54(rhs)).

Plotting the MTSR as function of phase error (black squares in Figure II-55), one exactly matches the theoretically calculated curve (Equation (II.36)) indicated as red line. The result is shown in Figure II-55.

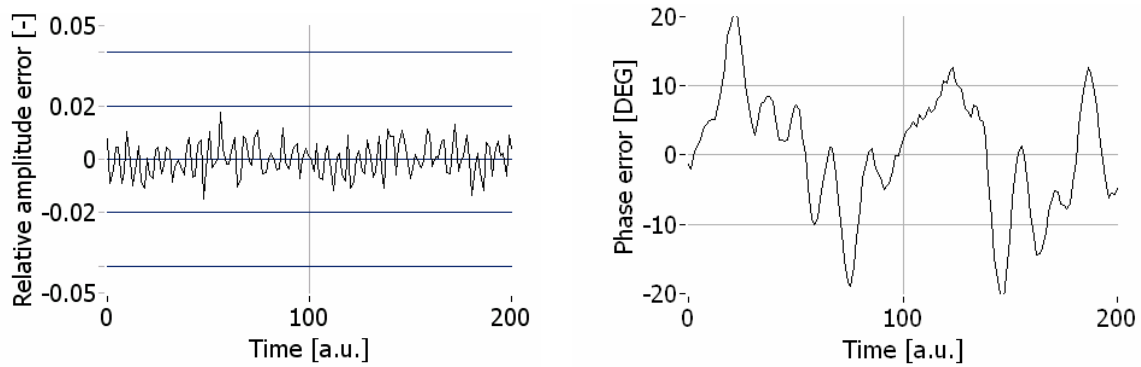


**Figure II-54. (lhs) Relative amplitude errors are small on a reflecting surface. (rhs) Phase errors cause insufficient mirror term suppression. See text for details.**

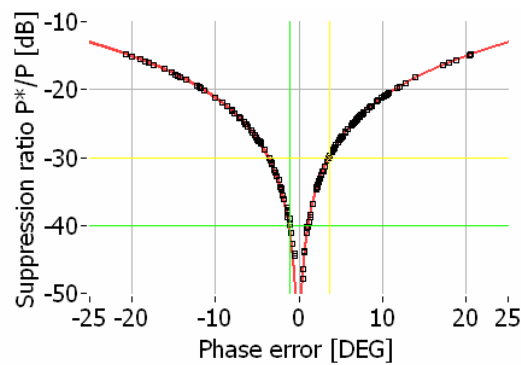


**Figure II-55. Mirror term suppression ratio of tomogram shown in Figure II-53 with fluctuating phase shift. Black squares: measured signal, red curve: plot of Equation (II.36). Yellow and green coordinate lines represent -30dB and -40dB suppression, corresponding to a phase error of  $\pm 3.6^\circ$  and  $\pm 1.2^\circ$  respectively. Without any perturbation the system performance limit is -50dB, thus  $\pm 0.4^\circ$  (standard deviation value).**

Performing a similar experiment on a diffusive sample like paper, while the beam is scanned at a constant speed, Figure II-56 results after complex reconstruction. Figure II-57 shows for

this case relative amplitude variations  $q$  and phase errors  $\Delta\varphi_{err}$ . For this analysis the maximum signal in depth was selected which varies slightly around bin number 100 approx. (see Figure II-56). The strong amplitude fluctuations ( $\sigma_q=0.09$ ) are caused by speckle effects. The phase errors  $\Delta\varphi_{err}$  are  $\sigma_{\Delta\varphi_{err}} = 7.4^\circ$ . The mean value of  $-12^\circ$  results from a large beam offset with respect to the scanner pivot axis and performing a unidirectional scan (sawtooth).

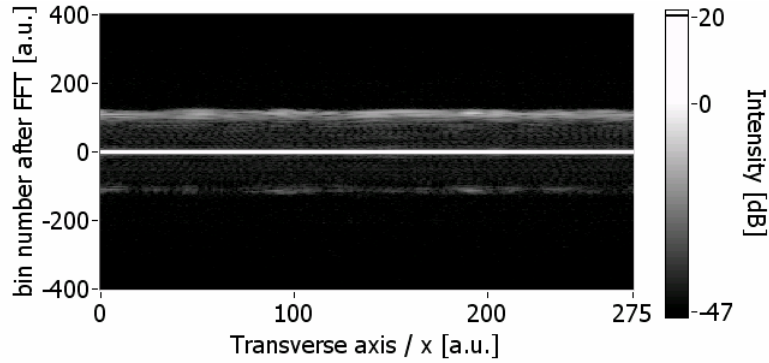


**Figure II-56. Complex reconstructed tomogram of a piece of paper. Phase errors are induced by fast scanning. Mirror terms are not sufficiently suppressed and become visible. DC at zero position.**

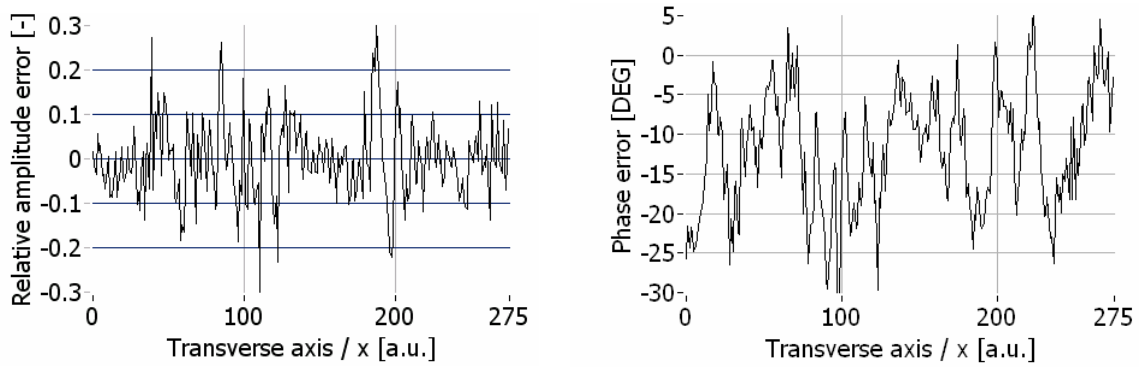


**Figure II-57. Important relative amplitude (lhs) and phase errors (rhs). Fluctuations are more chaotic than for the reflecting surface. See text for details.**

By plotting the MTSR, the relation issued from Equation (II.36) represents an inferior limit (see Figure II-58(lhs)). This result is as expected from Equation (II.35) and Figure II-52. For a given phase error, adding relative amplitude error, the complex signal is reconstructed with lower accuracy and mirror terms are less suppressed. Therefore we conclude that for complex signal reconstruction not only phase errors but also amplitude errors are of significant importance. Especially in scattering samples, subject to speckle generation, amplitude errors add up with pure phase errors and corrupt complex signal reconstruction additionally (see arrow in Figure II-52). This important conclusion suggests criteria for optimized reconstruction algorithms, equally insensitive to amplitude and phase errors.

This amplitude error insensitivity can be achieved by synthesizing the second phasor with its phase, but the module of the first acquisition; *i.e.* the amplitude for two successive phasors are imposed to be identical. This reconstruction technique results again in a tomogram with mirror terms, but the suppression ratio again fits perfectly the calculations from Equation (II.35) (see Figure II-58(rhs)).



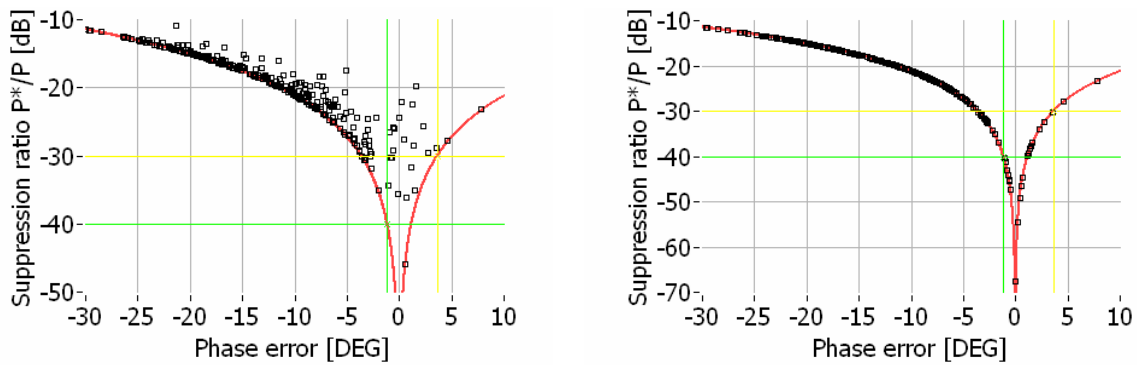


**Figure II-58. (lhs) Mirror terms suppression ratio in accordance to measurements shown in Figure II-57. The calculated curve for induced phase errors (red curve) represents an inferior limitation. Additional amplitude errors corrupt the complex reconstruction additionally. Black squares: measured values. (rhs) Same data as for (lhs) but with amplitude correction of second complex phasor. The measurements again fit perfectly to the calculated phase error curve.**

Recently a reconstruction algorithm using Hilbert transform prior to Fourier transform was proposed independently by Yasuno *et al.* [46] and Wang [47]. The algorithm applies the Hilbert transform to each spectral channel over the whole time range of one 2D tomogram, prior to Fourier transform. With this approach, theoretically, exact  $90^\circ$  copies of the spectra are calculated and extend the signal in the imaginary part. Especially Wang's solution is similar to what we were using throughout Part II. The advantage of his algorithm is that it does not need exact  $90^\circ$  phase shifts but some kind of carrier frequency or mean phase shift is sufficient. This phase shift, however, is important since  $\Delta\varphi > 0$  or  $\Delta\varphi < 0$  over the whole time range in order to not violate the Bedrosian theorem [48]. Otherwise the Hilbert transform will not necessarily represent its quadrature signal [47]. Therefore, acousto-optic frequency shifters prove to be ideal devices as they produce a unidirectional phase shift (or carrier frequency) with a large flexibility in the choice of carrier frequency. A different way to achieve unidirectional phase shift is the use of a piezo-actuator driven by a sawtooth wave form with relatively high amplitude synchronized to the fast scanning axis [47]. Figure II-59 shows the same tomogram data as Figure II-56, reconstructed using the Wang-algorithm [47], as consequence mirror terms are sufficiently well suppressed.

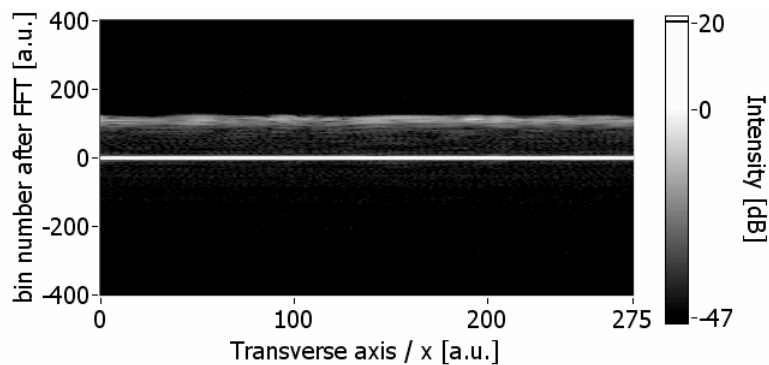


**Figure II-59. Tomogram showing same data as Figure II-56 but using the reconstruction algorithm proposed by Wang [47].**

Plotting the MTSR versus phase error with respect to a  $90^\circ$  phase shift, the measurement including the Wang-reconstruction is not in accordance with the theory from §6.1 anymore (see Figure II-60(lhs)), indicating an improvement compared to the reconstruction algorithm given in Equation (II.33).

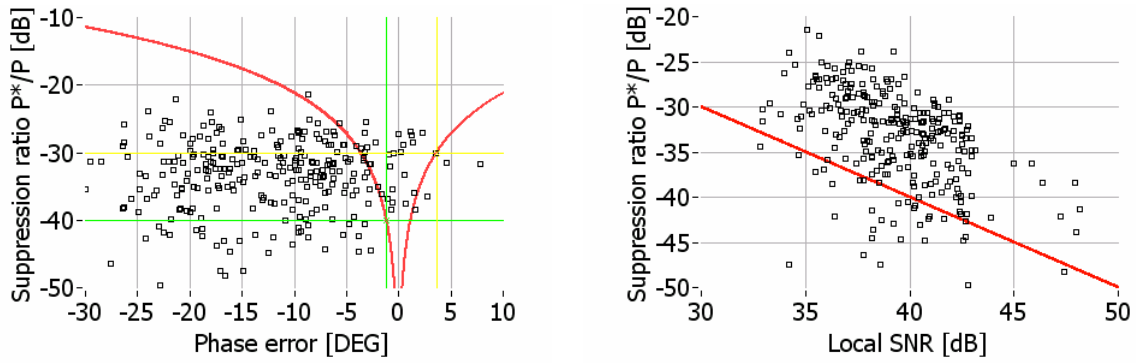


**Figure II-60. (lhs) Mirror terms suppression ratio for tomogram reconstructed using Wang's algorithm. For comparison the red curve represents the reconstruction performance based on the standard complex reconstruction scheme (for pure phase errors). (rhs) Suppression ratio versus local SNR (same data as lhs)). The red line indicates the ideal suppression ratio, where any mirror signal would be attenuation to the noise floor within the tomogram and hence would not be visible anymore.**

Analyzing the same data points as plotted in Figure II-60(lhs) by accounting for the local *SNR*, where the noise level was determined by measuring the mean value (in linear scale) of the dark region above the signal, the MTSR improves with increasing *SNR* (see Figure II-60(rhs)). This is, however, necessary since stronger signal needs a higher MTSR. The red line in Figure II-60(rhs) shows the theoretically ideal suppression ratio, where mirror terms are suppressed down to the noise level. The logarithmic difference between the black points and the red line presents a mean value of  $+5.9\text{dB}$  with a standard deviation of  $4.78\text{dB}$ .

Finally a short performance comparison of Wang's reconstruction scheme with the complex (§3.2.1, Equation (II.33)) and differential complex reconstruction algorithm (§3.2.2) will be given: Figure II-61(a-c) show data measured in the same series as the ones shown in Figure II-8 and Figure II-9. However, in this case, data sets with more significant phase errors with respect to the desired  $90^\circ$  phase relation had been chosen. In Figure II-61(a) standard complex reconstruction was performed. Figure II-61(b) shows differential complex reconstruction with a slightly increased dynamic range. Both tomograms show mirror terms clearly appearing at the fingernail fold region. Mirror structures are less apparent in the bottom right corner of the tomograms since they are superimposed with (weak) structure terms. Using the reconstruction algorithm proposed by Wang [47], Figure II-61(c) results. Mirror terms are better suppressed but do not vanish completely. This is in agreement with observations from Figure II-60(rhs). In Figure II-61(d), finally, the difference in mirror term suppression of Wang's reconstruction algorithm with respect to the standard complex reconstruction scheme is shown. As seen in the tomogram the relatively strong mirror term at the fingernail fold region is significantly better suppression with a Hilbert transform prior to FFT.

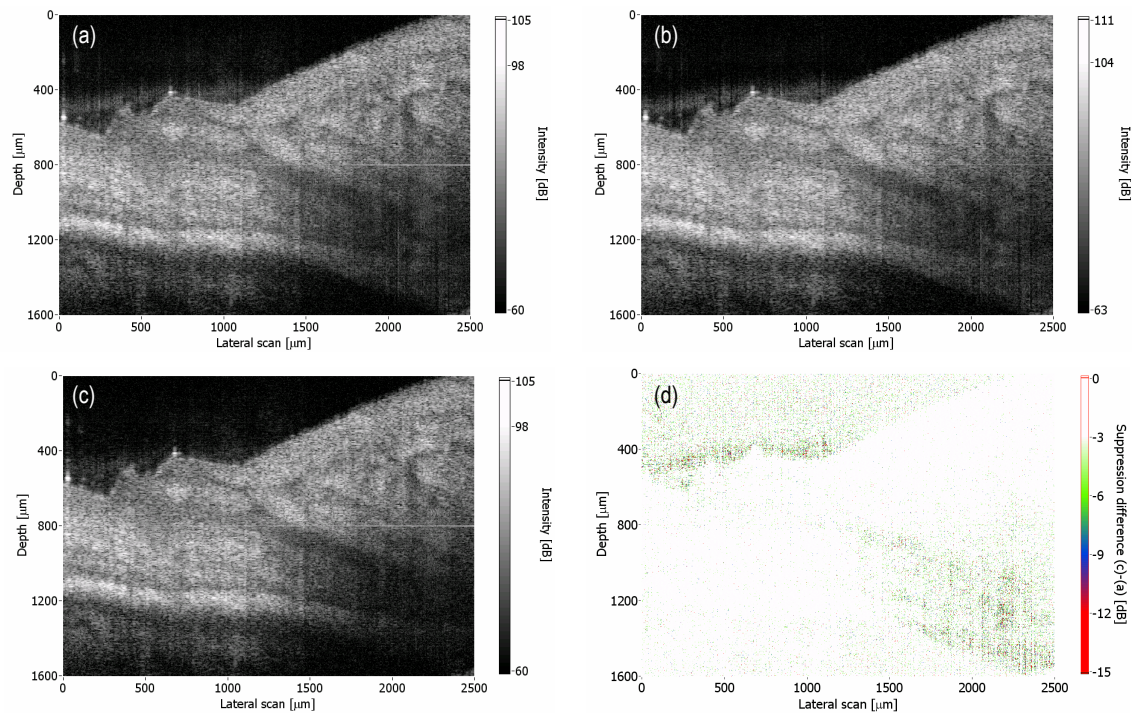


**Figure II-61. Tomogram using (a): complex reconstruction in accordance to Equation (II.4); (b): differential complex reconstruction scheme (Equation (II.5)); (c): Wang's reconstruction algorithm. (d) Suppression difference (c)-(a), revealing improved mirror term suppression using Hilbert transform prior to Fourier transform. See text for details. Depth axis: in air. Same measurement parameters as for Figure II-8 and Figure II-9.**

### 6.3 Conclusion

In this chapter phase stability issues were discussed in conjunction with the complex signal reconstruction scheme we have been using throughout Chapters 3 and 5. It was shown that amplitude errors influence the tomogram reconstruction significantly regarding the mirror term suppression ratio. Furthermore, a recently published reconstruction concept was tested and compared to our reconstruction scheme. This reconstruction algorithm showed improved performance but also undeniable limitations; it is certainly a step forward in the right direction, but still not the end point for best complex signal reconstruction.

#### References

1. A. F. Fercher, R. Leitgeb, C. K. Hitzenberger, H. Sattmann, and M. Wojtkowski, "Complex spectral interferometry OCT," in *Medical Applications Of Lasers In Dermatology, Cardiology, Ophthalmology, And Dentistry II, Proceedings* (1999), pp. 173-178.
2. M. Wojtkowski, A. Kowalczyk, R. Leitgeb, and A. F. Fercher, "Full range complex spectral optical coherence tomography technique in eye imaging," *Opt. Lett.* **27**, 1415-1417 (2002).
3. J. Schmit, and K. Creath, "Extended Averaging Technique for Derivation of Error-Compensating Algorithms in Phase-Shifting Interferometry," *Applied Optics* **34**, 3610-3619 (1995).
4. P. Targowski, M. Wojtkowski, A. Kowalczyk, T. Bajraszewski, M. Szkulmowski, and W. Gorczynska, "Complex spectral OCT in human eye imaging in vivo," *Opt. Commun.* **229**, 79-84 (2004).
5. Y. Yasuno, S. Makita, T. Endo, G. Aoki, H. Sumimura, M. Itoh, and T. Yatagai, "One-shot-phase-shifting Fourier domain optical coherence tomography by reference wavefront tilting," *Opt. Express* **12**, 6184-6191 (2004).
6. R. A. Leitgeb, C. K. Hitzenberger, A. F. Fercher, and T. Bajraszewski, "Phase-shifting algorithm to achieve high-speed long-depth-range probing by frequency-domain optical coherence tomography," *Opt. Lett.* **28**, 2201-2203 (2003).

7. E. Gotzinger, M. Pircher, R. A. Leitgeb, and C. K. Hitzenberger, "High speed full range complex spectral domain optical coherence tomography," *Opt. Express* **13**, 583-594 (2005).
8. M. A. Choma, C. Yang, and J. A. Izatt, "Instantaneous quadrature low-coherence interferometry with  $3 \times 3$  fiber-optic couplers," *Opt. Lett.* **28**, 2162-2164 (2003).
9. S. H. Yun, G. J. Tearney, J. F. de Boer, and B. E. Bouma, "Removing the depth-degeneracy in optical frequency domain imaging with frequency shifting," *Opt. Express* **12**, 4822-4828 (2004).
10. A. M. Davis, M. A. Choma, and J. A. Izatt, "Heterodyne swept-source optical coherence tomography for complete complex conjugate ambiguity removal," *J. Biomed. Opt.* **10** (2005).
11. S. H. Yun, G. J. Tearney, J. F. de Boer, and B. E. Bouma, "Motion artifacts in optical coherence tomography with frequency-domain ranging," *Opt. Express* **12**, 2977-2998 (2004).
12. R. Leitgeb, C. K. Hitzenberger, and A. F. Fercher, "Performance of fourier domain vs. time domain optical coherence tomography," *Opt. Express* **11**, 889-894 (2003).
13. M. Wojtkowski, R. Leitgeb, A. Kowalczyk, T. Bajraszewski, and A. F. Fercher, "In vivo human retinal imaging by Fourier domain optical coherence tomography," *J. Biomed. Opt.* **7**, 457-463 (2002).
14. B. H. Park, M. C. Pierce, B. Cense, S. H. Yun, M. Mujat, G. J. Tearney, B. E. Bouma, and J. F. de Boer, "Real-time fiber-based multi-functional spectral-domain optical coherence tomography at  $1.3 \mu\text{m}$ ," *Opt. Express* **13**, 3931-3944 (2005).
15. Y. C. Chen, X. M. Liu, M. J. Cobb, M. T. Myaing, T. Sun, and X. D. Li, "Optimization of optical spectral throughput of acousto-optic modulators for high-speed optical coherence tomography," *Opt. Express* **13**, 7816-7822 (2005).
16. Y. Chen, and X. Li, "Dispersion management up to the third order for real-time optical coherence tomography involving a phase or frequency modulator," *Opt. Express* **12**, 5968-5978 (2004).
17. T. Xie, Z. Wang, and Y. Pan, "High-speed optical coherence tomography using fiberoptic acousto-optic phase modulation," *Opt. Express* **11**, 3210-3219 (2003).
18. M. Pircher, E. Goetzinger, R. Leitgeb, and C. K. Hitzenberger, "Three dimensional polarization sensitive OCT of human skin in vivo," *Opt. Express* **12**, 3236-3244 (2004).
19. B. E. A. Saleh, and M. C. Teich, *Fundamentals of Photonics* (John Wiley & Sons, Inc., New York, 1991).
20. M. Bass, *Handbook of Optics, Volume 2* (McGraw-Hill, 1995).
21. A. K. Ghatak, *Optical electronics* (Cambridge University Press, 1989).
22. A. Korpel, *Acousto-optics* (Marcel Dekker, Inc., 1997).
23. J. Xu, and R. Stroud, *Acousto-optic devices - Principles, design and applications* (John Wiley & Sons, Inc., 1992).
24. A. Tchernyatin, E. Blomme, and V. Voloshinov, "Mixed isotropic-anisotropic Bragg diffraction in crystals," *Journal of Optics A: Pure and Applied Optics* **4**, 16-22 (2002).
25. D. L. Franzen, and R. Srivastava, "DETERMINING THE MODE-FIELD DIAMETER OF SINGLE-MODE OPTICAL FIBER: AN INTERLABORATORY COMPARISON," *Journal of Lightwave Technology* **LT-3**, 1073-1077 (1985).
26. A. H. Bachmann, R. A. Leitgeb, and T. Lasser, "Heterodyne Fourier domain optical coherence tomography for full range probing with high axial resolution," *Opt. Express* **14**, 1487-1496 (2006).
27. J. Zhang, J. S. Nelson, and Z. P. Chen, "Removal of a mirror image and enhancement of the signal-to-noise ratio in Fourier-domain optical coherence tomography using an electro-optic phase modulator," *Opt. Lett.* **30**, 147-149 (2005).
28. M. A. Choma, A. K. Ellerbee, C. H. Yang, T. L. Creazzo, and J. A. Izatt, "Spectral-domain phase microscopy," *Opt. Lett.* **30**, 1162-1164 (2005).
29. M. V. Sarunic, S. Weinberg, and J. A. Izatt, "Full-field swept-source phase microscopy," *Opt. Lett.* **31**, 1462-1464 (2006).
30. C. Joo, T. Akkin, B. Cense, B. H. Park, and J. F. De Boer, "Spectral-domain optical coherence phase microscopy for quantitative phase-contrast imaging," *Opt. Lett.* **30**, 2131-2133 (2005).
31. C. Joo, K. H. Kim, and J. F. De Boer, "Spectral-domain optical coherence phase and multiphoton microscopy," *Opt. Lett.* **32**, 623-625 (2007).
32. D. C. Adler, R. Huber, and J. G. Fujimoto, "Phase-sensitive optical coherence tomography at up to 370,000 lines per second using buffered Fourier domain mode-locked lasers," *Opt. Lett.* **32**, 626-628 (2007).
33. A. R. Tumlinson, J. K. Barton, B. Povazay, H. Sattman, A. Unterhuber, R. A. Leitgeb, and W. Drexler, "Endoscope-tip interferometer for ultrahigh resolution frequency domain optical coherence tomography in mouse colon," *Opt. Express* **14**, 1878-1887 (2006).
34. M. A. Choma, A. K. Ellerbee, S. Yazdanfar, and J. A. Izatt, "Doppler flow imaging of cytoplasmic streaming using spectral domain phase microscopy," *J. Biomed. Opt.* **11** (2006).

35. W. Drexler, O. Findl, R. Menapace, A. Kruger, A. Wedrich, G. Rainer, A. Baumgartner, C. K. Hitzenberger, and A. F. Fercher, "Dual beam optical coherence tomography: signal identification for ophthalmologic diagnosis," *J. Biomed. Opt.* **3**, 55 (1998).
36. A. F. Fercher, C. K. Hitzenberger, W. Drexler, G. Kamp, H. Sattmann, L. F. Schmetterer, I. Strasser, and C. Unfried, "In-vivo dual-beam optical coherence tomography," in *Proceedings of SPIE - The International Society for Optical Engineering*(1994), p. 356.
37. J. W. Goodman, *Statistical Optics* (Wiley and Sons Inc, New York, 1995).
38. R. A. Leitgeb, W. Drexler, A. Unterhuber, B. Hermann, T. Bajraszewski, T. Le, A. Stingl, and A. F. Fercher, "Ultrahigh resolution Fourier domain optical coherence tomography," *Opt. Express* **12**, 2156-2165 (2004).
39. M. Hafez, T. C. Sidler, R. P. Salathe, G. L. M. Jansen, and J. C. Compter, "Design, simulations and experimental investigations of a compact single mirror tip/tilt laser scanner," *Mechatronics* **10**, 741-760 (2000).
40. A. Baumgartner, C. K. Hitzenberger, H. Sattmann, W. Drexler, and A. F. Fercher, "Signal and resolution enhancements in dual beam optical coherence tomography of the human eye," *J. Biomed. Opt.* **3**, 45-54 (1998).
41. B. Möller, "Optische Augenlängenmessung für klinische Anwendungen," in *Département de microtechnique*(EPFL, Lausanne, 2001).
42. R. A. Leitgeb, L. Schmetterer, W. Drexler, A. F. Fercher, R. J. Zawadzki, and T. Bajraszewski, "Real-time assessment of retinal blood flow with ultrafast acquisition by color Doppler Fourier domain optical coherence tomography," *Opt. Express* **11**, 3116-3121 (2003).
43. B. R. White, M. C. Pierce, N. Nassif, B. Cense, B. H. Park, G. J. Tearney, B. E. Bouma, T. C. Chen, and J. F. de Boer, "In vivo dynamic human retinal blood flow imaging using ultra-high-speed spectral domain optical Doppler tomography," *Opt. Express* **11**, 3490-3497 (2003).
44. L. Wang, Y. Wang, S. Guo, J. Zhang, M. Bachman, G. P. Li, and Z. Chen, "Frequency domain phase-resolved optical Doppler and Doppler variance tomography," *Opt. Commun.* **242**, 345-350 (2004).
45. A. H. Bachmann, M. L. Villiger, C. Blatter, T. Lasser, and R. A. Leitgeb, "Resonant Doppler flow imaging and optical vivisection of retinal blood vessels," *Opt. Express* **15**, 408-422 (2007).
46. Y. Yasuno, S. Makita, T. Endo, G. Aoki, M. Itoh, and T. Yatagai, "Simultaneous B-M-mode scanning method for real-time full-range Fourier domain optical coherence tomography," *Applied Optics* **45**, 1861-1865 (2006).
47. R. K. Wang, "In vivo full range complex Fourier domain optical coherence tomography," *Appl. Phys. Lett.* **90** (2007).
48. A. D. Poularikas, and S. L. Hahn, *The Transforms and Applications Handbook* (CRC Press, 1996).



## **Part III**

# **Functional imaging with resonant Doppler Fourier domain optical coherence tomography**





## Chapter 7

### Introduction to functional ophthalmic imaging in FDOCT

#### 7.1 Physiology of the eye

##### 7.1.1 Retina

Within the retina an optical signal is converted into a neuronal activity. This information is transmitted and processed by the brain. The retina structure and function is an interesting research subject for OCT for various reasons:

- Vessels are within an almost transparent retinal tissue structure and therefore easily accessible.
- It offers a way to study some of the complex mechanisms of the brain, such as neuronal transmission and processing.
- Auto-regulation of the retinal blood flow and the interrelation to oxygen metabolism is directly accessible.

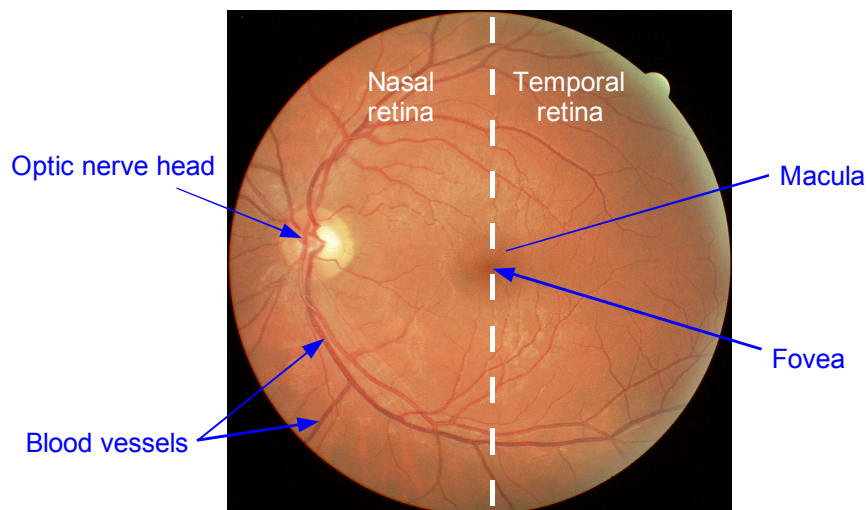


Figure III-1. Fundus image of healthy retina [modified, source: <http://www.goatman.me.uk>].

Figure III-1 shows a fundus image of a healthy eye (diameter of image  $\cong 42mm$ ). The different areas and parts are:

- The *optic nerve head* (also called the optical disk, blind spot or papilla): blood vessels enter through the papilla and nerve signals are transported from and to the brain. The diameter is approx.  $2mm$  (or  $\sim 5^\circ$ ).

- *Blood vessels* (arteries and veins): blood transport and oxygen delivery to the retinal tissue structures.
- The *macula* is the dark spot surrounding the *fovea*. Its diameter is approx. 6mm (or  $\sim 15^\circ$ ); this is the central vision area (opposite to peripheral) for color perception and high resolution vision. It is a mainly avascular region.
- The *fovea* is a small spot of 2mm diameter (or  $\sim 5^\circ$ ) in the centre of the *macula*. The distance between the *optic nerve head* and the *fovea* is around 5mm (or  $\sim 12.5^\circ$ ).

Oxygen is supplied to the retina by the retinal vessels as well as the coroidal tissue layer across the so-called Bruch's membrane.

A retinal histology is shown in Figure III-2. It displays the retina's different layers with a total thickness of approx. 0.5mm. Today, optical coherence tomography reveals this retinal structure with high resolution (compare with Figure III-4) and is at the edge of resolving individual photoreceptors [1].

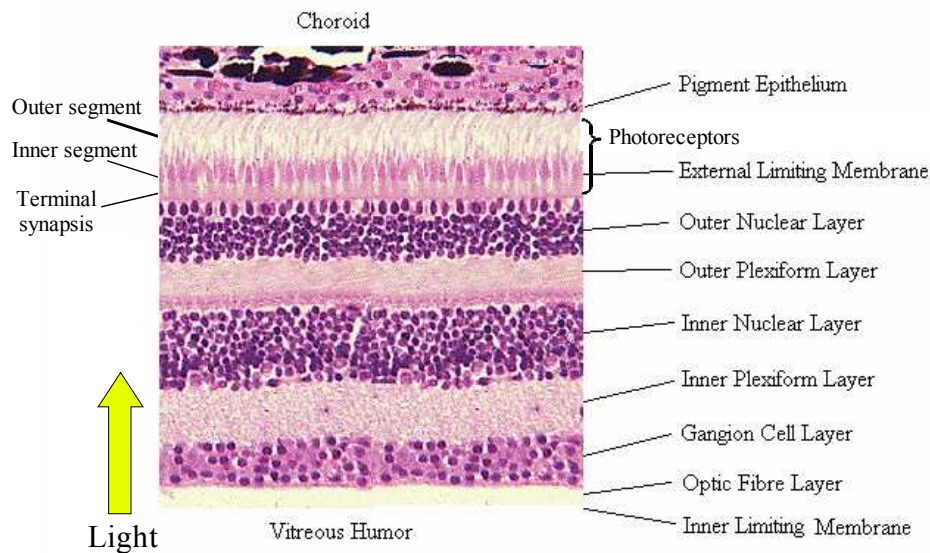
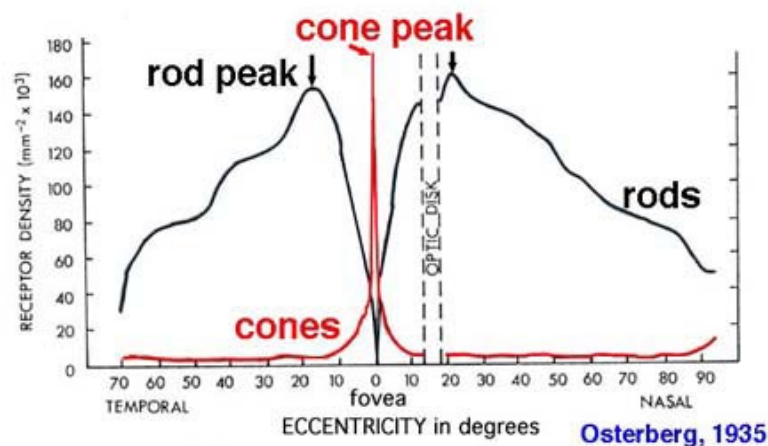


Figure III-2. Histology of retinal layers [modified, source: <http://137.222.110.150/calnet/visual2/page2.htm>].

### 7.1.2 Photoreceptors, phototransduction and color vision

The retina contains two types of photoreceptors (PR) called cones and rods. About 6 million cones and 100 million rods confer color vision and faint light vision respectively. Rods are 1'000 times more sensitive to light than cones. As shown in Figure III-3, cones are concentrated in the fovea and rod cells are principally located in the peripheral area.



**Figure III-3. Distribution of rods and cones on a human retina.** [modified, source: [http://www.phys.ufl.edu/~avery/course/3400/gallery/gallery\\_vision.html](http://www.phys.ufl.edu/~avery/course/3400/gallery/gallery_vision.html)].

The phototransduction phenomenon describes the conversion of light energy into electrical potential [2]. Each PR cell contains a photopigment (molecule called rhodopsin) that activates a chemical reaction when stimulated by light. This reaction generates a membrane potential decrease. This electrical signal will then be transmitted to the brain through the neuronal system. As the rod's photopigment is more sensitive than the one of cones, rod cells saturate in bright light.

Colour vision is due to three different types of cones (Short-S, Medium-M and Long-L), each type having a different spectral sensitivity characteristic [3]. Peak wavelength sensitivities are centred at 430, 530 and 560nm for S (blue), M (green) and L (red) cones respectively. This corresponds to the trichromatic (or RGB) model and it is well known that human eyes have a maximum sensitivity to green light. The length of cones is about 50 $\mu\text{m}$  and their diameter is varying from 0.5 $\mu\text{m}$  to 4 $\mu\text{m}$ . They are smallest in the fovea.

## 7.2 Functional retinal imaging with FDOCT

Fourier domain optical coherence tomography (FDOCT) has become the method of choice in particular for fast retinal *in-vivo* imaging with high three-dimensional resolution [4-6]. Recent developments enhance the clinical and biomedical potential of FDOCT by aiming from purely structural to functional tissue imaging revealing tissue dynamics and physiology. The imaging space is becoming highly multi-dimensional including polarization [7-10], Doppler flow [10-13] and spectroscopy [14, 15].

Differential spectral contrast FDOCT allows *optical staining* of retinal tomograms and contrasting tissue of high pigmentation such as the retinal pigment epithelium (RPE). The spectral contrast from this RPE-layer shows high correlation with results of polarization sensitive OCT [16]. However, spectral contrast FDOCT requires either very broadband light sources, like a fs-Ti:S laser, a synthetic SLD source combining multiple superluminescent diodes (*e.g. Broadlighter* from Superlum Inc.) or simply two distinct SLDs with separate spectral bands. Investigations showed that spectral separation of these distinct bands of at least 80nm is necessary to achieve contrast of spectroscopically different retinal structures such as the RPE layer [16].

Several studies of retinal blood flow using Laser Doppler flowmetry (LDF) outlined the importance of measuring vessel flow properties since it is an early indicator of retinal pathologies like glaucoma, diabetic retinopathy or age related macula degeneration (AMD)

[17-21]. In developed countries, glaucoma is among the leading causes of irreversible vision loss and blindness, AMD is the leading cause of central visual loss in the age group of 65 years and older, whereas diabetic retinopathy is the leading cause of blindness for people of age between 40-80 years [22, 23]. The ability for early indication of these pathologies arises from the fact that retinal perfusion is highly responsive to many pathologic changes of the retina [17, 20, 21]. Several color Doppler (CD) OCT modalities have been developed during the last decades. Early works on CD-OCT were based on time-domain OCT [24, 25]. FDOCT based on phase sensitive signal detection has been already applied to visualize retinal perfusion with high velocity sensitivity and to contrast for example systolic and diastolic blood flow [12]. The advantage of CD-OCT as compared to LDF is the ability to localize retinal perfusion in depth [24]. It is a typical problem for LDF not to be able to distinguish between choroidal and inner retinal perfusion. The first is of particular importance for the understanding of AMD and related neo-vascularization. Recent work in Doppler OCT applied elaborate image processing techniques to extract the retinal vascularization and to differentiate between choroidal and retinal flow bed [10, 26]. CD-FDOCT works best for vascular structures away from the optic nerve head since a limitation of Doppler OCT is the relatively restricted accessible velocity range. This is due to the fact that interference fringe blurring arises from moving structures, such as flow. In the worst case signal from retinal blood vessels is totally lost (see Figure III-4).

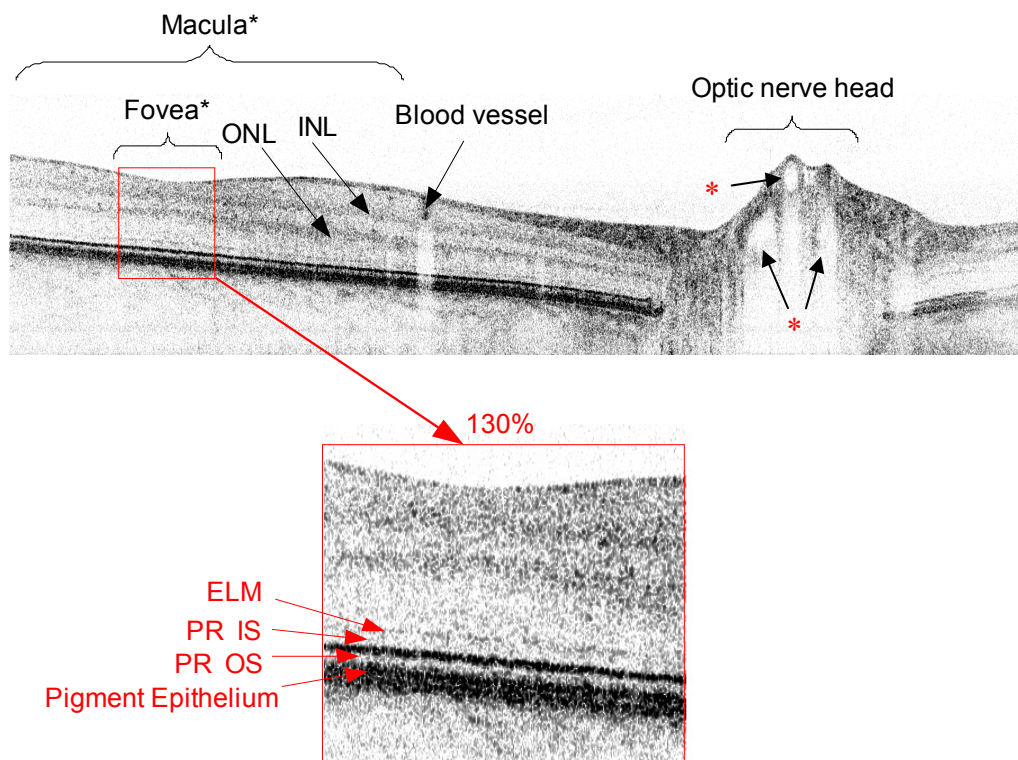


**Figure III-4.** Typical high resolution retinal tomogram with “empty” blood vessels (\*) in the optic nerve head region. Tomogram size: 12mm x 1mm (lateral x depth) with 8.5 $\mu$ m axial resolution (in air). ONL: Outer nuclear layer, INL: inner nuclear layer, ELM: external limiting membrane, PR IS: photoreceptor inner segment, PR OS: photoreceptor outer segment.

The standard method to visualize retinal and choroidal perfusion is still fluorescein angiography. Such methods are invasive since in general fluorescein or indocyanine green (ICG) need to be injected to produce the contrasting of vascular structure on the ocular

fundus. Although the adverse effects of such contrast agents could be reduced, a completely non-invasive assessment would still increase the comfort of the patient together with the easiness in handling such instruments. In addition, a fast tomographic method such as FDOCT would offer the possibility to assess the retinal vascularization in 3D.

Better understanding of retinal physiology may help to prevent and cure retina diseases in the future [27]. Functional imaging has become the trend in FDOCT and first demonstrations of studying retinal response to oxygen breathing using real-time spectrometer-based FDOCT have for example been demonstrated recently by Bower *et al.* [28].



## Chapter 8

### Resonant Doppler FDOCT

#### 8.1 Introduction<sup>\*</sup>

Spectrometer-based FDOCT suffers from inherent imaging artifacts such as complex ambiguity and signal decay in depth which were already subject in Part II. In addition, aliasing, and last but not least interference fringe blurring have to be mentioned. A recent approach to reduce the latter effect for retinal imaging has been the application of pulsed illumination [29]. Fringe blurring in particular limits the detection of moving structures such as flow. In Figure III-4 a typical high resolution retinal tomogram is shown. Blood vessels away from the optic nerve head (ONH) are visible but appear “empty” where flow is highest. Fast flow occurs especially in the region of the ONH where the central retinal artery and vein enter and leave the eye bulb. Hence, it is of great interest to keep the flow signal in this particular region for assessing retinal perfusion.

The approach discussed in this chapter circumvents the limitation of interference fringe blurring by phase-compensating the detection to the sample movement, analogue to a photographer that moves the camera with the object. In effect, static structures will be blurred whereas moving parts such as flow will be enhanced. The present chapter gives first a detailed discussion of the theory of fringe blurring in FDOCT using broad bandwidth light sources. Subsequently the theory of resonant Doppler imaging will be introduced together with the realization of employing electro-optic phase modulation. It will be shown how flow can be measured quantitatively on a pure intensity basis. It should be mentioned that an alternative method of phase-independent Doppler OCT has been introduced recently by analysis of speckle patterns [30]. Finally the method is applied to measure retinal blood flow and 3D vascularization in the ONH region.

#### 8.2 Theory

##### 8.2.1 Chromatic interference fringe blurring

It is a well known fact that in spectrometer-based FDOCT any sample movement causes interference fringe blurring and in consequence reduction of the signal-to-noise ratio (*SNR*).

---

<sup>\*</sup> This chapter was partly published in the following peer-reviewed article:

A. H. Bachmann, M. Villiger, C. Blatter, T. Lasser, and R. A. Leitgeb, „Resonant Doppler Imaging and optical vivisection of retinal blood flow,“ *Opt. Express* **15**, 408-422 (2007).



First analytic discussion of this effect has been given [31], but without accounting for the intrinsic chromaticity of FDOCT and without giving an analytic expression for the true FDOCT signal after Fourier transform. As we will see in due course, the fringe blurring causes not only loss of signal contrast but also signal peak broadening.

Let us assume, without loss of generalization, that we have a single reflecting interface in the sample arm. The reference field  $E_R(k)$  and the sample field  $E_S(k)$  are expressed as functions of the wavenumber  $k$ . We further assume, in the most general case, a time dependent phase shift  $\phi(t)$  between the sample and the reference field. The recorded spectral interference signal, written as number of generated photo-electrons, becomes

$$N(k) = \tau\gamma(I_R(k) + I_S(k)) + 2\gamma\sqrt{I_S(k)I_R(k)} \int_{-\tau/2}^{\tau/2} \cos(2kz_0 + \phi(t))dt, \quad (\text{III.1})$$

with  $I_{S,R}(k) = E_{S,R}(k)E_{S,R}^*(k)$ , the asterisk denoting complex conjugate,  $z_0$  being the optical path length difference between sample and reference interface at  $t=0$ ,  $\tau$  the camera exposure time, and the proportionality factor  $\gamma$  accounting for the detector conversion efficiency. Subsequently we will only consider the last part of Equation (III.1) that actually contains information about the relative sample position. Denoting this part  $N_{AC}(k)$  and assuming a phase shift  $\phi(t)$  that is linear in time, the integration yields [31]

$$N_{AC}(k) = N_{AC}(k, \Delta\Phi = 0) \text{sinc}\left(\frac{\Delta\Phi}{2\pi}\right), \text{ with} \\ N_{AC}(k, \Delta\Phi = 0) = 2\gamma\tau\sqrt{I_S(k)I_R(k)} \cos(2kz_0), \quad (\text{III.2})$$

where we defined  $\text{sinc}(x) \equiv \sin(\pi x)/(\pi x)$ ;  $\Delta\Phi = \phi(\tau)$  is the total phase change during the integration time. The varying phase  $\phi$  reduces the modulation depth of the spectral interference signal across the detector array. The origin of the phase shift can be manifold: often we are faced with involuntary sample movements, in particular during *in-vivo* measurements, or mechanical noise that causes statistical path length changes in the interferometer. In general, the phase change can be approximated as  $\Delta\Phi = \beta + \eta(k - k_0)$  with  $k_0$  being the central wavenumber. It comprises a constant phase term  $\beta$  and a group dispersion term  $\eta = d(\Delta\Phi)/dk$  at  $k_0$ . For the case of a single interface in the sample arm, moving with a constant axial velocity  $v_s$ , the phase shift can be written as  $\Delta\Phi = 2kv_s\tau = 2k_0\Delta z + 2(k - k_0)\Delta z$ , *i.e.*  $\beta = 2k_0\Delta z$  and  $\eta = 2\Delta z$ . The change in optical path length  $\Delta z$  can also be introduced on purpose as in phase shifting FDOCT, using piezo actuators or electro-optic modulators (EOM). The latter case will involve higher order terms in  $k$  for the resulting total phase shift due to the dispersion of the EOM crystal, which usually is Lithium Niobate ( $\text{LiNbO}_3$ ). An example for purely achromatic phase shifting, *i.e.*  $\eta = 0$ , has recently been given by employing acousto-optic frequency shifters to realize heterodyne FDOCT detection [32].

Keeping the linear dependence of the phase shift on  $k$ , we continue in calculating the FDOCT signal that is obtained by Fourier transforming Equation (III.2) with respect to  $k' = k - k_0$ . Expressing the *sinc*-function in Equation (III.2) as  $\text{sinc}\left(\frac{\beta + \eta(k - k_0)}{2\pi}\right) = \text{sinc}\left(\frac{\eta k'}{2\pi}\right) \otimes \delta\left(k' + \frac{\beta}{\eta}\right)$ , and applying the convolution theorem we obtain

$$\widehat{N}_{AC}(z) = \widehat{N}_{AC}(z, \Delta\Phi = 0) \otimes \frac{1}{|\eta|} \text{rect}\left(\frac{z}{\eta}\right) e^{j\frac{\beta}{\eta}z}, \quad (\text{III.3})$$



where  $\hat{\cdot}$  denotes the Fourier transformed signal. We see that for  $\beta=0$ , *i.e.* a change in group dispersion, the original axial point spread function (PSF), which is determined by the temporal coherence function of the light source, is averaged and broadened, due to the convolution with a *rect* function. However, for an exact signal analysis we need to take into account the complex exponential term  $\exp(j\beta z/\eta)$  which is direct result from our spectral bandwidth centered at  $k_0$ .

Assuming a Gaussian source spectrum with a full-width-at-half-maximum (FWHM) value  $\Delta k_{FWHM}$  centered at  $k_0$  and writing the convolution in Equation (III.3) explicitly one finds

$$\hat{N}_{AC}(z) \propto \frac{1}{|\eta|} \int_{-\infty}^{\infty} e^{-\alpha^2(z' \pm 2z_0)^2} \text{rect}\left(\frac{z-z'}{\eta}\right) e^{j\frac{\beta}{\eta}(z-z')} dz', \quad (\text{III.4})$$

with  $\alpha = \Delta k_{FWHM} / (4\sqrt{\ln(2)})$  being the inverse of the round trip coherence length. The effect of the *rect*-function is to change the integration borders to  $z \pm \eta/2$ . The result of this integral will exhibit two signal peaks, centered at  $z=2z_0$  and  $z=-2z_0$ , symmetric around the zero path delay due to the complex ambiguity of the FDOCT signal. Keeping only the peak at  $z=2z_0$ , and using iterative partial integration together with the definition of the Hermite polynomial of order  $m$ ,  $H_m = (-1)^m \exp(x^2) d^m(\exp(-x^2))/dx^m$ , gives

$$\hat{N}_{AC}(z) \propto \frac{-je^{j\frac{\beta}{\eta}z}}{\beta} \left[ e^{-\alpha^2(z'-2z_0)^2} e^{-j\frac{\beta}{\eta}z'} \sum_{m=0}^{\infty} \left( \frac{-j\alpha\eta}{\beta} \right)^m H_m(\alpha(z'-2z_0)) \right]_{z'=z-\eta/2}^{z'=z+\eta/2}. \quad (\text{III.5})$$

The different summation terms in Equation (III.5) are weighted by  $\alpha\eta/\beta$ . In case of a moving sample interface we have  $\alpha\eta/\beta = \alpha/k_0 = \Delta\lambda_{FWHM} / (2\sqrt{\ln(2)}\lambda_0)$ , which is usually much smaller than one. In this case the contributions of  $m \geq 1$  can be neglected. Upon using  $H_0=1$ , the absolute value of the expression in Equation (III.5) can then be simplified to

$$|\hat{N}_{AC}(z)| \propto \frac{\sqrt{2}e^{-\alpha^2\frac{\eta^2}{4}}}{\beta} e^{-\alpha^2(z-2z_0)^2} \sqrt{\cosh(\alpha^2 2(z-2z_0)\eta) - \cos(\beta)}. \quad (\text{III.6})$$

Evaluating this expression at the interface position  $z_0$ , *i.e.*  $(z-2z_0)=0$  for a displacement during camera exposure  $\Delta z$ , yields

$$|\hat{N}_{AC}(z=2z_0)| \propto e^{-\alpha^2\frac{\eta^2}{4}} \left| \text{sinc}\left(\frac{\beta}{2\pi}\right) \right| = e^{-\alpha^2(\Delta z)^2} \left| \text{sinc}\left(\frac{k_0\Delta z}{\pi}\right) \right|. \quad (\text{III.7})$$

Comparing this result with Equation (III.2) shows the expected signal decay following a *sinc*-function. This is the result that would be expected for the achromatic case since it depends only on  $\beta$ . The effect of the  $\eta$ -term is an additional dampening factor that depends on the ratio between round trip coherence length  $1/\alpha$  and change in group dispersion  $\eta$ . For the moving sample interface, the first zero of the *sinc*-function is reached at  $\Delta z = \lambda/2$ . Knowing the integration time  $\tau$ , the corresponding sample velocity is then expressed as  $v_s = \lambda/(2\tau)$ . In the ideal achromatic case, the axial peak shape remains Gaussian. Plotting in Figure III-5 the axial peak shape for the moving sample interface as expressed by Equation (III.6), it is

revealed that the  $\eta$ -term causes in addition peak broadening, which will eventually split up the signal and create two diverging signal peaks. The peak splitting is given by the width of the rect-function in Equation (III.4) which in turn is equal to the displacement  $\Delta z$ . Nevertheless, as seen from Figure III-5, high  $SNR$  and large optical bandwidth is needed in order to observe this effect. Figure III-5(a) indicates the normalized signal attenuation  $\mathcal{A}(\Delta z)$ , by plotting the normalized FDOCT signal peak heights (Equation (III.6)) as a function of  $\Delta z$ .

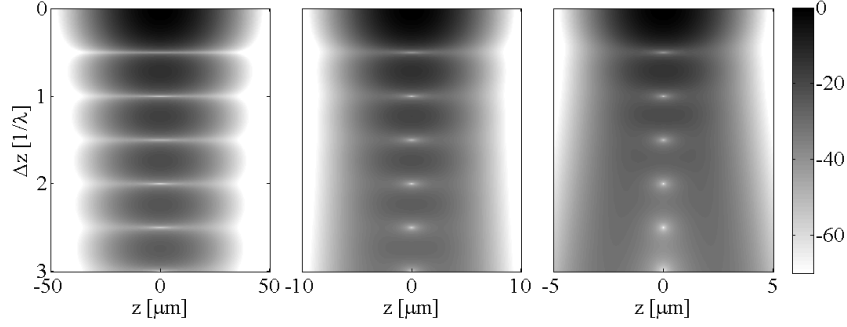


**Figure III-5.** Normalized signal attenuation  $\mathcal{A}$  as a function of  $\Delta z$ , the displacement of a sample surface during the integration time, and  $z$ , the axial coordinate in  $dB$ . The three plots correspond to a  $\Delta k_{FWHM}$  of  $0.2/\mu m$ ,  $1/\mu m$  and  $2/\mu m$ . For larger spectral bandwidths, the signal decays faster with  $\Delta z$  and the splitting occurs earlier.

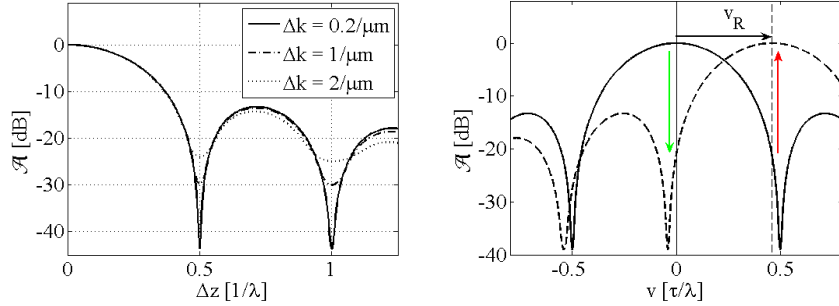


**Figure III-6.** (a) Maximum value in  $z$ -direction of the normalized signal attenuation  $\mathcal{A}$  as a function of displacement  $\Delta z$  for the same parameters as in Figure III-5. (b)  $\mathcal{A}$  as a function of sample velocity for the static case (solid line) and with a reference velocity offset  $v_R$  (dashed line). As indicated, the reference velocity offset reduces static structure intensity (green arrow) and enhances moving structure intensity (red arrow).

### 8.2.2 Signal recovery by reference phase tuning

In the preceding paragraph we mentioned the possibility to introduce phase shifting elements into the reference arm. If the phase shifting is performed during camera integration, then the overall phase shift  $\Delta\Phi$  (see Equation (III.2)) will in general have contributions from both interferometer arms, *i.e.*,  $\Delta\Phi = \Delta\Phi_R - \Delta\Phi_S$ . One immediately observes that for the phase matching condition

$$\Delta\Phi_R = \Delta\Phi_S \quad (III.8)$$

the overall phase shift is zero, meaning that there is no interference fringe blurring and the signal will be completely recovered. The reference phase shifting can in principle be realized by a piezo actuator which is, however, relatively slow for fast and precise phase changes. We propose therefore to use an electro-optic modulator (EOM) in which case the phase change is

realized by changing the refractive index of the EOM crystal fast axis. The corresponding phase shift will be a function of the voltage applied to the EOM. The relation  $V_\pi(k) = (2\pi a - bk)/(Qk)$ , the voltage at which for a certain wavenumber the phase is shifted by  $\pi$ , together with the constants  $a$ ,  $b$  and  $Q$ , are provided by the manufacturer. The total change of the reference phase can be expressed as  $\Delta\Phi_R(k) = \pi\Delta V/V_\pi$ , with  $\Delta V$  being the change of voltage during integration time. A Taylor expansion of  $V_\pi(k)$  yields  $\beta = \pi Q k_0 \Delta V / (2\pi a - b k_0)$  and  $\eta = 2\pi^2 Q a \Delta V / (2\pi a - b k_0)^2$ . It is then possible to associate a reference path length shift  $\Delta z_R$  to the  $\beta$ -term as

$$\Delta z_R = \frac{\beta}{2k_0} = \frac{\pi \Delta V}{V_\pi(k_0) 2k_0}. \quad (\text{III.9})$$

Finally, since the integration time is  $\tau$ , we can write for the corresponding reference speed  $v_R = \Delta z_R / \tau$ , leading to a Doppler frequency of  $f_R^D = k_0 v_R / \pi$ . According to Equation (III.8), this reference speed can compensate for the phase shift caused by sample movement, in particular of flow. For axial flow at constant speed  $v_S$  we can write  $\Delta\Phi_S(k) = 2k v_S \tau$ . For  $v_S = v_R$  the  $\beta$ -terms cancel out, but due to the group index of the EOM, the  $\eta$ -terms will not compensate completely resulting in a signal peak broadening. Nevertheless, even for a large source bandwidth of  $200\text{nm}$  at a central wavelength of  $800\text{nm}$ , the difference to the ideally compensated situation will be smaller than  $-1\text{dB}$  and can therefore be neglected. The important point is that the maximal detection sensitivity has been effectively shifted to the reference velocity  $v_R$ , as shown in Figure III-6(b). It is worth noting that the maximum detectable velocity or Doppler frequency is independent of the Nyquist limit given by half the camera acquisition rate. The center Doppler frequency can in theory be shifted to arbitrary values only limited by the maximal EOM phase shift during camera exposure. It can be tuned to a particular velocity or associated Doppler frequency for which the sample Doppler frequency will be in resonance. The moving sample signal is then detected with high contrast whereas the signals of static structures are attenuated. The contrast between static and moving structures will be higher, the larger the actual sample velocity is.

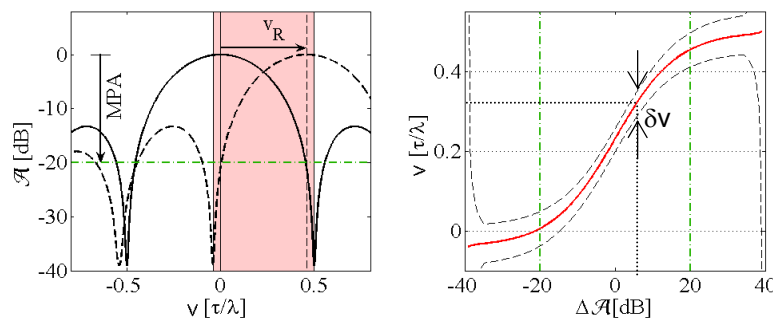


**Figure III-7. (a) Signal attenuation  $\mathcal{A}$  for the static (solid line) and shifted case (dashed line). The red shaded region indicates the intersection of the main lobes. The green dash-dotted line indicates the MPA for a typical local signal in the tomogram. (b) Velocity as a function of the quotient  $\Delta\mathcal{A}$  of the shifted and the static case within the red shaded area (red solid line). The curve allows associating to a given  $\Delta\mathcal{A}$  value a unique sample velocity  $v_S$ . The velocity error  $\delta v$  (Equation (III.14)) can be read from the dashed line. Within the green dash-dotted lines it is possible attributing a unique velocity value (see text for details).**

### 8.2.3 Differential velocity mapping

The freedom of driving the EOM with programmable phase slopes opens additional advantages of the resonant Doppler scheme. By driving the EOM with voltage ramps having inverse slopes, one obtains in effect two images where structures with opposite flow directions with respect to the optical axis appear enhanced. Flow inversion may be due to either different orientations of the same vessel or opposite flow direction in arteries and veins. A clear distinction is in fact possible within a true 3D reconstruction of the vessel bed. The two images can be subtracted having positive and negative intensity values in blue and red respectively to realize a bidirectional color Doppler flow map. Such representation has the additional advantage of removing spurious signals of static structures that will be visible depending on the reference velocity offset. One achieves a differential flow mapping already on an intensity basis without the need of evaluating FDOCT signal phase differences. It should be mentioned that the opposite reference velocities of course do not need to be the same; they can be individually tuned to the given sample flows in either direction by changing the respective EOM phase slope.

The above differential resonant Doppler scheme involves two phase slopes. We can also drive the EOM by one slope together with a constant voltage level. Knowing the exact reference velocity together with the theoretical signal decay, as shown in Figure III-7(a), one can then reconstruct the actual sample velocity based on the quotient between the two channels. Let us start with a reference velocity  $v_R$  and an a priori unknown sample velocity  $v_S$ . Since we know the reference velocity we also know the normalized signal attenuation  $\mathcal{A}(v_S)$  and  $\mathcal{A}(v_S - v_R)$ . Having measured a signal level of  $\hat{I}^0$  for constant EOM voltage and a signal  $\hat{I}^\varphi$  for the channel shifted by  $v_R$ , we then can write

$$\frac{\hat{I}^\varphi}{\hat{I}^0} = \frac{\mathcal{A}(v_S - v_R)}{\mathcal{A}(v_S)} = f(v_S), \quad (\text{III.10})$$

and thus in principle

$$v_S = f^{-1}\left(\frac{\hat{I}^\varphi}{\hat{I}^0}\right). \quad (\text{III.11})$$

However, such reconstruction will be unambiguous only in the range  $[v_R - \lambda_0/(2\tau), \lambda_0/(2\tau)]$  indicated by the red shaded region in Figure III-7(a). Within this range one can associate a unique velocity value to a given signal attenuation difference  $\Delta\mathcal{A}$  as shown in Figure III-7(b). In practice this range is determined by the fact that a local signal can only be attenuated down to the noise level. This defines a maximum possible attenuation (MPA) (see Figure III-7). The velocity error is directly related to the *SNR* within the image channels  $\hat{I}^\varphi$  and  $\hat{I}^0$ . Writing for the logarithmic signal difference  $Q$  (assuming equal noise  $\delta\hat{I}$ ) with an error  $\delta Q$ , and defining  $\hat{I}_S$  as the theoretical signal level without blurring, we can write

$$\begin{aligned} Q + \delta Q &= \log(\hat{I}^\varphi + \delta\hat{I}) - \log(\hat{I}^0 + \delta\hat{I}) \approx \\ &\approx \log(\hat{I}_S \mathcal{A}(v_S - v_R) + \delta\hat{I}) - \log(\hat{I}_S \mathcal{A}(v_S) + \delta\hat{I}), \end{aligned} \quad (\text{III.12})$$

and we finally find for the statistical error of the differential image

$$\delta Q = \frac{1}{\sqrt{SNR}} \sqrt{(\mathcal{A}(v_S - v_R))^{-2} + (\mathcal{A}(v_S))^{-2} + O(\delta\hat{I}^2)}, \quad (\text{III.13})$$

where we used the definition  $SNR \equiv (\hat{I}_S / \delta \hat{I})^2$  and assumed that the signal intensities are large as compared to the noise. The expression in Equation (III.13) can be compared to the phase difference error of phase-sensitive Doppler FDOCT being [9]  $\delta(\Delta\varphi) = 1/\sqrt{SNR}$ . The important difference is the dependence of the error on the signal attenuation for the static and the reference shifted channel  $\mathcal{A}(v_S)$  and  $\mathcal{A}(v_S - v_R)$  respectively. The actual value of the absolute velocity error  $\delta v$  depends on  $\delta Q$  as well as on the local derivative of  $\Delta\mathcal{A}(v_S)$  as shown in Figure III-7(b) as

$$\delta v|_{v_S} = \delta Q \left( \frac{d(\Delta\mathcal{A})}{dv} \right)^{-1} \Big|_{v_S}. \quad (\text{III.14})$$

The accessible unambiguous range and precision can be increased by using a three-stage EOM signal involving for example two inverse slopes together with a constant level, producing the tomograms  $\hat{I}^\varphi, \hat{I}^{-\varphi}$  and  $\hat{I}^0$  (see Figure III-8(A)). The only restriction is that the three attenuation curves need a common intersection part of their main lobes. A differential analysis of the three tomograms allows to determine the axial velocity of any sample motion such as flow in the range  $[-\lambda_0/(2\tau), \lambda_0/(2\tau)]$  (see also §8.4). Note that the velocity bandwidth is dependent on the camera exposure time  $\tau$  which is smaller than the camera line period  $T$ . The latter determines the unambiguous velocity bandwidth of phase-sensitive Doppler FDOCT as  $[-\lambda_0/(4\tau), \lambda_0/(4\tau)]$  [33].

An idea about the velocity can already be obtained by using the three different images as RGB channels for a color encoded Doppler image: red and blue encoding the opposite flow velocities and green displaying the static sample structure.

Finally it should be mentioned that, like in phase-sensitive Doppler FDOCT, only the axial component of flow  $v_{ax}$  is directly available. In principle a 3D reconstruction allows to extract the angle  $\theta$  of a vessel with respect to the optical axis. The actual speed would then be obtained from  $v = v_{ax}/\cos(\theta)$ . Such extension of the method, based on the same resonant Doppler scheme, was recently published by Michaely *et al.* [34].

## 8.3 Experimental

### 8.3.1 Setup

The setup is displayed in Figure III-8. It is a modified Mach-Zehnder configuration. The source is synthesized by two superluminescent diodes (EXALOS) with center wavelengths  $827nm$  and  $853nm$  and respective full-width-at-half-maximum values (FWHM) of  $25nm$  and  $34nm$  resulting in an overall FWHM of  $36nm$ , a central wavelength of  $833.5nm$  and an axial resolution of  $8.5\mu m$  in air. The light is first linearly polarized (Pol) in order to match the fast axis orientation of the EOM's  $LiNbO_3$  crystal. The reference arm contains the non-resonant EOM (NovaPhase) for phase shifting and a quarter waveplate in order to realize circular polarization. The EOM is driven by an arbitrary function generator (Agilent 33220A-001) followed by a high voltage amplifier (20x). The dispersion compensation matches both sample arm optics as well as the water chamber of the eye. The translation stage (TS) helps to adjust the reference to the sample arm length. The sample arm contains a  $LiNbO_3$  crystal to match the dispersion of the EOM in the reference arm. The light is then expanded with a Galilei telescope of focal lengths  $f_1 = -40mm$  and  $f_2 = 100mm$ . The light passes the X-Y galvo

scanning stage (X-Y Sc) (Cambridge Technology) and illuminates the eye via lenses  $f_3=60mm$  and  $f_4=30mm$ . The optical power at the cornea is  $300\mu W$  which is safe for direct beam viewing according to the ANSI laser safety regulations [35]. After recombination, the reference and sample arm light is guided through a single mode fiber to the spectrometer module. The spectrometer is equipped with a volume diffraction grating (DG) (Wasatch, 1200lines/mm), and an objective lens (OL) with focal length 135mm. The CCD is a line scan camera (ATEMEL AVIIVA, 2048 pixel, 12bit) where only 1024 elements are actually used. The camera is driven at a line rate of 17.4kHz with an integration time of  $\tau=43\mu s$ . The full covered spectral width is 68nm resulting in a depth range in air of 2.6mm. The beam waist at the cornea is 1.8mm. The measured sensitivity is 98dB close to the zero delay with a sensitivity decay of -7dB/mm.

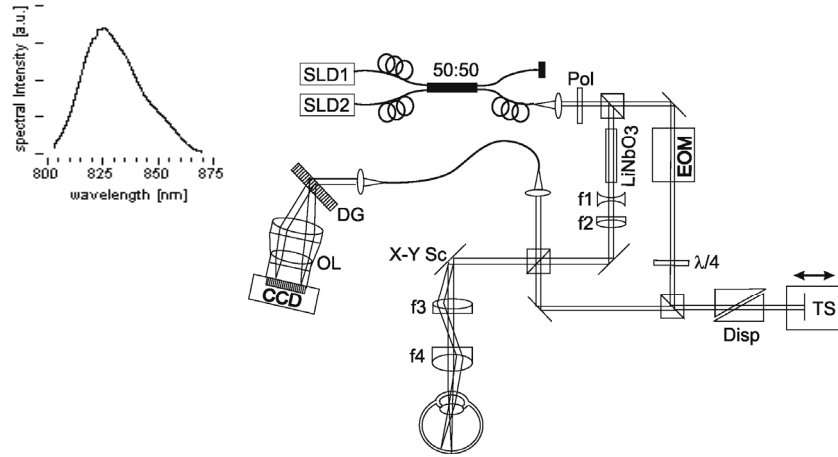


Figure III-8. Optical setup for resonant Doppler FDOCT (see text for details).

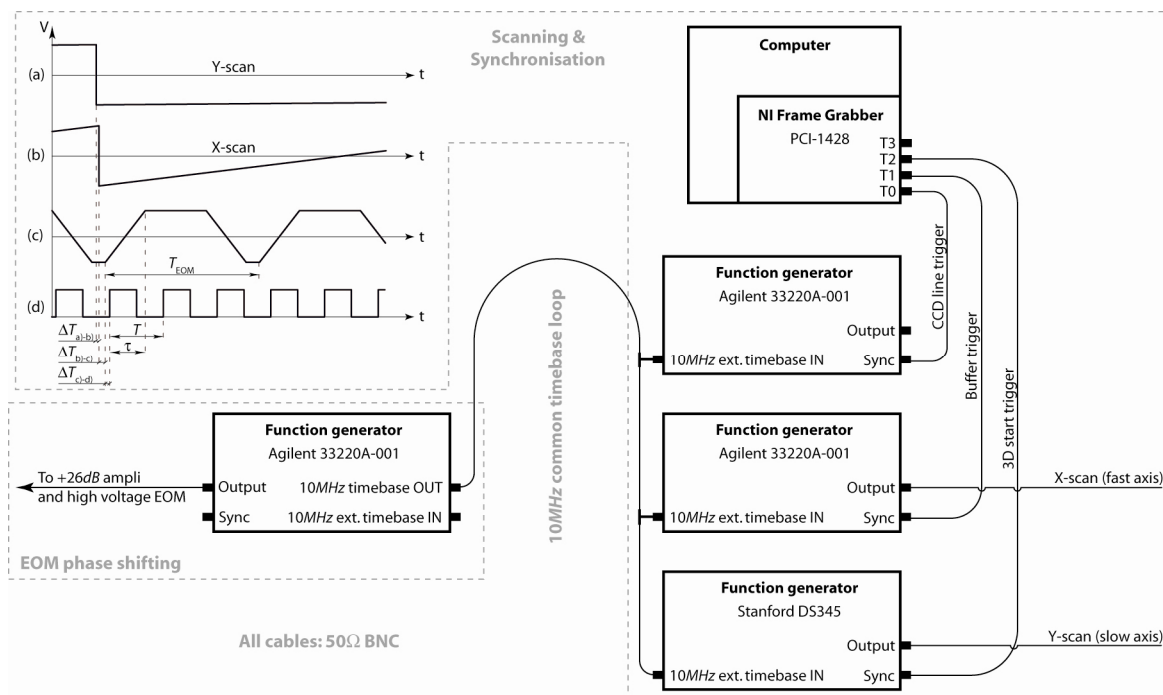
For a maximal voltage slope applied, the realized EOM phase shifts during the camera integration time of  $\tau=43\mu s$  are  $\Delta\Phi_{ref}(k)=\pm 2\pi$  at the center wavelength of 833.5nm corresponding to a velocity of  $v_R=\lambda/2\tau=\pm 9.7mm/s$  and an associated Doppler frequency of  $\pm 23.3kHz$ . The transverse scanning is performed continuously with a theoretical spot size ( $1/e^2$ -intensity) of  $14\mu m$  at the retina.

### 8.3.2 Detailed synchronization scheme

The main issue in synchronization for resonant Doppler FDOCT is the correct timing between EOM phase shifting and camera integration. The EOM voltage curve in Figure III-9(c) shows the three-stage mode as explained at the end of §8.2.3, programmable on the arbitrary function generator via USB. Up-shifting, static, and down-shifting together correspond to one EOM period, in the case of this three-stage mode exactly three times longer than the camera acquisition period:  $T_{EOM}=3T$ . It is important to distinguish between integration time  $\tau$  and acquisition period  $T$  (inverse of line rate) of the camera, since the accessible velocity range is dependent on  $\tau$  and not  $T$  as pointed out already in §8.2.3. If enough signal would be available,  $\tau$  could almost arbitrarily be shrunk with respect to the camera acquisition period  $T$  and the detected velocity band displaced accordingly.

It is also conceivable to drive other voltage curves than a linear slope corresponding to a linear phase shift. Integration of a sinusoidally modulated signal with a linear phase shift in time produces a *sinc*-function in attenuation (see also Figure III-6 and Figure III-7(lhs)). A smoother attenuation curve could potentially present some interest, not presenting such strong side lobes as in the previously discussed case.

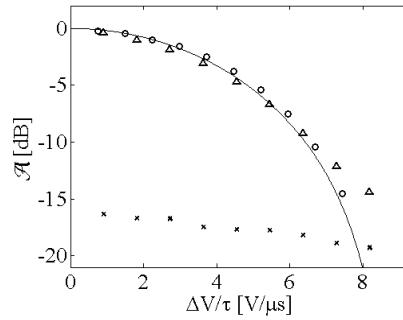
The different trigger signals are slightly delayed by adjusting the phase of the applied voltage function. This is important to allow the frame grabber detecting the three different trigger levels sequentially. A certain number of lines should only be acquired once the buffer trigger launched the 2D tomogram. In case of a three-dimensional tomogram acquired, latter trigger, however, should only be seen by the frame grabber once the 3D start trigger was launched. Each trigger channel is armed upon detecting its superior trigger level. Since this needs a bit of time and function generators do present a slight jitter, a short delay is induced between the different trigger channels. A very short delay  $\Delta T_{\text{c-d}}$  of approximately half a microsecond was set between the EOM period start and the camera line trigger ((d) in Figure III-9). The EOM voltage ramp was set accordingly to  $\tau+1\mu\text{s}$ . Other delays were put to  $\Delta T_{\text{a-b}}\approx 5\mu\text{s}$  (optional) and  $\Delta T_{\text{b-c}}=1-5\mu\text{s}$  (important).



**Figure III-9. Synchronization scheme for resonant Doppler FDOCT. (a) Y-scan, 3D start trigger synchronous to falling edge; (b) X-scan, buffer trigger synchronous to falling edge; (c) EOM voltage function; (d) CCD line trigger. Relative frequency accuracy and long time stability is achieved as for heterodyne FDOCT via a 10MHz common external timebase. Synchronization of line/buffer acquisition and scanning is as well achieved using individual function generators with external 10MHz timebase input. See text for details.**

## 8.4 Results and discussion

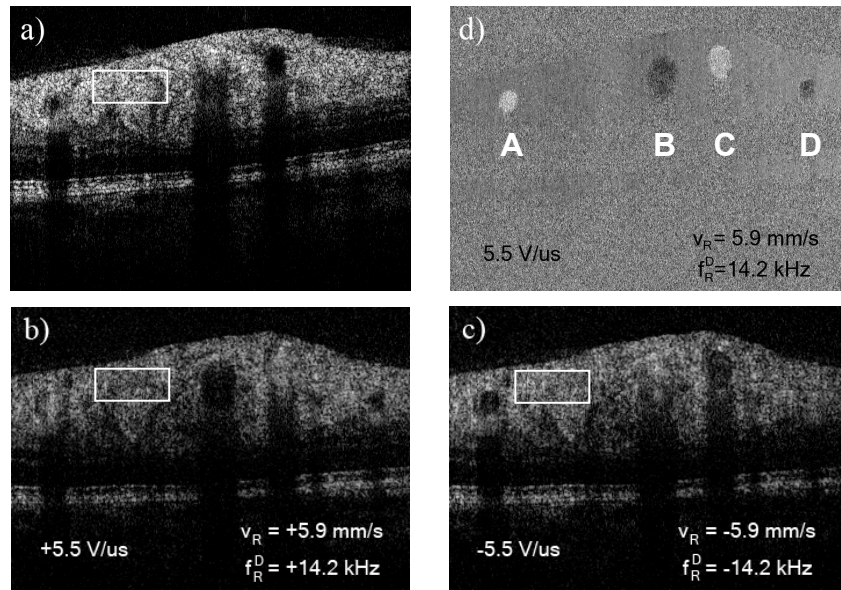
In a first step we measured the actual signal attenuation introduced by the EOM phase shifting by using a mirror as a sample. The curve showing the normalized signal decay with applied EOM voltage is plotted in Figure III-10 (circles). The measurement is in good agreement with the theoretical estimation according to Equation (III.6) (solid line in Figure III-10).



**Figure III-10.** Normalized signal attenuation  $\mathcal{A}$  for different samples due to the applied EOM phase slope: mirror (circles), *in-vivo* retinal structure (triangles) for ROIs in Figure III-11(a-c) compared to theory (solid line) (Equation (III.6)). Crosses represent the maximum possible attenuation (MPA) of the static structure in Figure III-11(a).

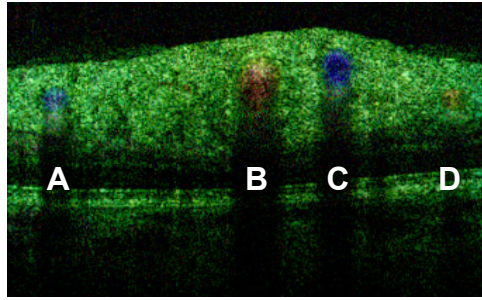
This measurement is then repeated for an *in-vivo* measurement of static retinal structure close to the ONH. The movies in Figure III-11 show a time sequence at the same vertical position after correction of movement artifacts between tomograms using image registration [1, 36]. The EOM voltage slope was stepwise changed from 0.91 to 8.2 V/ $\mu$ s in steps of 0.91 V/ $\mu$ s during the recording of 81 tomograms. A single tomogram is acquired in 130 ms and consists of 2250 lateral points covering a range of 3 mm on the retina. Assuming the theoretic spot size of 14  $\mu$ m we thus have 10.5x over-sampling transversally. The recorded tomogram data has effectively three individual channels with 750 transverse points, each obtained quasi in parallel via the scheme outlined in Figure III-8(A): firstly, the standard FDOCT tomogram with attenuated flow signals due to interference fringe blurring (see Figure III-11(a)); secondly, two tomograms where the static structure is gradually suppressed due to increasing EOM voltage slopes and the respective opposite flow signals are gradually enhanced (see Figure III-11(b,c)). We chose a region in Figure III-11(b) and (c) where only static structure was present and calculated the average signal relative to the same region in the static channel (Figure III-11(a)) for each EOM voltage slope (triangles in Figure III-10). Each point represents an average over eight frames at the same voltage slope. As one can see, the measured structure attenuation deviates from the theoretical decay for higher voltage slopes. In order to explain this effect we calculated the MPA by referencing the average signal of the static structure within the indicated ROI in Figure III-11(a) to the average noise floor in the phase-shifted channels for each voltage slope (crosses in Figure III-10). The ROI was selected such that it contains only static structure avoiding flow signals. Along with the attenuation of the static structure the ratio of number of noise components to signal components within the ROIs of the phase-shifted channels increases. Thus, the signal attenuation will eventually reach the MPA value.





**Figure III-11.** Time sequence (after registration) with a three-stage EOM signal applied showing the same vertical position on the retina with stepwise increasing EOM voltage; all tomograms in log-scale. (a) (Movie: 1.8 MB) Static retinal structure which does not change with increasing phase shift applied, (b,c) (Movies: 1.7 MB, 1.7 MB) phase-shifted tomograms with opposite phase shifting directions and (d) (Movie: 1.9 MB) calculated tomogram representing  $\hat{I}^\varphi / \hat{I}^{-\varphi}$ . Axial flow directions are clearly visible for all four vessels. Tomogram size:  $2.75\text{mm} \times 1.24\text{mm}$  (lateral  $\times$  depth) with  $8.5\mu\text{m}$  axial resolution (in air). Multimedia files are available on OpticsInfoBase at: <http://www.opticsinfobase.org/abstract.cfm?URI=oe-15-2-408>.

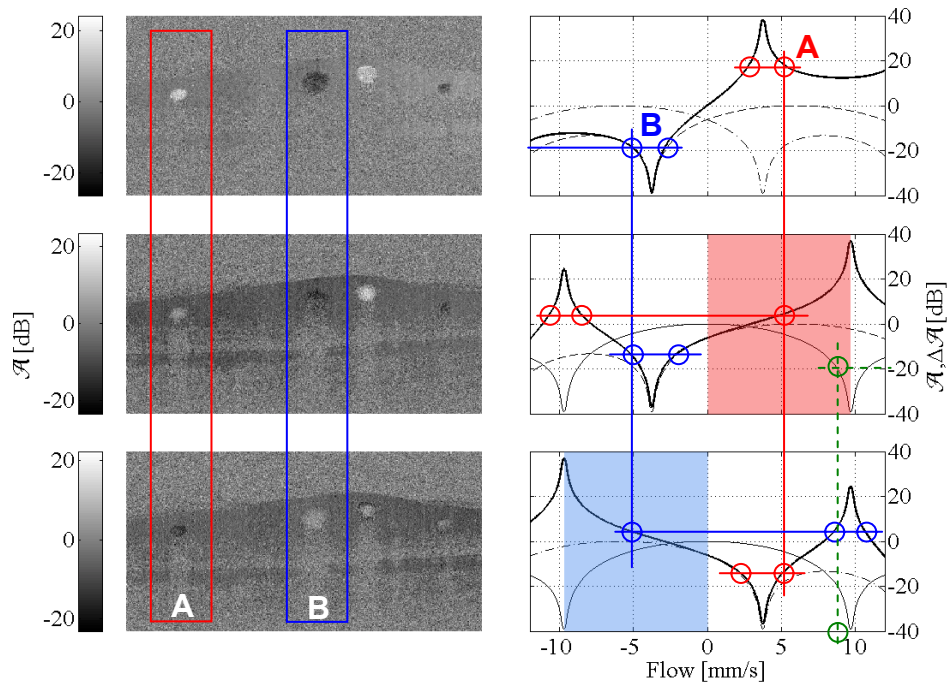
In the phase-shifted channels (Figure III-11(b,c)) one can clearly observe the loss of contrast for the static structures, whereas flow signals gain in contrast. The tomogram in Figure III-11(d) corresponds to the logarithmic differential signal between the two inversely phase-shifted channels, *i.e.*  $\log(\hat{I}^\varphi / \hat{I}^{-\varphi})$ . In the logarithmic representation, the static structure is well suppressed whereas flow in opposite directions will have different signs and can easily be distinguished via appropriate adjustment of a grey level scale. This representation allows actually identifying roughly the velocity range by observing at which EOM voltage the flow signals will appear brightest or darkest. This in fact demonstrates clearly the idea of the resonant Doppler scheme. We observe that for vessels A and D (see Figure III-11(d)) the resonant region is situated at about  $\pm 6.4\text{V}/\mu\text{s}$ , corresponding to a flow velocity of approximately  $\pm 6.9\text{mm/s}$ , whereas for vessel B one finds a value at about  $-4.6\text{V}/\mu\text{s}$  with a corresponding velocity of  $-5\text{mm/s}$ . Only vessel C seems to gain gradually in contrast towards the maximum applied voltage slope of  $8.2\text{V}/\mu\text{s}$ , hence  $v > 8.9\text{mm/s}$ . The high flow velocities present in vessel C exceed in fact the detection bandwidth. Only within the bandwidth the signal will be visible. This bandwidth is now shifted with reference velocity during the time sequence. In addition we have flow changes because of blood pulsation during the data acquisition. Those effects together manifest as rings within the vessel that seem to move radially during the sequence. The velocity values are estimates of  $\pm 0.9\text{mm/s}$  given the voltage slope step size of  $0.91\text{V}/\mu\text{s}$ . Comparing tomograms Figure III-11(b,d) to Figure III-11(a), the strong contrast enhancement realized by the introduced method is particularly well visible for vessels A and C. Since we do not correct for bulk motion velocity artifacts [9, 10] they manifest as vertical band-like structures visible in Figure III-11(d).



**Figure III-12.** (Movie: 1.8 MB) Time sequence of Figure III-11(a-c) in RGB representation. Multimedia: <http://www.opticsinfobase.org/abstract.cfm?URI=oe-15-2-408>.

The combination of the three channels as RGB entries of a color image results in the representation of Figure III-12. For low EOM voltage slopes the signal level will be approximately the same in all three channels resulting in an essentially black and white image. As the voltage increases the image turns gradually green, representing the static image channel, with the vessels tending towards blue and red (opposite flow directions). Hence the color within the vessels is also a qualitative indicator of the present velocities.

A clear quantitative value can be found by a differential analysis of all three channels as described in §8.2.3 and shown in Figure III-13. The tomograms are extracted from the time series in Figure III-11 at EOM voltage slopes of  $\pm 5.5 V/\mu s$ . The left column shows the logarithmically scaled differential images  $\hat{I}^\varphi/\hat{I}^{-\varphi}$ ,  $\hat{I}^\varphi/\hat{I}^0$  and  $\hat{I}^{-\varphi}/\hat{I}^0$  respectively with outlined vessels (A,B in Figure III-13). The right column shows the respective expected differential signal attenuation curves  $\Delta\mathcal{A}$  as function of flow velocity (cf. also Figure III-7). Combining the information of the three graphs, as is demonstrated for two selected vessels (A,B) in Figure III-13, one is able to find unique values for flow velocities via comparison and exclusion on a pure intensity basis. This can be easily realized by first observing from the upper row in Figure III-13 whether the corresponding velocity for a given intensity value is positive or negative. For a positive value one uses the red shaded range in the second row for unique velocity determination whereas for a negative value the blue shaded region in the third row. The maximum flow velocity which can be determined quantitatively is limited by the MPA value. We determined the MPA by calculating an average signal intensity and setting the MPA equal to the corresponding negative SNR, yielding  $MPA = -18.4 dB$ . This in turn gives a range of quantifiable velocity of  $\pm 8.76 mm/s$  (green dashed line in Figure III-13) which is not achievable with phase-sensitive Doppler FDOCT due to fringe blurring.



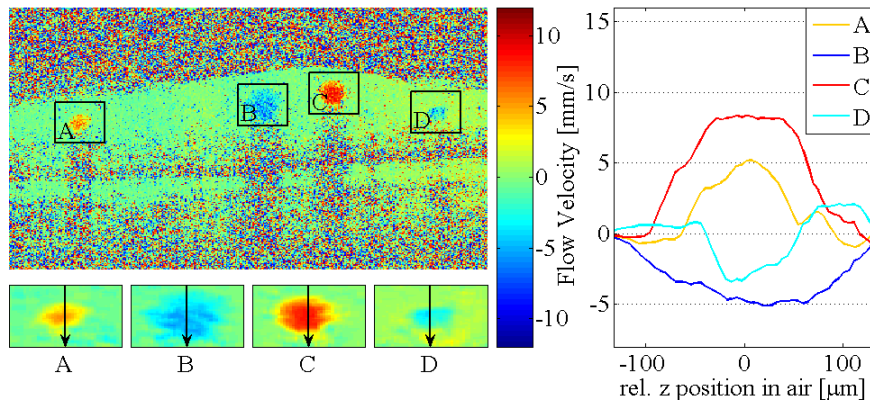
**Figure III-13. Velocity determination by unambiguous differential velocity mapping** (see §8.2.3). For each differential image (lhs) a corresponding theoretical  $\Delta\mathcal{A}$  curve (rhs) is shown. The blue and red solid lines correspond to the selected vessels on the lhs. The horizontal lines and circles on the rhs indicate possible velocity values according to the intensity level in the corresponding tomogram. The ambiguity is removed by looking for the common velocity in all three differential maps as indicated by the respective vertical lines on the rhs. The green dashed lines indicate the MPA limit of  $-18.4\text{dB}$ . Tomogram size:  $3\text{mm} \times 1.65\text{mm}$  (lateral  $\times$  depth) with  $8.5\mu\text{m}$  axial resolution (in air).

Figure III-14 shows a corrected quantitative flow map (in terms of velocity) of the tomogram from Figure III-13. It is now possible to extract flow profiles along the indicated cross sections through the four vessels A-D of Figure III-14. For speckle reduction an averaging filter with a  $5 \times 5$ -kernel was applied to the selected regions. The profile of vessel C has a flat top at  $8.3\text{mm/s}$  since we hit the MPA limitation. The velocities in the central region of vessel C are too fast to be properly detected by at least two channels and quantitatively analyzed. The velocity calculation does not take into account any velocity offset due to proband motion. This explains the offset of the profile of vessel D with velocity peak value of  $-3.4\text{mm/s}$  and the sign change towards the edges of the vessel which is also visible for vessel A. The maximum velocity of vessel A is measured to be  $5.2\text{mm/s}$ , whereas vessel D is at  $-5.1\text{mm/s}$ . According to Figure III-7(b), and assuming a typical  $\text{SNR}$  of  $18.4\text{dB}$  in our tomogram with dynamic range of  $39\text{dB}$ , the velocity error is  $\pm 550\mu\text{m/s}$ .

Applying vertical scanning, we finally recorded a full 3D data set of the ONH region where we have a typical loss of flow signals due to the presence of high flow velocities. Like before, the data set consists of 2250 transverse points covering an angle of  $7^\circ$  on the retina. Again we applied the three-stage EOM phase switching resulting in a threefold interlaced 3D data set. The voltage slopes were set to  $\pm 9.1\text{V}/\mu\text{s}$  in order to maximally contrast the vascular against the static structure for a 3D vessel sectioning. Each of the three sub-tomograms has 750 transverse points. A set of 81 tomograms was recorded vertically along a range of  $4^\circ$ . The 3D



data set was recorded in 10.7s. As for the previous measurement, motion artifacts are corrected by image registration.



**Figure III-14. (lhs) Velocity map obtained by differential analysis of Figure III-13. with zoomed and average-filtered ROIs of vessel regions. (rhs) Velocity profiles extracted along the indicated lines in the vessel regions.**

We calculated the  $z$ -projection of each 3D data channel and merged the resulting fundus images corresponding to the standard FDOCT image projection and the two reference phase shifted copies as RGB entries, resulting in Figure III-15(a). The RGB fundus image allows immediately distinction between opposite axial flow directions. A clear differentiation between arterial and venous blood flow can only be found by looking to the 3D reconstruction of the ONH vessel structure displayed in Figure III-15(b). The EOM allows not only dimming the static structure leaving only the vascular structure but also separating opposite flow. We reconstructed individual 3D images for both the positively and negatively shifted channels. The two 3D rendered structures were afterwards colored in red and blue respectively and merged into the 3D image sequence of Figure III-15(b). From this representation it is directly possible to identify points at which vessels change their orientation with respect to the optical axis.

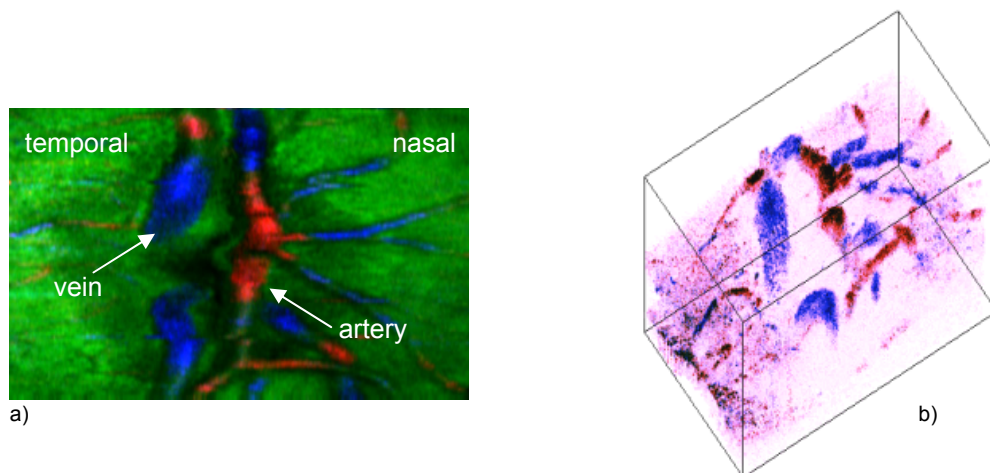


**Figure III-15. (a) RGB fundus image showing different axial flow directions in blue and red, and the static structure in green. Size:  $2.4\text{mm} \times 1.7\text{mm}$ . (b) (Movie: 2.5 MB) Movie of merged 3D volumes of positively and negatively shifted data sets in red and blue respectively. Tomogram size:  $2.4\text{mm} \times 1.7\text{mm} \times 1.1\text{mm}$  (length  $\times$  width  $\times$  depth) with  $8.5\mu\text{m}$  axial resolution (in air). Multimedia file is available on OpticsInfoBase at: <http://www.opticsinfobase.org/abstract.cfm?URI=oe-15-2-408>.**

Together with the color encoded directional information we have an unambiguous identification of an artery as the vessel that lead blood flow up from the nerve head channel to the retina, and the veins which transport the blood downwards the optical nerve (Figure III-15). For better contrast we combined both phase shifted channels to form a monochrome 3D image and displayed it in Figure III-16 as anaglyph stereo representation. This image, viewed through red-cyan filter goggles, gives a clear spatial impression of the vascular structure in the ONH region. Note also the fine vessel structure on the temporal side.

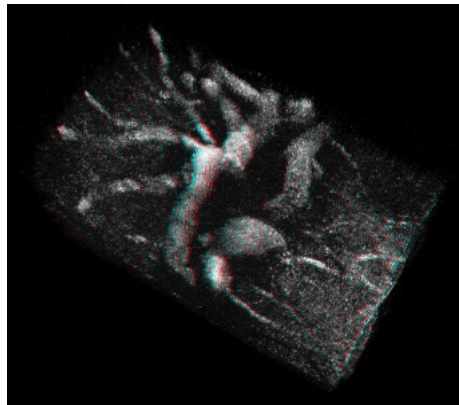


**Figure III-16.** (Movie: 3.6 MB) ONH blood vessel structure of Figure III-15 in an anaglyph stereo representation (red-cyan goggles). Multimedia file is available on OpticsInfoBase at: <http://www.opticsinfobase.org/abstract.cfm?URI=oe-15-2-408>.

The method of intensity based flow detection and optical vessel vivisection works well for large sample velocities as is the case in the ONH region, since the static structure will be strongly attenuated due to the large shift of the signal attenuation curve  $\mathcal{A}$  in Figure III-6(b). Nevertheless, this shift will also have an adverse effect on signals of flow at low speed. Tuning the EOM phase shift to these small flow velocities would result in only a weak static signal reduction, not sufficient anymore for an easy vessel sectioning. This is particularly the case if one approaches the foveal region.

## 8.5 Conclusion

In this chapter we established the theory of resonant Doppler imaging with spectrometer-based FDOCT and demonstrated its feasibility with the extraction of *in-vivo* retinal blood flow in 3D, *i.e.* optical vivisection of vascularization. With resonant Doppler flow imaging flow velocity values could be measured simply on the intensity basis without the need to extract the signal phase. This method has an increased velocity detection range compared to phase sensitive Doppler imaging. In addition, the use of a programmable EOM offers the flexibility, within its specifications, to tune the system sensitivity to arbitrary flow velocities independent of the CCD detector speed.



## Chapter 9

### Outlook on optical testing of retinal physiology

#### 9.1 Introduction

In the previous chapter resonant Doppler FDOCT, a novel spectrometer-based FDOCT modality, was presented. This system is capable to image preferentially the “moving” particles, *i.e.* to overcome the signal wash out of moving scatterers, and absolute flow measurements in an extended velocity range becomes possible. Studies of retinal perfusion using laser Doppler flowmetry (LDF) demonstrated high sensitivity of blood flow to external stimuli. The aim of this chapter is to present an extension of our FDOCT concept towards optical testing of retinal physiology by stimulating the eye using light flicker. The resonant Doppler FDOCT scheme will be used for the flow measurement.

#### 9.2 Short review on light flicker stimulation

Many retina mechanisms and the pathogenesis of important retinal diseases are not understood completely yet. It has already been shown that light stimulation in the visible spectrum can provoke retinal physiological reactions, measurable in function of time, such as vasodilatation, chorioretinal oxygen tension or blood flow in arterioles near the optic nerve head. It has been shown by Nagel *et al.* that light flicker stimulation induces a diameter change in human retinal arterioles [37]. Seifert *et al.* performed measurements using a *retinal vessel analyser* [38] which estimates vessel diameters by taking fundus images. Images were taken continuously before, during and after 20s of stimulation. The maximally induced dilatation was +7.4%. Using the same method, Gugleta *et al.* compared dilatation of arterioles in healthy and vasospastic persons (constriction of blood vessels resulting in a decrease in blood flow, a common symptom are cold hands). Healthy people presented maximum dilatory amplitude of about 8% [39]. The relation between flicker frequency (from 2 to 64Hz) and vessel dilatation in the living human retina was investigated by Polak *et al.* [40]. The peak amplitudes were found between 4Hz and 40Hz, without noticing a frequency with pronounced efficiency.

Oxygen tension in rats’ retinal and choroidal vasculatures in response to light flicker was studied by Shakoob *et al.* using phosphorescence imaging [41]. Measurements were taken before and during light flicker with frequencies ranging from 0Hz to 14Hz (2min of stimulation), located within one optic disk diameter from the edge of the optic nerve head. A significant increase in oxygen tension in the retinal arteries and capillaries has been demonstrated, veins on the other hand did not show noticeable changes. Oxygen tension is linked to blood flow: an increase in blood flow responds to a growth in oxygen consumption. Finally, Michelson *et al.* reported on blood flow increase of about 46% by a 30s stimulation at

8Hz and observed by phosphorescence imaging [42]. In addition, a dependency of this reaction on the stimulation location is speculated.

The relation between flow and retinal vessel diameter is very complex. The flow is at least a two-phase flow (red blood cells in blood plasma) and highly pulsatile, as known from human blood circulation. From literature one can assume that flow changes are more pronounced and therefore easier to observe than changes in diameter of retinal blood vessels.

### 9.3 Light flicker stimulation

The flicker source consists of three electroluminescent diodes (LED), coupled into a multi-mode (MM) fiber, each characterized by a different emission spectrum (red, green and blue). The different colors are combined using dichroic mirrors (Edmund Optics) with corresponding reflection and transmission characteristics (see Figure III-17).

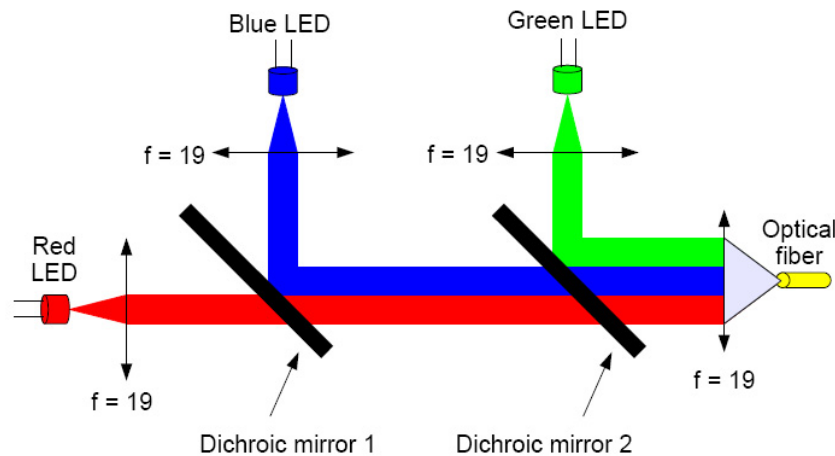


**Figure III-17. RGB light source scheme. Focal lengths in [mm].**

This system offers a wide choice of colors for the resulting beam by adjusting the power of each component (R,G,B), depending on the current driving each LED. The resulting color is delivered to the OCT system with the MM fiber. The delivered power scales with the fiber core surface. A 200 $\mu$ m step index fiber was chosen.

The RGB light source is easily controllable via a National Instruments data acquisition board (NI DAQ) (PCI-6030E) and a self-made LED controller box (RGB box) (see Figure III-18). The NI DAQ drives two different analogue voltage outputs and reads at the same time analogue voltages delivered by the RGB Box. This feedback loop gives accurate control of the power, the frequency and the spectrum of the light produced by the RGB source.

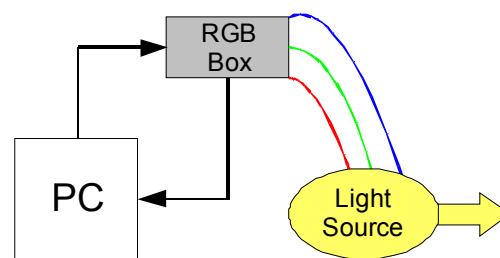


**Figure III-18. Data connection scheme for RGB source control.**



## 9.4 Measurements

The performed flicker light stimulation measurements aimed to show an effect of flicker light on retinal vessel diameter and blood flow velocity, close to the optic nerve head. To prevent the subject's head from moving during data recording, the proband used a bite bar for optimal fixation. The following measurements were performed by resonant Doppler FDOCT (see also Chapter 8).

The experimental settings were chosen in accordance with previously published studies (see §9.2). White light frequency and power were set to 10Hz and  $12\mu W$  respectively. The flicker light was imaged to the eye via two lenses in order to adjust the illumination area on the retina to a viewing angle of  $30^\circ$ , corresponding to an area of  $78mm^2$ . This leads to an irradiance of  $85mW/m^2$ , which is safe for the eye in accordance to ANSI safety standards [35].

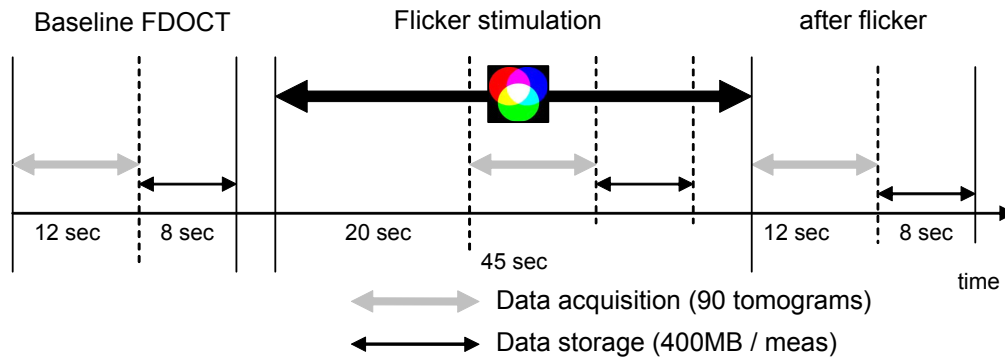


**Figure III-19. Blood flow measurement protocol for flicker stimulation. See text for details.**

The measurement protocol is shown in Figure III-19. First, a series of 90 tomograms at the same vertical position was acquired. This procedure took 12s and another 8s were needed for saving the recorded data. Flicker stimulation lasted 45s and a time series was acquired 20s after its start. The vertical position could be identified by recording a 3D volume and calculating the projection of the data along the depth axis in order to calculate the fundus image (see Figure III-20(a)). Directly after flicker stimulation additional acquisitions of 90 tomograms were recorded.

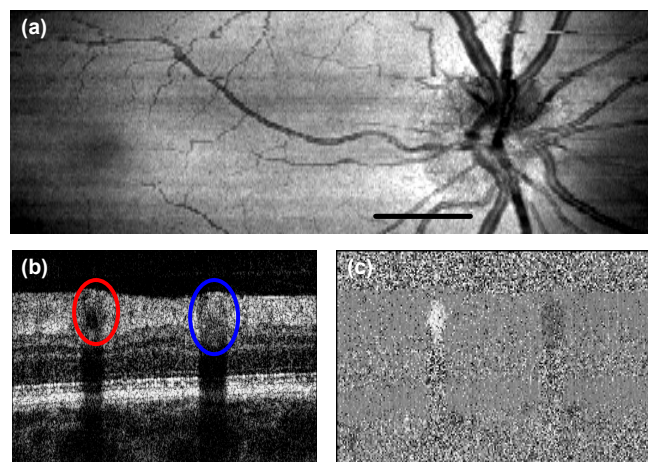


**Figure III-20: (a) z-projection of 3D FDOCT data ("fundus image"). The solid black line indicates the selected region of interest. (b) Tomogram at the indicated region in (a). (c) Doppler velocity image of indicated region in (a).**

Figure III-20(b) shows an intensity tomogram of an acquired time series before flicker stimulation and in Figure III-20(c) its Doppler image is displayed. By analyzing the flow velocity maximum within the vessel we observe a strong pulsatility of the left vessel in Figure III-20(b), whereas the right vessel shows only small pulsatility. Accordingly we believe that the left vessel is an artery and the right one a vein (see Figure III-21).

For removal of residual motion artifact we calculated the histogram of the Doppler tomogram. The maximum of the histogram was then used as negative offset to the actual determined velocity values within the vessels. The Doppler tomogram was post-processed using a 5x5 median filter for speckle reduction. For evaluation we had chosen data blocks with almost no motion artifacts.

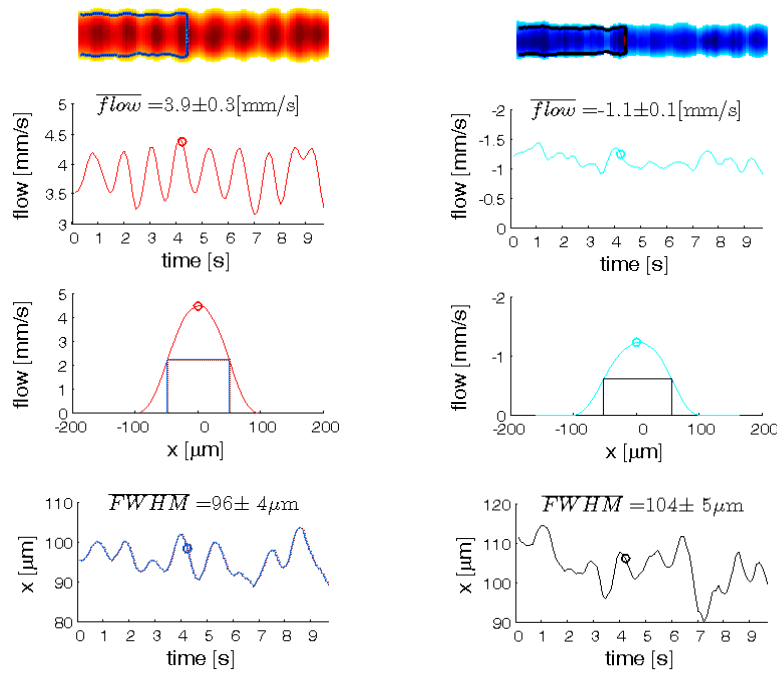


**Figure III-21. Pulsatility of blood vessels. Isolating vessels in the Doppler tomogram (Figure III-20(c)) gives access to vessel diameter and flow profile. (lhs) artery, (rhs) vein. Measurement before flicker stimulation.**

The analysis of our first experiments according to the protocol above is displayed in Figure III-22. It shows an +49% increase of the flow velocity maximum during flicker stimulation whereas the vessel diameter increased by +11%. Nevertheless, the diameter shows strong fluctuations in the image after flicker. Therefore the more reliable parameter is seen to be the actual flow velocity as it was expected according to §9.2. These preliminary results are in good agreement with previous findings using LDF, but for statistically significant results measurements on a larger amount of subjects need be performed in order to prove correlation between flicker stimulation and blood flow changes.

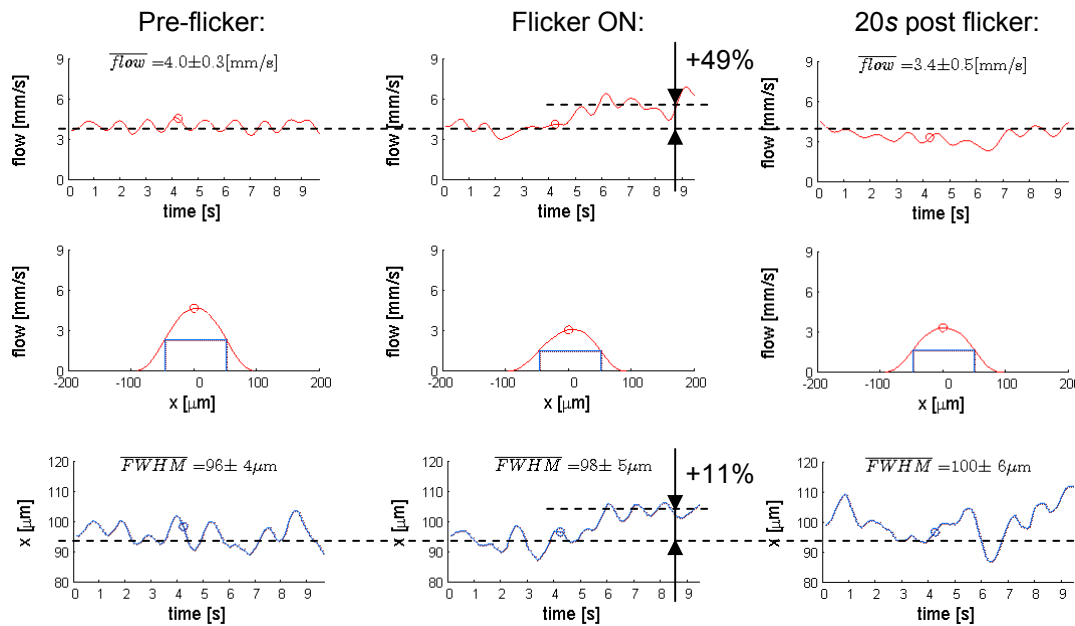


**Figure III-22. Resulting effect of flicker stimulation on flow velocity and vessel diameter. Preliminary results.**

## 9.5 Conclusion

In this chapter we implemented a platform based on high resolution and high speed FDOCT to probe physiologic parameters of the human retina. First experiments were performed to study the response of retinal perfusion on flicker stimulation with FDOCT. The results demonstrate the high sensitivity of the flow measurement allowing measuring an increase of blood flow of up to 49%, with an increase of vessel diameter of 11%. We believe that insight into functional parameters and thus into retinal physiology and metabolism will give valuable and unique information to help a better understanding of various retinal pathologies and their pathogenesis. Further measurements need to be performed for statistically significant results.

### References:

1. R. J. Zawadzki, S. M. Jones, S. S. Olivier, M. T. Zhao, B. A. Bower, J. A. Izatt, S. Choi, S. Laut, and J. S. Werner, "Adaptive-optics optical coherence tomography for high-resolution and high-speed 3D retinal in vivo imaging," *Opt. Express* **13**, 8532-8546 (2005).
2. M. F. Bear, M. A. Connors, and M. A. Paradiso, *Neurosciences: à la découverte du cerveau* (Editions Pradel, 2002).
3. D. H. Pritchard, "U. S. COLOR TELEVISION FUNDAMENTALS - A REVIEW," *RCA engineer* **29**, 15-26 (1984).
4. R. Leitgeb, L. Schmetterer, W. Drexler, F. Berisha, C. Hitzenberger, M. Wojtkowski, T. Bajraszewski, and A. F. Fercher, "Real-time measurement of in-vitro and in-vivo blood flow with Fourier domain optical coherence tomography," in *Coherence Domain Optical Methods And Optical Coherence Tomography In Biomedicine Viii*(Spie-Int Society Optical Engineering, Bellingham, 2004), pp. 141-146.
5. M. Wojtkowski, V. Srinivasan, J. G. Fujimoto, T. Ko, J. S. Schuman, A. Kowalczyk, and J. S. Duker, "Three-dimensional retinal imaging with high-speed ultrahigh-resolution optical coherence tomography," *Ophthalmology* **112**, 1734-1746 (2005).
6. U. Schmidt-Erfurth, R. A. Leitgeb, S. Michels, B. Povazay, S. Sacu, B. Hermann, C. Ahlers, H. Sattmann, C. Scholda, A. F. Fercher, and W. Drexler, "Three-dimensional ultrahigh-resolution optical coherence tomography of macular diseases," *Invest Ophthalmol Vis Sci* **46**, 3393-3402 (2005).
7. E. Gotzinger, M. Pircher, and C. K. Hitzenberger, "High speed spectral domain polarization sensitive optical coherence tomography of the human retina," *Opt. Express* **13**, 10217-10229 (2005).

8. Y. Yasuno, S. Makita, Y. Sutoh, M. Itoh, and T. Yatagai, "Birefringence imaging of human skin by polarization-sensitive spectral interferometric optical coherence tomography," *Opt. Lett.* **27**, 1803-1805 (2002).
9. B. H. Park, M. C. Pierce, B. Cense, S. H. Yun, M. Mujat, G. J. Tearney, B. E. Bouma, and J. F. de Boer, "Real-time fiber-based multi-functional spectral-domain optical coherence tomography at 1.3  $\mu\text{m}$ ," *Opt. Express* **13**, 3931-3944 (2005).
10. S. Makita, Y. Hong, M. Yamanari, T. Yatagai, and Y. Yasuno, "Optical coherence angiography," *Opt. Express* **14**, 7821-7840 (2006).
11. R. A. Leitgeb, L. Schmetterer, C. K. Hitzenberger, A. F. Fercher, F. Berisha, M. Wojtkowski, and T. Bajraszewski, "Real-time measurement of in vitro flow by Fourier-domain color Doppler optical coherence tomography," *Opt. Lett.* **29**, 171-173 (2004).
12. R. A. Leitgeb, L. Schmetterer, W. Drexler, A. F. Fercher, R. J. Zawadzki, and T. Bajraszewski, "Real-time assessment of retinal blood flow with ultrafast acquisition by color Doppler Fourier domain optical coherence tomography," *Opt. Express* **11**, 3116-3121 (2003).
13. B. R. White, M. C. Pierce, N. Nassif, B. Cense, B. H. Park, G. J. Tearney, B. E. Bouma, T. C. Chen, and J. F. de Boer, "In vivo dynamic human retinal blood flow imaging using ultra-high-speed spectral domain optical Doppler tomography," *Opt. Express* **11**, 3490-3497 (2003).
14. R. Leitgeb, M. Wojtkowski, A. Kowalczyk, C. K. Hitzenberger, M. Sticker, and A. F. Fercher, "Spectral measurement of absorption by spectroscopic frequency-domain optical coherence tomography," *Opt. Lett.* **25**, 820-822 (2000).
15. R. A. Leitgeb, W. Drexler, B. Povazay, B. Hermann, H. Sattmann, and A. F. Fercher, "Spectroscopic Fourier domain optical coherence tomography: Principle, limitations, and applications," in *Progress in Biomedical Optics and Imaging - Proceedings of SPIE*(2005), pp. 151-158.
16. R. A. Leitgeb, A. H. Bachmann, M. L. Villiger, C. Blatter, T. Lasser, and M. Pircher, "Measurement of retinal physiology using functional Fourier domain OCT concepts," in *Coherence Domain Optical Methods and Optical Coherence Tomography in Biomedicine XI*(SPIE, San Jose, 2007).
17. J. Flammer, S. Orgul, V. P. Costa, N. Orzalesi, G. K. Kriegelstein, L. M. Serra, V. X. Renard, and E. Stefansson, "The impact of ocular blood flow in glaucoma," *Prog. Retin. Eye Res* **21**, 359-393 (2002).
18. L. Schmetterer, and M. Wolzt, "Ocular blood flow and associated functional deviations in diabetic retinopathy," *Diabetologia* **42**, 387-405 (1999).
19. C. E. Riva, S. D. Cranston, J. E. Grunwald, and B. L. Petrig, "Choroidal blood flow in the foveal region of the human disc," *Invest. Ophthalmol. Vis. Sci.* **35**, 4273-4281 (1994).
20. C. E. Riva, J. E. Grunwald, S. H. Sinclair, and B. L. Petrig, "Blood velocity and volumetric flow rate in human retinal vessels," *Invest. Ophthalmol. Vis. Sci.* **26**, 1124-1132 (1985).
21. E. Friedman, "A hemodynamic model of the pathogenesis of age-related macular degeneration," *Am. J. Ophthalmol.* **124**, 677-682 (1997).
22. H. A. Quigley, "Number of people with glaucoma worldwide," *British Journal of Ophthalmology* **80**, 389-393 (1996).
23. R. Klein, B. E. K. Klein, and S. E. Moss, "The Wisconsin Epidemiologic Study of Diabetic Retinopathy. II. Prevalence and risk of diabetic retinopathy when age at diagnosis is less than 30 years," *Archives of Ophthalmology* **102**, 520-526 (1984).
24. S. Yazdanfar, A. M. Rollins, and J. Izatt, "In vivo imaging of human retinal flow dynamics by color Doppler optical coherence tomography," *Arch. Ophthalmol.* **121**, 235-239 (2003).
25. Y. Zhao, Z. Chen, C. Saxer, S. Xiang, J. F. De Boer, and J. S. Nelson, "Phase-resolved optical coherence tomography and optical Doppler tomography for imaging blood flow in human skin with fast scanning speed and high velocity sensitivity," *Opt. Lett.* **25**, 114-116 (2000).
26. R. K. Wang, S. L. Jacques, Z. Ma, S. Hurst, S. R. Hanson, and A. Gruber, "Three dimensional optical angiography," *Opt. Express* **15**, 4083-4097 (2007).
27. K. Bizheva, R. Pflug, B. Hermann, B. Povazay, H. Sattmann, P. Qiu, E. Anger, H. Reitsamer, S. Popov, J. R. Taylor, A. Unterhuber, P. Ahnelt, and W. Drexler, "Optophysiology: Depth-resolved probing of retinal physiology with functional ultrahigh-resolution optical coherence tomography," *Proceedings Of The National Academy Of Sciences Of The United States Of America* **103**, 5066-5071 (2006).
28. B. A. Bower, M. Zhao, and J. A. Izatt, "Investigation of retinal vessel autoregulation using real-time spectral domain doppler optical coherence tomography," in *Proceedings of SPIE - The International Society for Optical Engineering*(2006).
29. J. W. You, T. C. Chen, M. Mujat, B. H. Park, and J. F. de Boer, "Pulsed illumination spectral-domain optical coherence tomography for human retinal imaging," *Opt. Express* **14**, 6739-6748 (2006).
30. J. K. Barton, and S. Stromski, "Flow measurement without phase information in optical coherence tomography images," *Opt. Express* **13**, 5234-5239 (2005).

31. S. H. Yun, G. J. Tearney, J. F. de Boer, and B. E. Bouma, "Motion artifacts in optical coherence tomography with frequency-domain ranging," *Opt. Express* **12**, 2977-2998 (2004).
32. A. H. Bachmann, R. A. Leitgeb, and T. Lasser, "Heterodyne Fourier domain optical coherence tomography for full range probing with high axial resolution," *Opt. Express* **14**, 1487-1496 (2006).
33. R. Leitgeb, L. Schmetterer, M. Wojtkowski, C. K. Hitzenberger, M. Stricker, and A. F. Fercher, "Flow Velocity Measurement by Frequency Domain Short Coherence Interferometry," in *Coherence Domain Optical Methods And Optical Coherence Tomography In Biomedicine VI*(2002), pp. 16-21.
34. R. Michaely, A. H. Bachmann, M. L. Villiger, C. Blatter, T. Lasser, and R. A. Leitgeb, "Vectorial retinal blood flow in 3D using high resolution resonant Doppler FDOCT," submitted to *J Biomed Opt*, accepted for publication (2007).
35. A. N. S. Institute, "American National Standards for Safe Use of Lasers, ANSI Z.136.1 " (2000).
36. P. Thevenaz, U. E. Ruttimann, and M. Unser, "A Pyramid Approach to Subpixel Registration Based on Intensity," *IEEE Transaction On Image Processing* **7**, 27-41 (1998).
37. E. Nagel, and W. Vilser, "Flicker observation light induces diameter response in retinal arterioles: A clinical methodological study," *British Journal of Ophthalmology* **88**, 54-56 (2004).
38. B. U. Seifert, and W. Vilser, "Retinal Vessel Analyzer (RVA) - Design and Function," *Biomed Tech* **47** (2002).
39. K. Gugleta, C. Zawinka, I. Rickenbacher, A. Kochkorov, R. Katamay, J. Flammer, and S. Orgul, "Analysis of retinal vasodilation after flicker light stimulation in relation to vasospastic propensity," *Investigative Ophthalmology and Visual Science* **47**, 4034-4041 (2006).
40. K. Polak, L. Schmetterer, and C. E. Riva, "Influence of flicker frequency on flicker-induced changes of retinal vessel diameter," *Investigative Ophthalmology and Visual Science* **43**, 2721-2726 (2002).
41. A. Shakoor, N. P. Blair, M. Mori, and M. Shahidi, "Chorioretinal vascular oxygen tension changes in response to light flicker," *Investigative Ophthalmology and Visual Science* **47**, 4962-4965 (2006).
42. G. Michelson, A. Patzelt, and J. Harazny, "Flickering light increases retinal blood flow," *Retina* **22**, 336-343 (2002).



## **Part IV**

### **Conclusion and outlook**





## Chapter 10

### Conclusion

This thesis proposes two new spectrometer-based FDOCT modalities, both based on the phase-sensitive nature of OCT. Appropriate locking of acquisition speed, exposure time and triggering onto the induced signal phase changes leads to additional degrees of freedom in signal detection. Such concepts were applied to biological and non-biological samples.

In Chapter 3 in Part II the spectrometer-based heterodyne FDOCT was presented and discussed. *Iv-vivo* measurements demonstrated the suppression of FDOCT-inherent artifacts like complex mirror terms due to full complex signal reconstruction by quadrature detection of a stable beating frequency at 20'000 depth-scans per second using integrating buckets. The beating frequency is generated by two AOFS and is wavelength-independent; therefore no mirror terms interfere with the actual structure terms even if large bandwidth sources are employed. A novel differential complex reconstruction algorithm was proposed and applied showing efficient elimination of DC and autocorrelation terms. This achromatic, heterodyne spectrometer-based FDOCT system would reach its full potential once combined with a true heterodyne detector performing the signal demodulation for each pixel on-chip instead of the integrating bucket approach as in the presented case. First concepts for such detectors are discussed in literature [1, 2].

The limit in the spectral transmittance bandwidth was identified as the key limiting factor for achieving ultra-high resolution tomograms, motivating the development of truly broadband acousto-optic frequency shifters which allows improved fiberization. Design and realization of such devices was discussed in detail in Chapter 4. It was shown that the spectral transmission bandwidth can be increased to more than an octave by employing appropriate dispersion prisms to compensate for the dispersion induced by the frequency shifting devices; this also improves the Bragg condition matching. Two prototypes used with a titanium sapphire laser were realized and tested. Spectral bandwidth increase was clearly shown while intensity losses still need to be decreased by proper AR coatings.

In Chapter 5 dual beam FDOCT was introduced allowing for phase sensitive measurements even through long probing fibers and employing manual applicators. A detailed theoretical analysis of sensitivity and dynamic range capabilities of a dual beam configuration was presented showing a -6dB decline in sensitivity for an equal dynamic range as compared to standard FDOCT. Even though the dual beam concept is equally suitable for swept source and spectrometer-based FDOCT, the method was only tested using the spectrometer-based FDOCT. Employing two different applicators with a single mirror tip/tilt scanner, *iv-vivo* measurements on human skin were performed, and using a custom-made esophagoscope *ex-vivo* measurements were demonstrated on porcine esophagus. The measurements are in good agreement with theoretical findings concerning SNR and dynamic range.

In Chapter 6 phase stability issues with respect to the complex signal reconstruction algorithms used were discussed in order to conclude Part II of this thesis. It was shown that amplitude errors are equally disturbing as phase errors. The speckle structure of a diffuse (*e.g.* biological) sample is mainly responsible for these local intensity fluctuations. The established model shows that pure phase errors represent a lower limit (best case) for complex mirror term artifact suppression. The model could be experimentally verified, proving that  $\pm 3.6^\circ$  and  $\pm 1.2^\circ$  phase error is tolerable for  $-30\text{dB}$  and  $-40\text{dB}$  mirror term suppression respectively. In the same chapter a novel reconstruction algorithm proposed by Wang [3] was tested and compared to the one used in Chapters 3 and 5 of this thesis. Improved – but still not complete – mirror term suppression could be observed.

In Part III an expansion from structural to functional imaging was given. After a brief introduction to functional imaging in FDOCT in Chapter 7, a novel signal recovery scheme for avoiding interference fringe blurring was introduced in Chapter 8: resonant Doppler FDOCT. We established the theory of resonant Doppler imaging with spectrometer-based FDOCT and demonstrated its feasibility for the extraction of *iv-vivo* retinal blood flow in 3D, *i.e.* optical vivisection of vascularization. The advantage of the resonant Doppler flow imaging modality is the possibility of achieving flow extraction on a pure intensity basis. This method has an improved velocity detection range as compared to phase sensitive color Doppler imaging. In addition, the use of a programmable EOM has the flexibility, within its specifications, to tune the system sensitivity to arbitrary flow velocities independent of the CCD detector speed.

In Chapter 9 a short outlook on probing retinal physiology by observing blood flow changes was given. Literature on flicker light in combination with vaso-mechanical reactions is reviewed concluding on the measurement protocol we are currently employing in order to study physiological changes in the human retina *iv vivo*. Physiological studies are in general delicate and need statistically relevant numbers of subjects to be measured. However, first preliminary results could be presented.

## Chapter 11

### Outlook

*“There are questions without answers, but also answers without a question.”*  
“Dorian Gray” by Oscar Wilde

As with any other scientific work, this thesis resolves a certain number of issues but unearths many new questions for further investigation as well.

The heterodyne spectrometer-based FDOCT with achromatic phase shifting proved to deliver a superior performance and the residual complex signal reconstruction errors were found to be mainly due to sample speckle statistics and related signal phase and amplitude errors. In order to decrease these errors, high over sampling is required while scanning. A very recently published novel reconstruction algorithm [3] proves to be significantly less sensitive to phase errors, including chromatic phase errors. Especially with faster line or true heterodyne line detectors, heterodyne spectrometer-based FDOCT should attract additional interest.

The presented dual beam concept for FDOCT allows for phase sensitive measurements with applicators even if connected via long probing fibers. Dual beam FDOCT does not require heterodyne or other phase shifting techniques, however it might be less useful if not used in conjunction with them. Especially for an algorithm such as that presented by Wang [3], a dual beam concept could be of great interest since this algorithm fails if phase fluctuations deflect the frequency-shifted signal too far away from the induced carrier frequency towards and beyond the zero frequency. A dual beam configuration would prevent such strong fluctuations for the fiber-related portion and the system would remain more reliable.

Surprisingly, not much effort in signal processing has been made within the OCT community and publications like [3, 4] and [5, 6] might show *one* of the new trends: developing novel algorithms for exploiting the information of the detected signal to its maximum. The author of this thesis is convinced that more information is buried within the detected signal than is currently extracted for most cases. However, such algorithms might need even better understanding of the rather complex manner in which the detected signal is generated when taking into account speckle effects. More investigation in this direction should therefore be conducted.

Without any doubt OCT owes its growing interest to ophthalmology and its unique position within this important biomedical field. FDOCT fledged rapidly during recent years and research will drift towards specific applications of OCT in general and functional imaging in biological samples in particular. The combination of different imaging technologies increases the potential of each method involved and is therefore of great interest for further research [7-13].

**References:**

1. S. Bourquin, P. Seitz, and R. P. Salathe, "Two-dimensional smart detector array for interferometric applications," *Electron. Lett.* **37**, 975-976 (2001).
2. S. Beer, P. Zeller, N. Blanc, F. Lustenberger, and P. Seitz, "Smart pixels for real-time optical coherence tomography," in *Proceedings of SPIE - The International Society for Optical Engineering* (2004), pp. 21-32.
3. R. K. Wang, "In vivo full range complex Fourier domain optical coherence tomography," *Appl. Phys. Lett.* **90** (2007).
4. M. V. Sarunic, B. E. Applegate, and J. A. Izatt, "Real-time quadrature projection complex conjugate resolved Fourier domain optical coherence tomography," *Opt. Lett.* **31**, 2426-2428 (2006).
5. T. S. Ralston, D. L. Marks, S. A. Boppart, and P. Scott Carney, "Inverse scattering for high-resolution interferometric microscopy," *Opt. Lett.* **31**, 3585-3587 (2006).
6. T. S. Ralston, D. L. Marks, P. S. Carney, and S. A. Boppart, "Interferometric synthetic aperture microscopy," *Nature Physics* **3**, 129-134 (2007).
7. B. E. Applegate, C. Yang, and J. A. Izatt, "Theoretical comparison of the sensitivity of molecular contrast optical coherence tomography techniques," *Opt. Express* **13**, 8146-8163 (2005).
8. S. Yazdanfar, L. H. Laiho, and P. T. C. So, "Interferometric second harmonic generation microscopy," *Opt. Express* **12**, 2739-2745 (2004).
9. S. Tang, T. B. Krasieva, Z. Chen, and B. J. Tromberg, "Combined multiphoton microscopy and optical coherence tomography using a 12-fs broadband source," *J. Biomed. Opt.* **11** (2006).
10. E. Beaurepaire, L. Moreaux, F. Amblard, and J. Mertz, "Combined scanning optical coherence and two-photon-excited fluorescence microscopy," *Opt. Lett.* **24**, 969-971 (1999).
11. B. E. Applegate, and J. A. Izatt, "Molecular imaging of endogenous and exogenous chromophores using ground state recovery pump-probe optical coherence tomography," *Opt. Express* **14**, 9142-9155 (2006).
12. M. V. Sarunic, B. E. Applegate, and J. A. Izatt, "Spectral domain second-harmonic optical coherence tomography," *Opt. Lett.* **30**, 2391-2393 (2005).
13. K. D. Rao, M. A. Choma, S. Yazdanfar, A. M. Rollins, and J. A. Izatt, "Molecular contrast in optical coherence tomography by use of a pump-probe technique," *Opt. Lett.* **28**, 340-342 (2003).

## **Part V**

## **Addendum**



## A Glossary – acronyms and medical terms

AC	OCT structure signal/cross-correlation terms
AMD	Age related macula degeneration
ANSI	American National Standards Institute
AOFS	Acousto-optic frequency shifter
AR	Anti-reflective
BK7	Brand name for one type of crown glass from Schott
BS	Beam splitter
c.c.	Complex conjugate
CCD	Charged coupled device
CL	Camera lens
dB	Decibel
DC	Direct current/constant signal
DG	Diffraction grating
Disp	Dispersion compensation
DOE	Diffraction optical element
DR	Dynamic range
ELM	External limiting membrane
EOM	Electro-optic modulator
FDOCT	Fourier/spectral domain optical coherence tomography
FFT	Fast Fourier transform
FT	Fourier transform
FWHM	Full width at half maximum
ILS	Interferometric light source
INL	Inner nuclear layer
LCI	Low coherence interferometry
LDF	Laser Doppler flowmetry
LED	Electroluminescent diode
lhs	left hand side
LS	Light source
MM	Multi mode
MPA	Maximum possible attenuation
NA	Numerical aperture
NI DAQ	Data acquisition board from National Instruments Inc.
NIR	Near infrared spectral range
OCM	Optical coherence microscopy
OCT	Optical coherence tomography
ONH	Optic nerve head
ONL	Outer nuclear layer
OL	Objective lens
PC	Polarization control paddle

PM	Polarization maintaining
PR IS	Photoreceptor inner segment
PR OS	Photoreceptor outer segment
RGB	Red, green, blue
ROI	Region of interest
RPE	Retinal pigmented epithelium
SF6	Brand name for one type of flint glass from Schott
SLD	Superluminescent diode
SM	Single mode
SNR	Signal-to-noise ratio
TDOCT	Time domain optical coherence tomography
TE	Transverse electric
TeO <sub>2</sub>	Tellurium dioxide
Ti:S	Titanium sapphire
TS	Translation stage
VIS	Visible spectral range
Nasal	Towards the nose
Temporal	Towards the temple



## B List of figures

Figure I-1	Typical high resolution retinal tomogram with “empty” blood vessels in the optic nerve head region	3
Figure II-1	Retinal tomogram with strong mirror terms	18
Figure II-2	Simulation of complex FDOCT signal reconstruction with chromatic phase shifting (with no other phase errors present)	19
Figure II-3	The three plotted curves show the suppression ratio of P* (mirror term) with respect to P (signal peak) for three different central wavelengths of the light source depending on optical bandwidth ( $\lambda_0=550nm$ (blue), $\lambda_0=800nm$ (red), $\lambda_0=1300nm$ (green))	20
Figure II-4	Differential complex reconstruction. (a) beating signal; (b) camera trigger; (c) camera exposure; (d) brackets indicate the frames used for complex two-frame reconstruction	23
Figure II-5	Logarithmic spectral characteristics of the two pigtailed AOFS. The -3dB spectral transmittance is approximately 120nm	24
Figure II-6	Mach-Zehnder like interferometer comprising: fs-Ti:S light source (LS), 90:10 fiber coupler (FC), AOFS shifting the light fields by $\omega_{R,S}$ , translation stage (TS), dispersion compensation (Disp), 50:50 beamsplitter (BS), galvo scanners (X-Y scan), camera lens (CL)	25
Figure II-7	Synchronization scheme for heterodyne FDOCT. A common timebase is very important for relative frequency accuracy and long time stability	26
Figure II-8	Tomogram of a fingernail fold region with standard FDOCT and heterodyne FDOCT	27
Figure II-9	Tomogram of a fingertip with standard FDOCT and heterodyne FDOCT	27
Figure II-10	(a) Raman-Nath regime with multiple diffraction orders. (b) Bragg regime, crystal illuminated under the Bragg angle $\theta_B$	30
Figure II-11	Vector diagram (Ewald sphere construction) for the acousto-optic interaction resulting in a so-called <i>up-shift</i> . $k_{i,m}$ and $k_{d,m}$ : incident and diffracted optical wavevectors respectively	31
Figure II-12	(lhs) Diffraction efficiency of order 0 and +1 or -1 as a function of $\nu_{RN}$ in the case of Bragg regime. (rhs) Diffracted intensity $I_l$ and intensity in order zero $I_0$ for optimal interaction ( $\nu_{RN}=\pi$ ) as a function of the quality factor $Q$	32
Figure II-13	(lhs) vector diagram for interaction not satisfying the Bragg condition. See text for details. (rhs) Ewald sphere construction with broad bandwidth	32
Figure II-14	Normalized diffraction efficiency outside the Bragg condition for two different acoustic frequencies, with optimal interaction ( $\nu_{RN}=\pi$ )	33
Figure II-15	Anisotropic interaction	34
Figure II-16	Wavelength dependent angular spreading of the diffracted beam	35

Figure II-17	(a) Fix Bragg angle $\theta_B(\lambda_0)$ defining the incident beam angle and effective Bragg angle $\theta_B(\lambda)$ for an AOFS based on $\text{TeO}_2$ , $F=110\text{MHz}$ . (b) Angular error $\Delta\theta(\lambda)$	36
Figure II-18	(lhs) Generalized prism equation. (rhs) Deviation $\delta$ of a light beam	37
Figure II-19	(a) Bragg angle $\theta_B(\lambda)$ , output angle for the optimal prism apex $\theta_{\text{out,optimal}}(\lambda)$ , and $\theta_{\text{out},30}(\lambda)$ for BK7. (b) Angular error $\Delta\theta(\lambda)$ for curves in (a). Spectral range is NIR	39
Figure II-20	(a) Bragg angle $\theta_B(\lambda)$ , and output angle for the optimal prism apex $\theta_{\text{out,optimal}}(\lambda)$ for BK7. (b) Angular error $\Delta\theta(\lambda)$ for curves in (a). Spectral range is VIS and NIR	39
Figure II-21	Normalized spectral transmittance (diffraction efficiency) for calculated curves	40
Figure II-22	Symmetric system with respect to the AOFS longitudinal axis. The whole spectral output becomes collinear for perfectly matched Bragg condition	40
Figure II-23	Coupling into single mode fiber for ideally coaxial incidence and with angle	41
Figure II-24	coupling efficiency $C$ into single mode fiber for $f_c=3\text{mm}$ and standard dispersion prisms positioned in accordance to minimum deviation	41
Figure II-25	Total normalized spectral transmission for uncorrected and corrected cases	42
Figure II-26	Free spectral range is not limiting transmittance if angular correction with prisms is implemented	42
Figure II-27	Configuration with standard prisms. Several parameters can be adjusted resulting in optimized transmittance characteristics	43
Figure II-28	Calculated normalized transmittance curves for the standard prism configuration with optimized apex angle and orientation of prisms	43
Figure II-29	Configuration with achromatic prisms	44
Figure II-30	Calculated normalized transmittance curves for achromatic prism pairs	44
Figure II-31	Acousto-optic frequency shifter from AA Opto-Electronics without top cover	45
Figure II-32	Drawing of broadband fiberized AOFS with angular correction	46
Figure II-33	Normalized spectral transmittance for parameters as listed in Table II-7. The strong influence by the tilt of the coupling optics is well illustrated by the different curves	46
Figure II-34	Comparison of normalized transmittance of Brimrose Inc. AOFS and prototypes assembled at the Cube Optics facility in Mainz	47
Figure II-35	Concept of a common path configuration	50
Figure II-36	Dual beam principle	51
Figure II-37	Scheme illustrating the filling of a camera pixel in case of dual beam and classical FDOCT respectively	54
Figure II-38	Dual beam heterodyne FDOCT setup	56
Figure II-39	Hand held probe with: (a) single mirror tip/tilt scanner	57
Figure II-40	Sectional drawings of rigid esophagoscope design for use with dual beam heterodyne FDOCT	58
Figure II-41	Picture of designed and manufactured rigid esophagoscope	59
Figure II-42	Time sequence of 500 depth scans per tomogram for phase stability measurement and comparison between dual beam and standard FDOCT	60
Figure II-43	Tomogram of human fingertip with sweat gland	61
Figure II-44	3D Tomogram of human finger tip	61
Figure II-45	Tomogram of porcine esophagus <i>ex vivo</i> , consisting of 15'400 lines with 10.5x over-sampling	62

Figure II-46	Tomogram of porcine esophagus <i>ex vivo</i> , consisting of 20'000 lines with 13.6x over-sampling	63
Figure II-47	ROI. (rhs). Circle-like residual mirror structures are visible in the lower left direction of the structure	63
Figure II-48	Complex signal reconstruction before or after FFT with equivalent result	65
Figure II-49	Cosine modulation on spectrometer representing one reflecting sample surface, without DC term	66
Figure II-50	Complex phasors after FFT of a cosine function, representing a positive (bin $N_0$ ) and negative frequency (bin $-N_0$ )	66
Figure II-51	Complex phasors in 2D for two conjugated Fourier bins after FFT	67
Figure II-52	Mirror term suppression ratio as function of relative amplitude errors and relative phase errors	68
Figure II-53	Complex reconstructed tomogram of mirror surface with induced phase errors	69
Figure II-54	(lhs) Relative amplitude errors are small on a reflecting surface. (rhs) Relative phase errors cause insufficient mirror term suppression	69
Figure II-55	Mirror term suppression ratio of tomogram with fluctuating phase shift	69
Figure II-56	Complex reconstructed tomogram of a piece of paper. Phase errors are induced by fast scanning	70
Figure II-57	Important relative amplitude (lhs) and phase errors (rhs)	70
Figure II-58	Mirror terms suppression ratio in accordance to measurements shown in	71
Figure II-59	Tomogram using the reconstruction algorithm proposed by Wang	71
Figure II-60	Mirror terms suppression ratio for tomogram reconstructed using Wang's algorithm	72
Figure II-61	Tomogram using (a): complex reconstruction in accordance to Equation (II.4); (b): differential complex reconstruction scheme (Equation (II.5)); (c): Wang's reconstruction algorithm. (d) Suppression difference (c)-(a), revealing improved mirror term suppression using Hilbert transform prior to Fourier transform	73
Figure III-1	Fundus image of healthy retina	79
Figure III-2	Histology of retinal layers	80
Figure III-3	Distribution of rods and cones on a human retina	81
Figure III-4	Typical high resolution retinal tomogram with "empty" blood vessels	82
Figure III-5	Normalized signal attenuation $\mathcal{A}$ as a function of $\Delta z$ , the displacement of a sample surface during the integration time, and $z$ , the axial coordinate in $dB$	88
Figure III-6	(a) Maximum value in $z$ -direction of the normalized signal attenuation $\mathcal{A}$ as a function of displacement $\Delta z$ . (b) $\mathcal{A}$ as a function of sample velocity for the static case (solid line) and with a reference velocity offset $v_s$ (dashed line).	88
Figure III-7	(a) Signal attenuation $\mathcal{A}$ and (b) velocity as a function of the quotient $\Delta\mathcal{A}$	89
Figure III-8	Optical setup for resonant Doppler FDOCT	92
Figure III-9	Synchronization scheme for resonant Doppler FDOCT	93
Figure III-10	Normalized signal attenuation $\mathcal{A}$ for different samples due to the applied EOM phase slope	94
Figure III-11	Time sequence (after registration) with a three-stage EOM signal applied showing the same vertical position on the retina with stepwise increasing EOM voltage	95
Figure III-12	Time sequence. Figure III-11(a-c) in RGB representation	96

Figure III-13	Velocity determination by unambiguous differential velocity mapping	97
Figure III-14	(lhs) Velocity map obtained by differential analysis with zoomed and average-filtered ROIs of vessel regions. (rhs) Velocity profiles extracted along the indicated lines in the vessel regions	98
Figure III-15	(a) RGB fundus image showing different axial flow directions in blue and red, and the static structure in green. (b) Merged 3D volumes of positively and negatively shifted data sets in red and blue respectively	98
Figure III-16	ONH blood vessel structure in an anaglyph stereo representation	99
Figure III-17	RGB light source scheme	102
Figure III-18	Data connection scheme for RGB source control	102
Figure III-19	Blood flow measurement protocol for flicker stimulation	103
Figure III-20	(a) z-projection of 3D FDOCT data ("fundus image"). The solid black line indicates the selected region of interest. (b) Tomogram at the indicated region in (a). (c) Doppler velocity image of indicated region in (a)	103
Figure III-21	Pulsatility of blood vessels. Isolating vessels in the Doppler tomogram gives access to vessel diameter and flow profile. (lhs) artery, (rhs) vein. Measurement before flicker stimulation	104
Figure III-22	Resulting effect of flicker stimulation on flow velocity and vessel diameter. Preliminary results	105

## C List of tables

Table II-1	Mutual (negative) impact of three important OCT parameters	18
Table II-2	Design criteria: comparison prism-grating for evaluating optimal choice for angular error correction	37
Table II-3	Optimized apex angle $\alpha$ for two current glasses and two different spectral ranges potentially interesting	38
Table II-4	Calculated parameters for standard prisms in BK7. $f_c=3mm$	43
Table II-5	Calculated parameters for achromatic prism pairs. $f_c=3mm$	44
Table II-6	AOFS from AA Opto-Electronics available in our laboratory for prototype packaging	45
Table II-7	Calculated parameters for standard prisms with symmetric orientation for minimum deviation (minimum reflection losses for uncoated surfaces). $f_1=f_2\approx 1.5mm$	46
Table II-8	Phase fluctuations for three different configurations with similar local $SNR\approx 26.5dB$	59



## D Scientific contributions

### D.1 Peer-reviewed publications

Bachmann A.H., Michaely R., Lasser T., Leitgeb R.A.: "*Dual beam heterodyne Fourier domain optical coherence tomography*". Opt. Express 15 (2007), in press. (multimedia file)

Michaely R., Bachmann A.H., Villiger M.L., Blatter C., Lasser T., Leitgeb R.A.: "*Vectorial retinal blood flow in 3D using high resolution resonant Doppler FDOCT*". J. Biomed. Opt. 12, 4 (2007).

Bachmann A.H., Villiger M.L., Blatter C., Lasser T., Leitgeb R.A.: "*Resonant Doppler flow imaging and optical vivisection of retinal blood vessels*". Opt. Express 15, p.408-422 (2007). <http://www.opticsinfobase.org/abstract.cfm?URI=oe-15-2-408> (multimedia files)

Leitgeb R.A., Villiger M., Bachmann A.H., Steinmann L., Lasser T.: "*Extended focus depth for Fourier domain optical coherence microscopy*". Opt. Lett. 31, p.2450-2452 (2006). <http://www.opticsinfobase.org/abstract.cfm?URI=ol-31-16-2450>

Bachmann A.H., Leitgeb R.A., Lasser T.: "*Heterodyne Fourier domain optical coherence tomography for full range probing with high axial resolution*". Opt. Express 14, p.1487-1496 (2006). <http://www.opticsinfobase.org/abstract.cfm?URI=oe-14-4-1487>

Perentes A., Bachmann A., Leutenegger M., Utke I., Sandu C., Hoffmann P.: "*Focused electron beam induced deposition of a periodic transparent nano-optic pattern*". Microelectronic Engineering 73-74, p.412-416 (2004).

Bret T., Utke I., Bachmann A., Hoffmann P.: "*In situ control of the focused-electron-beam-induced deposition process*". Appl. Phys. Lett. 83, p.4005-4007 (2003).

### D.2 Book contribution

Faupel M., Smigielski P., Grzymala R.: "Imagerie et Photonique pour les Sciences du Vivant et la Médecine". ISBN 2-88476-005-9, Fontis Media, p.275-286: L. Froehly, A. Bachmann, T. Lasser, F. Lang: "*Topographie par interférométrie spectrale multiplexée en longueur d'onde*"

### D.3 International conferences

Michaely R., Bachmann A.H., Villiger M.L., Blatter C., Lasser T., Leitgeb R.A.: *"Intensity based quantification of fast retinal blood flow in 3D via high resolution resonant Doppler spectral OCT"*. SPIE Invited Paper 6627-17 (2007).

Leitgeb R.A., Michaely R., Bachmann A.H., Villiger M., Blatter C., Lasser T.: *"Vectorial retinal blood flow and optical vessel vivisection for 3D angiography with high resolution resonant Doppler OCT"*. ARVO Paper 2758-B941, to be published in Invest. Ophthalmol. Vis. Sci. (2007).

Bachmann A.H., Leitgeb R.A., Lasser T.: *"Dual-beam heterodyne FDOCT with high axial resolution"*. SPIE Paper 6429-48 (2007).

Leitgeb R.A., Bachmann A.H., Villiger M.L., Blatter C., Lasser T.: *"Resonant Doppler Fourier domain optical coherence tomography for enhanced retinal blood flow imaging in vivo"*. SPIE Paper 6429-10 (2007).

Leitgeb R.A., Bachmann A.H., Villiger M.L., Blatter C., Lasser T., Pircher M.: *"Measurement of retinal physiology using functional Fourier domain OCT concepts"*. SPIE Paper 6426A-08 (2007).

Leitgeb R.A., Villiger M.L., Bachmann A.H., Pralong W., Meda P., Lasser T.: *"3D cell imaging with extended depth of field Fourier domain optical coherence microscopy"*. SPIE Paper 6443-04 (2007).

Sekhar C., Leitgeb R.A., Villiger M.L., Bachmann A.H., Blu T., Unser M.: *"Non-iterative exact signal recovery in frequency domain optical coherence tomography"*. ISBI Paper SA-AM-PS3.3 (2007).

Bachmann A.H., Leitgeb R.A., Lasser T.: *"Complex ultrahigh resolution Fourier domain optical coherence tomography"*. SPIE Paper 6079-26 (2006).

Leitgeb R.A., Steinmann L., Imboden C., Villiger M., Leutenegger M., Bachmann A.H., Lasser T.: *"High-resolution Fourier domain optical coherence microscopy"*. SPIE Paper 6079-33 (2006).

Leitgeb R.A., Steinmann L., Imboden C., Villiger M., Leutenegger M., Bachmann A.H., Lasser T.: *"Highly confined depth focus for Fourier domain optical coherence microscopy"*. SPIE Paper 6090-07 (2006).

Froehly L., Bachmann A., Lasser T., Depeursinge C., Lang F.: *"Wavelength multiplexed spectral interferometry for endoscopic topographic imaging"*. Proc. SPIE Vol. 5864, p.47-57 (2005).

Liebling M., Bernhard T.F., Bachmann A.H., Froehly L., Lasser T., Unser M.: *"Continuous Wavelet Transform Ridge Extraction for Spectral Interferometry Imaging"*. SPIE Paper 5690-65 (2005).

Bachmann A., Froehly L., Lasser T., Depeursinge C., Lang F.: *"Nouvelle méthode d'imagerie 3D: interférométrie spectrale multiplexée en longueur d'onde"*. CMOI, Belfort (F), 17-21 nov. 2003.

Froehly L., Bachmann A., Lasser T., Depeursinge C., Lang F.: *"Nouvelle méthode d'imagerie 3D: interférométrie spectrale multiplexée en longueur d'onde"*. IMVIE, Strasbourg (F), 15-17 sept. 2003.



## E Acknowledgements

I am grateful for the help and contributions from my colleagues, as well as for the support from my family and friends. I would like to thank my parents for supporting me throughout the years of education what finally led to completing this thesis.

I have been very fortunate to work with people who turned out to be not only colleagues, but friends. The not so rare long working days would have been much more exhausting without the joy of this friendship.

I would like to thank my thesis director Prof. Theo Lasser for giving me the opportunity to work in his well equipped laboratory with palatine standard lab surface and the office space with breath-taking view towards the Swiss and French Alps and the Lake of Geneva I sometimes paddled on. I appreciated his friendly and collegial interaction and I'm grateful for his assurance and confidence as well as his valuable help throughout my thesis.

There is not enough space to acknowledge my thesis co-director Prof. Rainer Leitgeb for all his help. His great personality, almost inexhaustible support and immense knowledge in the field of OCT were an indispensable help to me. I am deeply in debt for his availability when projects were difficult, his good intuition regarding which direction a project should be directed to and his valuable programming skills in LabVIEW for almost perfectly synchronizing a frame grabber and a camera which did not want to obey as they were supposed to.

First as a student and then as an office mate Martin Villiger was a great colleague. His good knowledge in optics as well as his ambition to solve problems not so simple to resolve helped me a lot for the resonant Doppler FDOCT project. I would like to thank Roland Michaely for his friendship and the best home-made pizza I know. He was a great help in preparing the tomogram-data of the ophthalmologic measurements for better and animated presentations. Antonio Lopez did a lot of technical drawings on my behalf and was fighting, together with Joseph Lasser, against group-internal laziness regarding inventory issues. Pablo Dosil Rosende was a very valuable sports mate and friend. Wouldn't it be for him, I'd probably forgot how to paddle in my flat-water kayak! I would like to thank the other group members Marcel Leutenegger, Matthias Geissbühler, Iwan Märki, Vladislav Shcheslavskiy and Erica Martin-Williams for scientific discussions and sharing *croissants* and *pains au chocolat* at the weekly group meeting.

Working in a lab at EPFL, not many female collaborators are in your entourage. Our secretary Judith Chaubert, however, was not only special due to this fact. She managed to deal with the ever changing bureaucratic rules and directives at EPFL without discommoding the lab members more than necessary and still express friendliness and be available for our issues.

But what would be our laboratory without its history? I would like to thank lab alumni I met and worked with: Sébastien Favre for his supervision of my diploma project, Luc Froehly for teaching me a lot of useful skills in the optics lab, Michael Gösch, Kai Hassler, Per Rigler,

Tiemo Anhut, Ramachandra Rao, Alexandre Serov, Boris Karamata, Markus Laubscher and Marcel Zeller for the good time we spent. I would like to thank the former group member Jelena Mitic for starting the weekly running group together with me and lending her name for the famous *tour Jelena* we still quite often jog.

Many thanks go to Yannick Fournier, Thomas Maeder, Damien Sonney, Sanna Palmgren, Caroline Jacq and Prof. Peter Ryser for regularly or at least occasionally running with me and some of them for coping with the single available shower afterwards.

Within the whole institute our laboratory is affiliated to I would like to thank in particular Roland Gianotti for his electronics know-how and help with circuitry, Thomas Sidler for lab equipment and answers to questions nobody else could answer, Alejandro Salamanca for IT support, François Aguet for his help on some image processing and Chandra Seelamantula for discussions on reconstruction algorithms.

Many thanks also go to other groups within the institute and at EPFL for lending us lab equipment when we were missing a particular device or after a breakdown of a component when it was most needed.

I was happy to work with some excellent students I would like to mention at this place. Cédric Blatter helped me designing the ophthalmic system from scratch. Christophe Pache was a driving force in extending the ophthalmic system towards optical testing of retinal physiology. Tilman Schmoll helped me a lot with developing the rigid esophagoscope and Roland Vulliamy did all the simulations about bandwidth increase for the fiberized acousto-optic frequency shifters. Although their projects are not part of this thesis, I appreciated working with Lukas Steinmann, Chantal Imboden, Enrico Seise, Christian Rödel, and once again Martin Villiger and Cédric Blatter (the only – former – students completing two projects with me).

The machine shop of the micro-engineering department did a lot of work for my several projects and I would like to thank all its members for their flexibility, precise manufacturing and technical advice.

I highly appreciated industrial cooperation with EXALOS AG (Schlieren, Switzerland) for providing semiconductor broadband light sources and Cube Optics AG (Mainz, Germany) for prototype manufacturing of the fiberized acousto-optic frequency shifters.

Finally, I would like to thank all my friends from sports and abroad who maintained contact with me throughout the years I stayed in Lausanne.

Last but not least I would like to thank my girlfriend Jsabelle for her love and understanding, especially throughout the last months when working on my thesis was often more important than anything else.

... and all I might have forgotten to mention.

## F Curriculum Vitæ

Adrian H. Bachmann  
Rislenstrasse 10  
CH-8590 Romanshorn

---

Born on July 12, 1976 in Uzwil, Switzerland; Swiss nationality.

### Professional activities

- |             |   |
|-------------|---|
| 2004 - 2007 | PhD student in the Laboratoire d'Optique Biomédicale, Ecole Polytechnique Fédérale de Lausanne (EPFL):<br><ul style="list-style-type: none"> <li>- <i>working on different concepts in FDOCT with phase manipulation techniques as main research topic</i></li> <li>- <i>three patent applications</i></li> </ul> |
| 2003 - 2004 | Assistant in the Laboratoire d'Optique Biomédicale, EPFL:<br><ul style="list-style-type: none"> <li>- <i>working on spectrally encoded interferometry</i></li> </ul>  |
| 2001        | Internship in the electronics laboratory of the Fritz-Haber-Institut, Max-Planck-Gesellschaft, Berlin (3 months)  |
| 1999 - 2000 | Internship at Weidmann Plastics Technology AG, Rapperswil (11 months)   |

### Education

- |             |  |
|-------------|--|
| 1997 - 2003 | Microengineering at EPFL, specialization in applied photonics; <i>Ingénieur</i> diploma, equivalent to MS degree |
| 1991 - 1996 | Maturité fédérale typus C, Kantonsschule Romanshorn  |

Adrian Bachmann was actively involved in teaching Bachelor and Master course level at EPFL and supervised eleven student laboratory projects. Prior to his PhD studies he was a high performance athlete and participated at the Olympic Games in Sydney 2000. After his active sporting career he became technical director at the Swiss Canoe Federation and led its competition department on voluntary basis. He was Olympic torch bearer and head of the Swiss canoe delegation for the Olympic Games in Athens 2004. Adrian Bachmann was rewarded three prizes related to his work at EPFL and two related to his achievements in sports. He is still active in sports administration on voluntary basis.